Deposition and structural properties of silicon carbide thin films for solar cell applications.

Joshua Relebogile Khoele

A thesis submitted in fulfillment of the requirements for the degree of Magister Scientiae in the Department of Physics, University of the Western Cape

Supervisor: Dr. S. Halindintwali, University of the Western Cape

Co-supervisor: Prof B. Julies, University of the Western Cape

November 2014

Declaration

I declare that *Deposition and structural properties of silicon carbide thin films for solar cell applications* is my own work, that it has not been submitted for any degree or examination in any other university, and that all sources I have used or quoted have been indicated and acknowledged by complete references.

Joshua Relebogile Khoele **November 2014**

Signature:

ABSTRACT

The growth of hydrogenated amorphous silicon carbide (a-SiC:H) thin films deposited by Hot-Wire Chemical Vapour Deposition (HWCVD) for solar cell applications has been studied. The films were characterized for structural properties using Fourier Transform Infrared Spectroscopy FTIR, Elastic Recoil Detection Analysis (ERDA), X-ray Diffraction (XRD), Transmission Electron Microscopy (TEM) and Raman Spectroscopy (RS). A low temperature of the substrate heater maintained at 280 °C was used in this thesis due to the demand of low-cost solar cells based on cheap substrate that require deposition at such low temperatures. In this thesis, we showed that the structural properties of a-SiC:H films are dependent on the filament temperature and also on the CH_4 gas flow rate. It was shown that in non-stoichiometric a-SiC:H, hydrogen content throughout the deposited films varies with depth. An attempt is done in this study to determine, for the first time the absorption strength of the C-H_n bonds in the 950 -1050 cm^{-1} band of the FTIR spectrum. Real-time ERDA was used to determine the hydrogen kinetics parameters in a single temperature ramp; a model based on the solution of the diffusion equation is used for this effect.

November, 2014

UNIVERSITY of the
WESTERN CAPE

DEDICATION

To my parents the late Jeremiah and Maria Khoele, thank you for carrying me.

ACKNOWLEDGEMENTS

I would firstly want to thank my Lord and Saviour Jesus Christ for the opportunity to do this work presented and for the following persons and their support:

Dr. Sylvain Halindintwali of the department of Physics at the University of the Western Cape (UWC) for giving me the opportunity to be his student, his guidance and support throughout this investigation;

Prof Basil Julies of the Electron Microscope Unit at UWC, my co-supervisor, for his help with TEM measurements of the samples, encouragement, guidance, direction and continual support throughout this investigation;

Mr. Timothy Lesch, of the Department of Chemistry at UWC, for his assistance with the FTIR and Raman measurements;

Dr. Remy Butcher, of the Material Research Group at iThemba LABS, for his assistance with the XRD measurements;

Dr. Mlungisi Nkosi, of the Materials Research Department iThemba LABS, for his assistance with the AFM measurements;

Prof. Craig M. Comrie, from the iThemba LABS Material Research Group, for his assistance with the ERD measurements;

My fellow Matsci/Manus students for their much treasured friendship and many discussions around this investigation;

A special thanks to my friend Nozipho Dzimba, for her continual encouragement and support during the time of this project;

UNIVERSITY of the
WESTERN CAPE

A special thanks to Pastors Seth and Annah Tladi and the entire Jehovah Reigns family at Epping, for their continual support and encouragement throughout this work.

Table of Contents

ABSTRACT....3

ACKNOWLEDGEMENTS....5

Chapter 1. Introduction....10

1.1 Overview on Photovoltaic Technology....10

1.2 The Three Generation Photovoltaic Technologies....11

1.3 Background on Silicon Carbide Films....15

1.3.1 Crystalline Silicon Carbide....16

1.3.2 Amorphous Silicon Carbide....19

1.4 Hydrogenated Silicon Carbide....21

1.5 Doping of Silicon Carbide films....22

1.6 Material properties....24

1.7 SiC as window layer in Solar cells....26

1.8 Aim and Outlines....28

References....30

Chapter 2. Hot wire chemical vapour deposition systems....34

2.1 Introduction....34

2.2 Background on HWCVD....35

2.3 Thin film deposition....37

References....38

Chapter 3. Characterization Methods....39

3.1 Infrared Spectroscopy....39

3.1.1 Introduction....39

3.1.2 Theory....39

3.1.3 Background Theory on Vibrational modes....42

3.1.4 Bonding in Silicon Carbide films....44

3.1.5 Determination of Hydrogen and Silicon Carbide concentration in the Deposited Films....46

3.2 Elastic Recoil Detection Analysis....49

3.2.1 Introduction....49

3.2.2 Background theory of ERDA....49

3.2.3 The experimental set up....52

3.2.4 Real Time-ERD....55

3.3 Raman Spectroscopy....58

UNIVERSITY of the
WESTERN CAPE

3.3.1 Introduction 58
3.3.2 Theoretical background 58
3.3.3 Thin films applications 63
3.3.4 Structural Characterization in Raman Spectroscopy 64
3.4 Transmission Electron Microscopy 65
3.4.1 Introduction 65
3.4.2 Theory 65
3.4.3 Operation of a TEM 69
3.4.5 Alternative techniques in the TEM 74
3.4.6 Specimen Preparation 75
3.5 Atomic Force Microscopy 80
3.5.1 Introduction 80
3.5.2 Theoretical Background 81
3.5.3 Surface Morphology and Roughness Measurements 83
3.6 XRD characterization 84
3.6.1 Introduction 84
3.6.2 Absorption of X-rays 85
3.6.3 Diffraction of X- rays 86
References 87
Chapter 4. Structural Properties of the Deposited Materials 92
4.1 Deposition conditions 92
4.2 The effect of the filament temperature 95
4.2.1 The effect of the filament temperature on deposition rate 95
4.2.2 AFM topography of films deposited at varied filament temperatures 97
4.2.3 Effect of filament temperature on microstructure by FTIR analysis 99
4.2.4 Effect of the filament temperature on the microstructure as studied by Raman scattering spectroscopy 101
4.2.5 Effect of the filament temperature on the microstructure as studied by XRD analytical technique 104
4.2.6 Effect of the temperature of the filament on hydrogen incorporation in the films as studied by ERDA 105
4.2.7 Influence of the temperature of the filament on the microstructure as investigated by TEM 107
4.3 Effect of CH_4 flow rate on the film microstructure 111

UNIVERSITY of the
WESTERN CAPE

4.3.1 Effect of CH_4 flow rate on deposition rate 111
4.3.2 Effect of CH_4 flow rate on the films' microstructure by TEM 112
4.3.3 Effect of CH_4 flow rate on microstructure as studied by FTIR spectroscopy 115
4.3.4 Effect of CH_4 flow rate on hydrogen incorporation, investigated by ERDA 118
4.3.5 Determination of the absorption strength of the 960 - 1050 cm^{-1} band due to CH_n bonds 121
4.5 Evolution of hydrogen in the samples with annealing. 123
4.5.1 Introduction on the annealing of a-SiC:H films 123
4.5.2 Annealing conditions 124
4.5.3 Annealing induced effects investigated by FTIR analytical technique. 125
4.5.4 Effect of annealing on the microstructure as studied by Raman spectroscopy 130
4.5.5 Effect of annealing on the microstructure as studied by XRD 134
4.5.6 Conclusions 138
References 140
Chapter 5. Hydrogen Kinetics Studies 146
5.1 Hydrogen kinetics in a-Si:H and a-SiC: H thin films investigated by Real-time ERD 146
5.2 Sample description and methods 146
5.3 Results and discussion 148
References 153
Chapter 6. Conclusions and Recommendations 154
6.1 Conclusions 154
6.2 Recommendations and Future Research 156

UNIVERSITY of the
WESTERN CAPE

Chapter 1. Introduction

1.1 Overview on Photovoltaic Technology

The Photovoltaic effect was firstly known through the work of the scientist Alexandre Edmond Becquerel who, in 1839, discovered that an electrode submerged in an electrolyte solution could produce electricity when light shines on the electrode [1.1]. However, it was only until 1888 that Charles Fritts [1.2] demonstrated the first working selenium based solar cell which yielded an efficiency of less than 1%: it is only then that a renewed interest in the photovoltaic research appeared again in the scientific community. The working principle of a photovoltaic cell lies on the ability of semiconductor materials to produce electricity through the conversion of sunlight.

UNIVERSITY of the WESTERN CAPE

However the conversion of sunlight into electricity by a photovoltaic cell has not reached its maximum point due to the various limitations in the materials' structure fabricated for solar cell application. Silicon solar cell technology have dominated the photovoltaic cell industry over the past three decades, however due to high manufacturing costs of these solar cells, a route in applying thin film solar cell technology has been deemed viable in replacing the highly efficient bulk materials. The development of silicon technology for solar cell application based on silicon has ever since grown from the use of single crystalline silicon (c-Si) to various forms such as polycrystalline silicon (pc-Si) and the thin film hydrogenated amorphous silicon and micro/nano-crystalline silicon for sustainable renewable energy sources. The use of photovoltaic module systems is tipped to be among alternatives to fossil fuels such as coal and petroleum that release greenhouse gases [1.3].

1.2 The Three Generation Photovoltaic Technologies

Significant advances in silicon technology have been registered in photovoltaic applications since the conception of the crystalline silicon wafers known as the first generation photovoltaic technology, although very efficient, their main drawback is the high processing and manufacturing costs. Second generation photovoltaic technology also known as thin film technology were developed in order to reduce manufacturing costs by cutting down on material consumption and the energy used to fabricate the materials, thus making low cost manufactured photovoltaic cells. However the promise of an improvement in the energy conversion efficiency of these second generation photovoltaic cells, which is below that of crystalline silicon, has not yet been realized. Optimization of these second generation cells may lead to higher conversion efficiencies as suggested by Shockley and Queisser who indicated the possibility of these materials to surpass the detailed balance [1.4]. In the Shockley and Queisser's model, the contributing factors to the efficiency limit is due to transmission loses that occur from photons carrying energies lower than the band gap and also from the thermal relaxation losses due to photons of energy higher than the band gap.

UNIVERSITY of the
WESTERN CAPE

Third generation photovoltaic technology also utilizes thin film materials with the aim of producing photovoltaic cells with higher conversion efficiencies than first and second generation technologies by taking advantage of the transmission losses experienced in second generation solar cells. An example of third generation photovoltaic cells are multi-junctions which are made of superimposed subcells with absorbers of energy band gaps that are able to absorb an extended range of the spectrum, leading to an efficient conversion of electricity and thus breaking the

Shockley-Queisser theoretical limit of single band gap devices. Multi-junction cells have now reached the conversion efficiency milestone of ~40% [1.5].

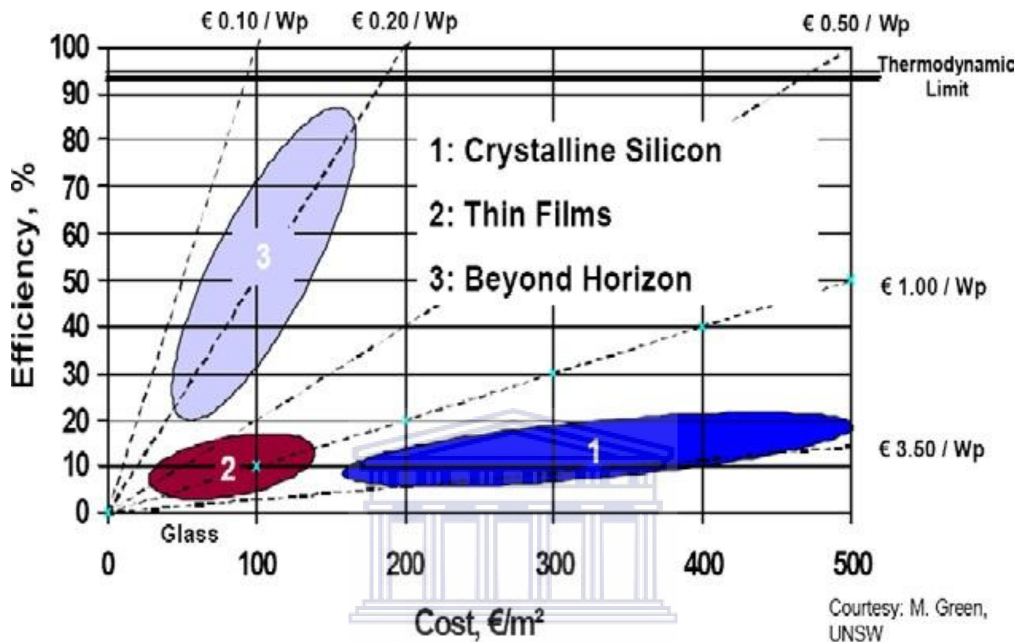

UNIVERSITY of the
WESTERN CAPE

Figure 1.1. *Cost-efficiency analysis for (1) first-generation, (2), second-generation and (3) third generation photovoltaic technologies [1.6].*

Figure 1.1 is a summary of the cost-efficiency of the evolution in photovoltaic technologies comparing achievable cost in crystalline silicon technology to the projected costs of second generation and third generation photovoltaic technologies. From fig. 1.1 it can be deduced that although the third generation PV technologies projects higher efficiencies, second generation PV cells have the advantage of reducing costs pertaining to module production measured by the total manufacturing costs per square area and the conversion efficiency [1.6]. One approach towards aiming to increase the conversion efficiency in second generation PV cells is by improving the

transmission of photons to an intrinsic layer in a p-i-n junction solar cell. Wide band gap materials as a window layer allow transmission of most of the useful light in solar cells and thus increasing the probability of photon absorption in the intrinsic layers of p-i-n or n-i-p structured solar cells.

The break-even price of solar cell modules depend on the total cost of the manufacturing process and the conversion efficiency of the module; second and third photovoltaic technologies are advantageous to use when considering the energy pay-back time (EPBT) of the solar cells. EPBT is the time needed for the photovoltaic solar module to pay back the quantity of energy invested during its fabrication; therefore a small value of the EPBT is desirable. It is reported that the EPBT for Photovoltaic systems in the Northern Europe is equal to about one year [1.7].

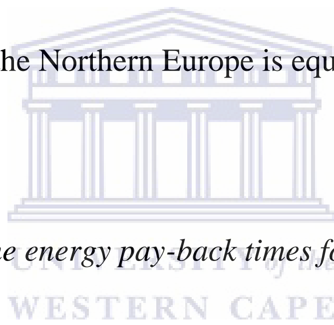
UNIVERSITY of the
WESTERN CAPE

Table1.1 *EPBT chart describing the energy pay-back times for multi-crystalline and thin film photovoltaic systems. [1.8].*

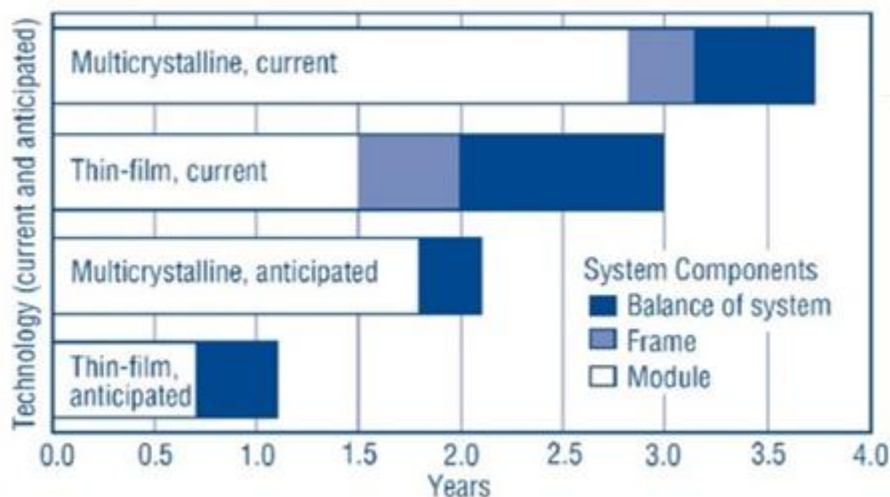

The EPBT is calculated using the following relation:

$$EPBT = \frac{E_{mat} + E_{manuf} + E_{inst}}{E_{agen}} \tag{1.1}$$

where E_{mat} is the energy needed to produce the materials of the photovoltaic system, E_{manuf} is the energy needed to manufacture the system, E_{inst} is the energy to install the system and E_{agen} is the annual electrical energy supplied by the system. From Eqn. 1.1 it can be deduced that thin film solar cells would be advantageous to use since less energy is required to manufacture and install the photovoltaic systems compared to multi-crystalline PV and also the output energy from these cells are comparable. In contrast the EPBT is the highest due to high cost in the manufacturing process associated with the materials [1.9]. Generally the measure of PV module cost is dependent on the total manufacturing cost of the module per square area and the conversion efficiency; Fig. 1.1 compares an estimate of achievable cost with c-Si technology with projected achievable costs of other PV technologies. This implies that the c-Si wafer technology would not be able to meet the low-cost targets, whereas thin-film technologies have the potential to provide a viable alternative in the near future [1.9].

UNIVERSITY of the
WESTERN CAPE

Thin films technology involves the processing of intrinsic layers of thickness less than a micron; the opto-electronic properties and overall performance depend on the composition and microstructure of the film. Thin films have several applications such as thin film thermo-mechanical sensors [1.10], and thin film solar cells [1.11]. Advantages in fabrication of thin films solar cells include reduction of the modules' thickness to about 50 μm or less, the use of cheap substrates such as glass or plastic and large-area modules fabrication leading to reduced manufacturing production costs [1.9]. On the other hand a major disadvantage is that the material properties of the fabricated thin films products dependent on the deposition conditions employed

and thus the reproducibility is not guaranteed [1.12, 1.13, 1.14]. The deposition of thin films has been studied intensively and there is an agreement among the PV research community that the deposited films are highly dependent on the deposition techniques and deposition conditions employed. Progress in material characterization techniques during the last decades have resulted in a deeper understanding of the correlation between the deposition conditions and the modules' performance.

1.3 Background on Silicon Carbide Films

UNIVERSITY of the
WESTERN CAPE

Silicon Carbide is the only stable compound made up of a silicon and carbon atom with a stoichiometry of 1:1 [1.15]. Silicon carbide's only natural occurrence was discovered in meteorites, which implies that it can only be fabricated with deposition techniques developed for processing these materials [1.16]. Application of Silicon carbide in research areas such as Microelectromechanical systems (MEMS) has been promising and viable material replacing its dominant counterpart silicon as SiC exhibits superior properties such as wide band gap, higher melting temperature, elastic modulus, fracture toughness, hardness, chemical inertness and thermal conductivity; all these characteristics are essential in harsh environment applications [1.17, 1.18]. Silicon carbide is applied in Microelectromechanical systems (MEMS) as protective coatings for harsh environments [1.18]. For MEMS application, silicon carbide-based materials possess superior optical and electrical properties such as high thermal conductivity and electrical stability at temperatures higher than 300°C compared to silicon-based materials, which are limited to an operational temperature of 250°C [1.19].

Silicon carbide has also found application in photovoltaic cells as an n- or p-type doped layer in amorphous or microcrystalline silicon solar cells because of its advantageous properties such as a wide band gap, high carrier mobility and high conductivities for both n- and p-type doping [1.20]. T. Chen *et al.* [1.20] demonstrated that crystalline silicon carbide may be used as a transparent conductive window layers in thin film solar cells, eliminating the use of transparent conductive oxides in the solar cell structures and consequently improving amount of sunlight transmitted to the intrinsic layer.

1.3.1 Crystalline Silicon Carbide

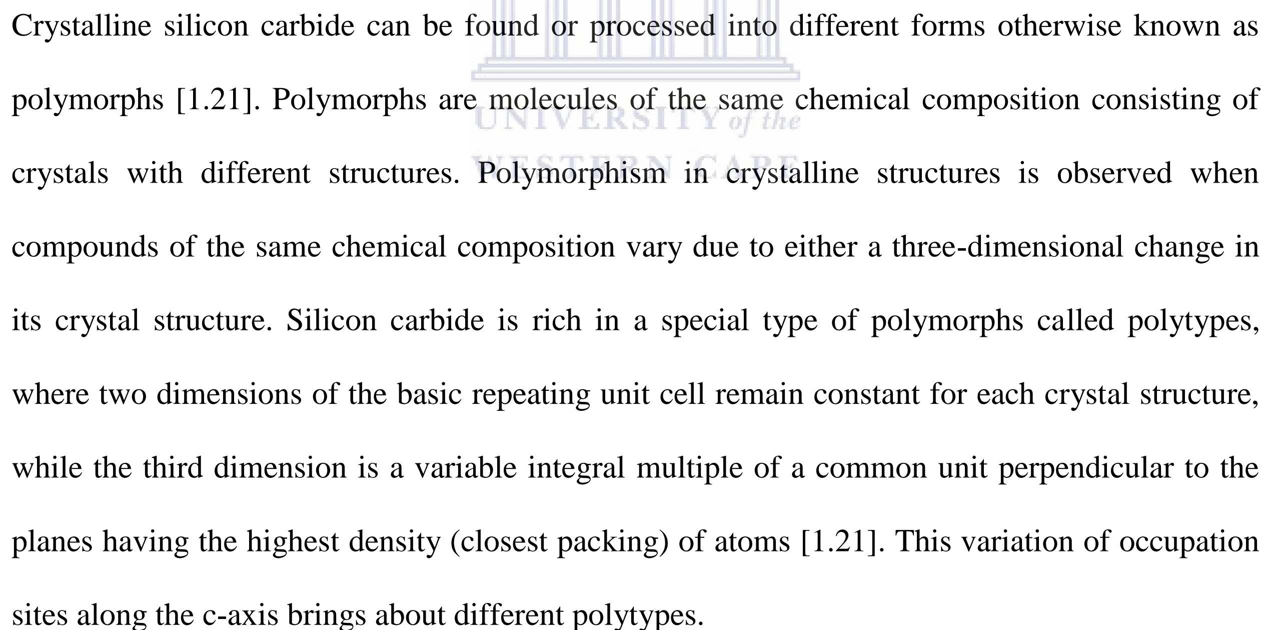

Crystalline silicon carbide can be found or processed into different forms otherwise known as polymorphs [1.21]. Polymorphs are molecules of the same chemical composition consisting of crystals with different structures. Polymorphism in crystalline structures is observed when compounds of the same chemical composition vary due to either a three-dimensional change in its crystal structure. Silicon carbide is rich in a special type of polymorphs called polytypes, where two dimensions of the basic repeating unit cell remain constant for each crystal structure, while the third dimension is a variable integral multiple of a common unit perpendicular to the planes having the highest density (closest packing) of atoms [1.21]. This variation of occupation sites along the c-axis brings about different polytypes.

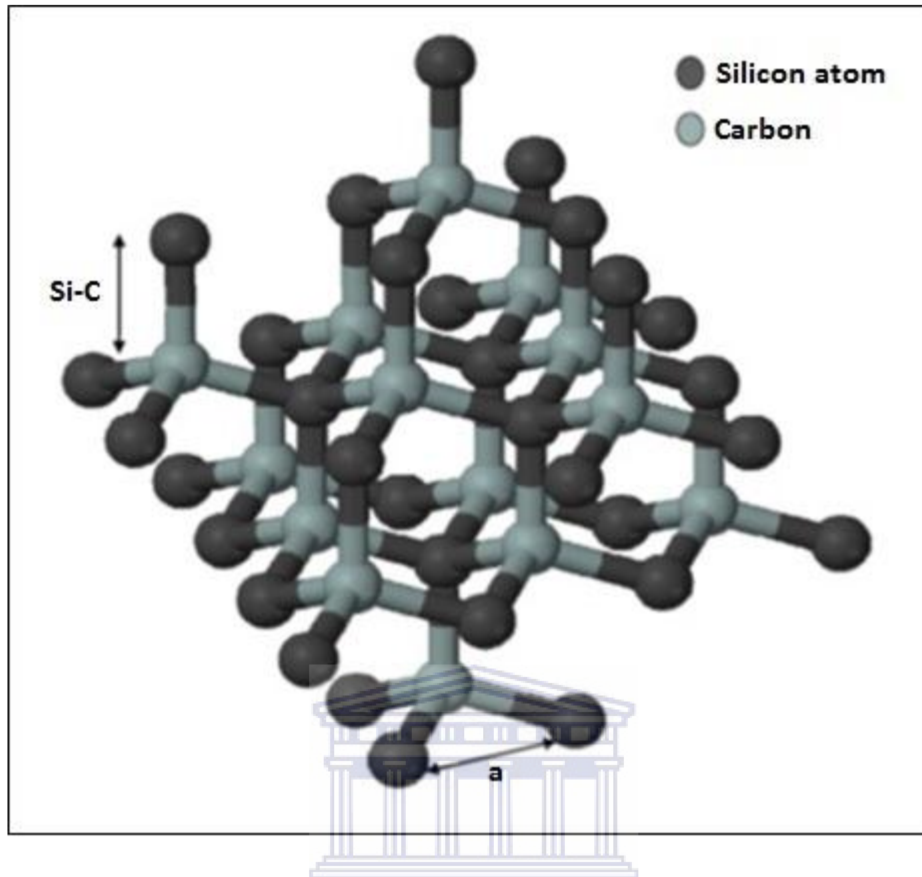

Figure 1.2. *The tetragonal structure of a Carbon atom bonded to four nearest Silicon neighbors [1.19].*

UNIVERSITY of the
WESTERN CAPE

Figure 1.2 shows the Si-C structure consisting of a carbon atom at the center of a tetrahedral structure and surrounded by four Si atoms. The distance between the silicon and carbon bond (C-Si bond) is approximately 1.89 Å and the nearest carbon and silicon atom distance marked as 'a', known as the lattice constant, on the diagram is approximately 3.09 Å. The figure displays a crystalline structure of Si-C; the crystalline structure differs from polytype to polytype.

Although silicon carbide consists of over 250 known polytypes, the most common are 3C and 6H; 4H, 15R and 2H, all other polytypes are a combinations of these polytypes [1.40]. The numbers before each letter represents the number of layers along the c-axis before the repeat of

the stacked layers of the same sequence, while the letters represent which type of Bravais lattice the structure belongs to, as described in Table 1.2. Examples of the stacking of these polytypes are shown in Figure 1.3 [1.22].

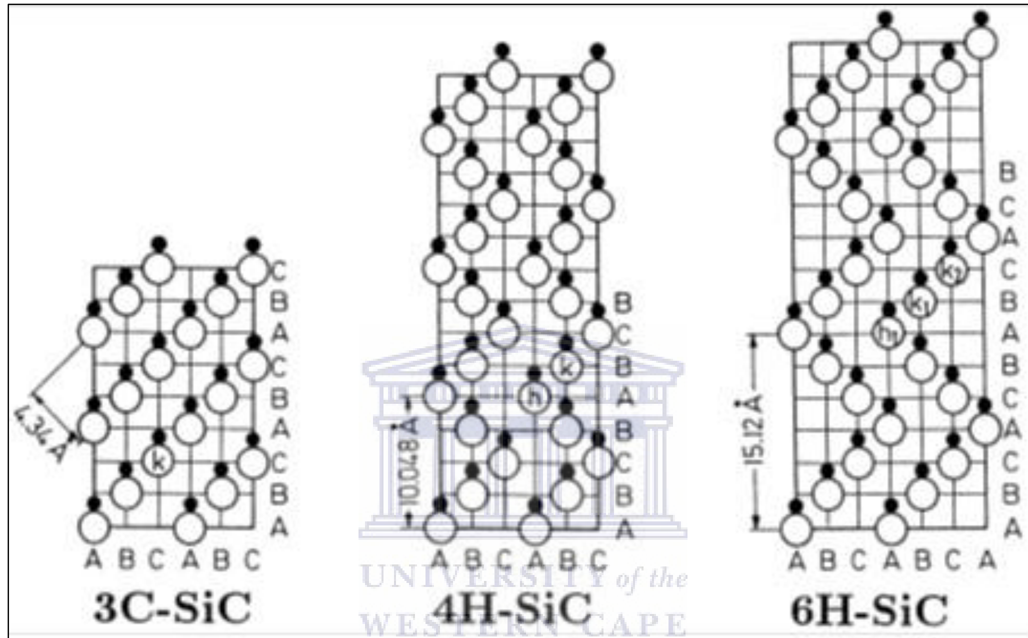

UNIVERSITY of the
WESTERN CAPE

Figure 1.3. *Examples of the most commonly known SiC polytypes.*

These polytypes consist of Si and C elements structurally arranged differently; the stacking of these elements is found to have an influence on the electrical properties of the material thus each polytype displays its fundamental electrical and optical properties [1.23]. The three most common polytypes of SiC, 3C-SiC, 4H-SiC and 6H-SiC possess an indirect band gap characteristic and exhibit band gaps of about 2.39, 3.27 and 3.02 eV respectively [1.24].

Table 1.2. *Bravais lattices with the corresponding polytype letters.*

Letters	Bravais lattice
C	Cubic
H	Hexagonal
R	Rhombohedral

The wide band gap allows for the material to be used in high temperature operation without any interference from the intrinsic conductivity effects. During high temperature operation, bound electrons in the material can be thermally excited into the conduction band causing a transient electrical conductivity [1.23].

The application of high band gap materials are also advantageous in photovoltaic cells as window layers because of their high transparency in the visible spectrum range, that is in the range; because they allow photons spread over a large range of frequency to pass through to the intrinsic layer in p-i-n and n-i-p structures [1.25]. Crystalline cubic silicon carbide (3C-SiC) however is superior in photovoltaic applications because it possesses relatively high electron mobility compared to other polytypes [1.26].

1.3.2 Amorphous Silicon Carbide

Amorphous alloys possess a structure with no long range order, with only a short-range atomic ordering in the films, thus the material does not form a crystal. Amorphous silicon carbide (a-SiC:H) possesses a tetrahedral structure; however the slight variations in the bond lengths

UNIVERSITY of the WESTERN CAPE

introduce a short-range atomic ordering within the material's network. Because of the departure from the known values of the Si-Si bond angles and Si-Si bond lengths of the crystalline configuration, amorphous networks such as a-Si contain unsaturated dangling bonds that act as recombination centers.

Table 1.3 describes the different bonds and bond lengths in SiC films [1.16]. This variation in bond lengths of a-SiC brings about the disorder of the network, and thus a high number of dangling bonds are also observed in such films. The introduction of the recombination sites causes a deterioration of its photo-electronic properties due to an increase in the density of electronic states [1.27].

Stefan Janz suggested that for amorphous tetrahedral alloys, in this case amorphous silicon carbide, there will be more disorder compared to amorphous silicon since chemical disorder is added to the inherent structural disorder [1.16]. The addition of carbon in the a-Si:H network however leads to other superior material properties such as a wide optical band gap, depending on the carbon content in the films.

UNIVERSITY of the
WESTERN CAPE

Pereyra *et al.* [1.28] showed from Plasma Enhanced Chemical Vapour Deposition technique deposited films under silane starving conditions that the band gap increased from about 1.5 to 3.5 eV when the C content was increased from 0 to 70%.

Pereyra *et al.* [1.28] also argued that films with high concentration of polymer chains exhibit high band gap values; the increase in the band gap is attributed to the higher concentration of polymer chains in the film [1.29]. It has been suggested that high band gaps are associated with diamond – like sp3 C-C bonding; the sp2 C-C bonding leads instead to a porous structure that

reduces the bang gap [1.30]. Thus the growth process of SiC must be optimized for material quality a-SiC with high band gap as candidate for window layer in Si based solar cells.

Table 1.3. *SiC bonds and bond lengths.*

Bond	Length [10^{-1}nm]	Bond	Length [10^{-1}nm]
C-C	1.54	C-H (sp^3)	1.09
C=C	1.33	Si-H	1.48
C=C (graphite)	1.42	Si-Si (in c-Si)	2.35
C≡C	1.21	C-Si	1.87

UNIVERSITY of the
WESTERN CAPE

1.4 Hydrogenated Silicon Carbide

Following the observation of the degradation effect by D.L. Staebler and C.R. Wronski [1.41], known as the Staebler Wronski Effect (SWE), new approaches on minimizing this effect have been considered by optimizing the deposition process. The SWE degradation was observed when an amorphous silicon layer exposed to light experienced a breaking of the bonds within the amorphous network consequently creating dangling bonds within the network; this consequently reduced significantly the dark conductivity and photo conductivity of the material. However the incorporation of hydrogen in the deposited layers proved to reduce the rate at which this

degradation effect occurred. Using a thermal and catalytic process in the deposition of hydrogenated amorphous silicon films, Matsumura *et al.* [1.42] showed that the passivation of dangling bond by the hydrogen atoms within the amorphous layer resulted in high quality films with improved electronic properties. It was later shown that only a small amount of hydrogen in the films is adequate to produce high quality stable thin films that resist the SWE. R. Platz *et al.* [1.43] showed by the use of higher substrate temperature, that a decrease in H content stabilized and improved the electronic transport properties after the degradation effect.

The already demonstrated beneficial effect of hydrogen on Si films applies also to hydrogenated amorphous silicon carbide films; hydrogenation recombination sites in the films and promote a more coordinated amorphous network [1.31]. Hydrogenated silicon carbide is desired as a layer with high conductivity property. It is found experimentally that H effuses from a-SiC:H above 600 $^{\circ}$C and a crystallization process follows [1.16]. During high temperature deposition of a-SiC:H films from SiH_4, CH_4 and H_2 gas mixture, the carbon atoms preferentially bond with silicon atoms; this results in an increased amount of Si-C bonds in the deposited films, reducing the deposition of carbon clusters in the form of sp^2 C-C bonds, responsible for poor electronic conduction characteristics [1.28, 1.32, 1.33].

UNIVERSITY of the
WESTERN CAPE

1.5 Doping of Silicon Carbide films

The concentration of doping atoms in semiconductor materials is one of the important parameters that determine the design and also performance of the photovoltaic cell [1.44]. Doping is used in order to separate the photo-generated charge carriers from the absorber layer

and allowing a flow of current in the external circuit out of the solar cell. There are two types of doping in a semiconductor; n-type doping is achieved when donor foreign elements are introduced in the solar cell and p-type when acceptor elements are added.

Silicon carbide thin films can be doped to both n- and p-type and resulting both materials display wide band gap and high conductivity characteristics [1.20]. Silicon carbide doping is usually applied in order to improve the electrical conductivity of the films, however the challenge of doping such films is the degree of structural disorder, film crystallinity and the defect distribution [1.45]. Boron has been optimized for p-type doping in a-Si:H films, but since the p-doped a-Si:H exhibits a reduced band gap, the alloying of carbon in a-Si:H has the beneficial effect of compensating the band gap width [1.49]. Boron-doped hydrogenated microcrystalline silicon-carbide (p-µc-SiC:H) films are preferred however as a p-type material in hydrogenated amorphous silicon (a-Si:H) based solar cell because they have higher electrical conductivity, optical transmittivity, carrier mobility, and dopability than conventional p-type hydrogenated amorphous silicon-carbide (p-a-SiC:H) thin films [1.46].

UNIVERSITY of the
WESTERN CAPE

The most commonly used method of doping is adding a dopant gas such as diborane (B_2H_6), phosphine (PH_3), in the deposition process, where the dopant gas is split into its desired radical in a Plasma Enhanced Chemical Vapour Deposition (PECVD) or Hot Wire Chemical Vapour Deposition (HWCVD) system. The doping of boron from diborane gas for optimum use as p-doped a-SiC:H has been achieved by Schropp *et al.* [1.47] where they used an equal amount of silane and methane whereas for diborane, a factor of a thousand lower was utilized in yielding an optimized p-type film with an energy band gap (E_g) = 2.0 eV, activation energy (E_A) = 0.5 eV, conductivity (σ_d) = 10^{-5} Ω^{-1} cm^{-1}, and absorption coefficient at 600 cm^{-1} wavelength (α_{600}) = 10^4 cm^{-1}.

The dopant gases such as diborane and phosphine are extremely toxic, with its threshold limited value (TLV) values in the low parts-per-million range. Therefore the use of such gases requires extreme care when being handled.

Doping can also be achieved by evaporation, whereby a metal such as Aluminium (Al) is heated to very high temperatures reaching its melting point and thereafter its heat of evaporation. The evaporated metal can thus be co-deposited with the precursor gases during growth.

The control over the level of doping from this method is challenging, however a suggested method is to co-deposit the precursor gases along with the evaporated metal from the start of the deposition process until the film reaches a thickness around a few tens of nanometers, and then continue the deposition in the absence of the dopant plume.

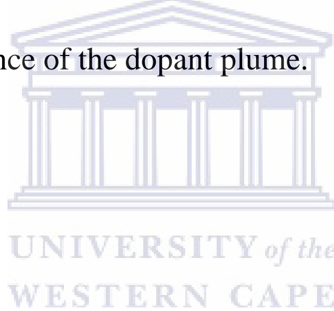

1.6 Material properties

UNIVERSITY of the
WESTERN CAPE

The common classification of silicon carbide as a wide band gap material is in reference to its band gap which is significantly higher than that of silicon. The high band gap property prevents thermal and other small energy excitations to cause valence electrons to bridge the gap. SiC films are thus better candidates for devices operating at high temperature. Silicon Carbide exhibits other properties such as high breakdown field and high electron mobility. [1.34].

Since the early 1980-ies, extensive research was conducted by many labs in the fabrication and optimization of a-Si:H based alloys which led to the discovery of amorphous silicon carbide (a-SiC:H) semiconductor, and was utilized as a low-absorbing p-type window layer in a-Si:H solar cells [1.34]. This discovery opened up to improvements of silicon based technologies in fields

such as MEMS. In solar cell applications, a-SiC:H as a p-type semiconductor layer reduces absorption losses in the p-layer [1.35]. The wide energy band gap of the p-type semiconductor layer allows most of the radiation of the solar spectrum passage, thus increasing the chance of high absorption of the photons in the intrinsic layer. Bullot *et al.* [1.36] reported that hydrogenated amorphous silicon carbide (a-$Si_{1-x}C_x$:H) can be deposited by Glow-discharge Chemical Vapour Deposition using CH_4 and SiH_4 gas mixture. Tawada *et al.* [1.37] showed that silicon-rich hydrogenated amorphous silicon carbide (a-SiC:H) possessing a wide band gap can be used in hydrogenated amorphous silicon (a-Si:H) solar cells as a p-type layer with promising higher conversion efficiency. Tabata *et al.* [1.38] showed that the band gap of a-$Si_{1-x}C_x$:H films can be controlled by varying the methane flow rate and also the process pressure. The experiment was performed in a HWCVD system using SiH_4, CH_4 and H_2 as precursor gases and it was shown that by increasing the methane flow rate from 4 to 20 sccm at low process pressure, Si-rich films with a slight change in the optical band gap ranging from 1.8 to 2.0 eV were obtained at a pressure of 2 Torr. Higher pressures of 4 Torr yielded films with optical gap varying from 1.9 eV to 2.3 eV when the carbon content in the films increased from 20 at. % to 60 at. %. The production of C-related precursors is required for higher values of C-content in the films. The process pressure is an important deposition parameter in this regard as it is a measure of the number of collisions between radicals that participate to the film growth.

UNIVERSITY of the
WESTERN CAPE

1.7 SiC as window layer in Solar cells

The production of electrical power by a solar cell is based on the photovoltaic effect where the sun's light induces a potential difference at a junction of two different materials. The sun rays strike a semiconductor material, which absorbs a portion of the sunlight. The absorbed light has enough energy to free electrons in the semiconductor. The freed electrons are directed by the induced potential difference towards a certain direction causing a current to flow in the cell. The current is then collected by metal contacts on the solar cell.

Fig. 1.4, illustrates a schematic band diagram of an ideal solar cell structure consisting of an absorber and semipermeable membranes. When light strikes the absorber (or intrinsic) layer, photons of this incident radiation are absorbed, creating electron-hole pairs within the layer. These electron-hole pairs are selectively separated by an electric field created between two semiconductor layers, a p-type and an n-type semiconductor, between which is sandwiched an absorber layer. A p-type semiconductor layer contains a larger concentration of holes compared to concentration of electrons, thus electrons diffusing from the absorber layer into the p-type semiconductor layer recombine with holes. Similarly the opposite holds for an n-type semiconductor. The p-type layer is also known as the window layer because light always enters through it whether the solar cell has an n-i-p or a p-i-n configuration.

UNIVERSITY of the
WESTERN CAPE

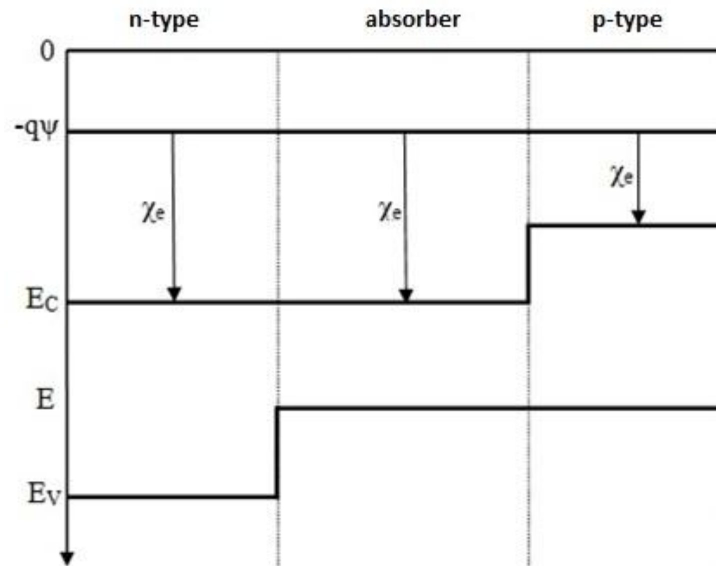

Figure 1.4: Band diagram of an idealized solar cell at the open circuit condition [1.39].

UNIVERSITY of the
WESTERN CAPE

In order to reduce the chance of electrons diffusing from the absorber layer to the p-layer, an energy barrier should be intr4oduced in the conduction band (CB), between the absorber layer and the p-layer. And this is possible by using a p-layer with a higher band gap than the absorber layer and with the energy difference of the two layers located in the conduction band. This energy difference in the p-layer requires that its electron affinity (χ_e) to be smaller than the absorber layer [1.39]. Since light passes through the p-type semiconductor before reaching the absorber layer, the p-type layer must be as transparent as possible to allow light through and become absorbed by the intrinsic layer. The advantage of using these window layers with high band gap is that they are capable of transmitting almost all photons to the absorber layer.

1.8 Aim and Outlines

The aim of our investigation is to study the structural properties of a-SiC:H thin films deposited by the Hot-Wire Chemical Vapor Deposition (HWCVD) using different analytical techniques. The use of low temperature of the substrate is sought for low cost photovoltaic devices; the films described in this thesis have been deposited using a temperature of the substrate as low as 280 °C.

The thesis is outlined as follows:

Chapter 1 consists of an introduction on silicon carbide alloy and its polytypes, its properties and how it can be used in photovoltaic thin films.

Chapter 2 gives brief overview of the Hot Wire Chemical Vapour Deposition process, a deposition method that has been used to process the films studied.

UNIVERSITY of the
WESTERN CAPE

Chapter 3 gives an overview on the analysis techniques employed in this thesis, namely Fourier Transform Infrared (FTIR) Spectroscopy, Raman Scattering, X-ray Diffraction, Elastic Recoil Detection Analysis (ERDA), Transmission Electron Microscopy as well as Atomic Force Microscopy.

In chapter 4, the influence of the filament temperature on the structural properties, the influence of the substrate heater temperature on the deposition rate were studied. We present there the results on hydrogen content and structural studies by FTIR. Lastly, we present and discuss the data on total hydrogen concentration obtained from ERDA measurements.

Chapter 5 is dedicated to the kinetic properties of hydrogen from effusion studies using in situ ERD; for this effect, we have monitored the retained hydrogen in the sample during a temperature ramp at a fixed rate. Coefficient constants at different temperatures of anneal were used to construct Arhenius plots; from these plots, activation energy and the diffusion pre-factor were determined.

At the end of the thesis, a summary of results and recommendation of future work are given.

UNIVERSITY of the
WESTERN CAPE

References

1.1. *Antoine Cesar Becquerel,* 2009. Available from <http://science.howstuffworks.com/dictionary/famous-scientists/chemists/antoine-cesar-becquerel-info.htm.> [22 February 2013].

1.2. K. Zweibel, P. Hersch, Basic Photovoltaic Principles and Methods, New York: Van Nosstrand Reinhold Company, Inc., 1984.

1.3. M.A. Green, 2000. Space Solar Cells and Arrays, Status of Crystalline Photovoltaic Technology. In: World Renewable Energy Congress VI, pp. 2630–2635.

1.4. W. Shockley, H.J. Queisser, Detailed balance limit of efficiency of p–n junction solar cells. Journal of Applied Physics 32 (3), (1961) 510–519.

1.5. R.R. King, D.C. Law, K.M. Edmondson, C.M. Fetzer, G.S. Kinsey, H.Yoon, R.A. Sherif, N.H. Karam, Appl. Phys. Lett. 90, (2007) 183516.

1.6. M.A. Green. Third generation photovoltaics: solar cells for 2020 and beyond. Physica E 14 (1–2), (2002) 65–70.

1.7. “What is the energy payback for PV?” January 2004, http://www.nrel.gov/docs/fy04osti/35489.pdf, 22 February 2013.

1.8. National Renewable Energy Laboratory Solar Energy Technologies Program, DOE/GO-102004-1847, (2004).

1.9. T.M. Razykov, C.S. Ferekides, D. Morel, Solar Energy 85 (2011) 1580–1608

1.10. X. C. Li, A. Golnas, F. Prinz, SPIE's 7th International Symposium on Smart Structures and Materials, Newport Beach, California. 2000.

1.11. H.F. Sterling and R.C.G. Swann, Solid-State Electron. 8 (1965) 653-654.

UNIVERSITY of the
WESTERN CAPE

1.12. Li Wang et al., Journal of Alloys and Compounds 290 (1999) 273–278.

1.13. Y. Komura, A. Tabata, T. Narita, A. Kondo, Thin Solid Films 516 (2008) 633–636.

1.14. B.P. Swain, Surface & Coatings Technology 201 (2006) 1132–1137.

1.15. D. Perrone, Process and characterization techniques on 4H-Silicon Carbide (Ph.D. Thesis), Politecnico di Torino, Torino, March 2007.

1.16. S. Janz, Amorphous Silicon Carbide for Photovoltaic Applications (Ph.D. Thesis), Fraunhofer Institute for Solar Energy Systems, Freiburg, Germany, (2006).

1.17. F. Liu, R. Maboudian, CS MANTECH Conference, May 17th-20th, Portland, Oregon, USA (2010).

1.18. X. Fu, J.L. Dunning, C.A. Zorman, M. Mehregany, Sensors and Actuators A, 119 (2005) 169–176

1.19. J. Deva Reddy, (2008), "Mechanical properties of Silicon Carbide (SiC) thin films". MSc Thesis. University of South Florida.

1.20. T. Chen, Y. Huang, A. Dasgupta, M. Luysberg, L. Houben, D. Yang, R. Carius, F. Finger, Solar Energy Materials & Solar Cells 98 (2012) 370–378.

1.21. P. Raback, "Modelling of the Sublimation Growth of Silicon Carbide Crystals" (Helsinki University of Technology, Helsinki, Finland, 1999).

1.22. A. Fissel, Physics Reports Volume 379, Issues 3–4 (2003) 149–255.

1.23. S.E. Stone, (2008), “A study of the effects of neutron irradiation and low temperature annealing on the electrical properties of highly doped 4H silicon carbide”, MSc Thesis, Graduate School of The Ohio State University.

1.24. W.Y. Ching, Y. Xu, P. Rulis, L. Ouyang, Materials Science and Engineering A 422 (2006) 147–156.

UNIVERSITY of the
WESTERN CAPE

1.25. K.L. Chopra, P.D. Paulson, V. Dutta, Prog. Photovolt: Res. Appl. 2004; 12:69–92.

1.26. Q. Wahab, L. Hultman, I.P. Ivanov, M. Willander, J.E. Sundgren, Thin Solid Films 261. (1995) 317-321.

1.27. B. Racine, A. C. Ferrari, N. A. Morrison, I. Hutchings, W. I. Milne, J. Robertson, J. Appl. Phys. 90, 5002 (2001).

1.28. L Pereyra, M.N.P. Carreho, Journal of Non-Crystalline Solids 201 (1996) 110-118.

1.29. J. Bullot and M.P. Schmidt, Phys. Status Solidi (b) 143 (1987) 345.

1.30. H. L. Juan, (2000), "Structural and electrical characterization of amorphous silicon carbide films (MSc Thesis), National University of Singapore. F. Demichelis, C. F. Pirri, E. Tresso. J. Appl. Phys. 72, 1327 (1982).

1.31. S. Miyajima, A. Yamada, M. Konagai, Thin Solid Films 501 (2006) 186-189.

1.32. C. Summonte, R. Rizzoli, M. Bianconi, A. Desalvo, D. Iencinella, J. Appl. Phys. 96, 3987 (2004).

1.33. W. Yu,W. Lu, L. Han, G. Fu, J. Phys. D: Appl. Phys. 37 (2004) 3304–3308.

1.34. H. Abderrazak, E.S.B.H. Hmida Silicon Carbide: Synthesis and Properties, Properties and Applications of Silicon Carbide, Rosario Gerhardt (Ed.), ISBN: 978-953-307-201-2, InTech, DOI: 10.5772/15736, (2011).

1.35. J. Meier, J. Spitznagel, U. Kroll, C. Bucher, S. Fay, T. Moriarty, A. Shah, Thin Solid Films 451 –452 (2004) 518–524.

1.36. J. Bullot, M. Gauthier, M. Schmidt, Y. Catherine, A. Zamouche, Philosophical Magazine Part B, Volume 49, Issue 5, (1984) 489 – 501.

1.37. T. Tawada, M. Kondo, H. Okamoto, Y. Hamakawa, Solar Energy Materials 6 (1982) 299–315.

UNIVERSITY of the
WESTERN CAPE

1.38. A. Tabata, M. Kuroda, M. Mori, T. Mizutani, Y. Suzuoki, Journal of Non-Crystalline Solids 338–340 (2004) 521–524.

1.39. TU Delft OpenCourseWare, “Solar Cell Operational Principles”, http://www.slideshare.net/DelftOpenEr/solar-cell-operational-principles#btnNext, 22 February 2013.

1.40. R. Cheung, (2006). Silicon Carbide Microelectromechanical Systems for Harsh Environments. Imperial College Press.

1.41. D.L. Staebler, C.R. Wronski, Appl. Phys. Lett., 31, 292.

1.42. H. Matsumura, Japanese Journal of Applied Physics, 25 (12), (1986) L949-L951.

1.43. R. Platz, S. Wagner, C. Hof, A. Shah, S. Wieder, and B. Rech, J. Appl. Phys. 84, 3949 (1998).

1.44. Semiconductor Materials for Solar Cells. March 2011. http://www.slideshare.net/DelftOpenEr/ch3-solar-cellmaterials.

1.45. K. Su Lim, O. Shevaleevskiy, Pure Appl. Chem., Vol. 80, No. 10, pp. 2141–2150, 2008.

1.46. S. Y. Myong, H. K. Lee, E. Yoon, K. S. Lim. J. Non-Cryst. Solids 298, 131 (2002).

1.47. R.E.I. Schropp and M. Zeman, "Amorphous and Microcrystalline Silicon Solar Cells--Modeling, Materials and Device Technology." Kluwer Academic Publishers, Boston, 1998.

1.48. R. Singh, S. Prakash, J. Phys., Vol. 61, No. 1, pp 121-129 (2003).

1.49. W. Van Sark, (2002) Handbook of Thin Film Materials, Volume 1: Deposition and Processing of Thin Films, Academic Press, Japan.

UNIVERSITY of the WESTERN CAPE

Chapter 2. Hot wire chemical vapour deposition systems

2.1 Introduction

Amorphous and nano-crystalline silicon carbide films were deposited using a Hot-Wire Chemical Vapour Deposition systems, designed by MVSystems Inc. [2.1]. This technique finds applications in the processing of material quality a-Si:H thin films with a low hydrogen content [2.2]. However its application for the development of material quality a-SiC:H or nc-SiC:H films has been of great interest as the growth mechanism of these films is challenging given the extra-complexity due to C alloying [2.3, 2.4, 2.5].

The HWCVD system in our laboratory is made up of two vacuum chambers: a load-lock and an ultra-high vacuum (UHV) chambers. The load-lock chamber, which can achieve a vacuum of ~1 x 10^3 mbar is designed in such a way that substrates can be loaded, brought in the UHV and retrieved from there without breaking the vacuum in the UHV reaction chamber; this is done by opening and shutting down the gate valve separating them and the transport is accomplished by a magnetic rod. The background pressure in the UHV chamber is capable of reaching values up to 10^{-9} mbar.

The load-lock chamber comprises of a substrate holder designed to carry two 10 x 10 cm^2 substrates. A track connecting both the load-lock chamber and the ultrahigh vacuum chamber transports the substrates between chambers. A full description of the chambers has been given by Arendse [2.1].

UNIVERSITY of the
WESTERN CAPE

2.2 Background on HWCVD

The HWCVD method was first introduced in 1979 by Wiensmann *et al.* [2.6] based on the principle that a heated tungsten or tantalum wire can be applied to thermally decompose the silane gas. The HWCVD method was later shown by Matsumura [2.7] that the decomposition of the silane (SiH_4) gas by the hot filament is a catalytic process, hence the term Catalytical Chemical Vapour Deposition (CTL-CVD).

Fig. 2.1 is the schematic representation of a cross-section HWCVD reaction chamber used in this study that shows some of the possible reactions that may take place from precursor gases that includes SiH_4, CH_4 and H_2. In the reaction during deposition, the precursor gases are let in and decomposed into its constituent radicals by the hot filament such as , which then reach the heated substrate. The radicals produced after the splitting of the precursor gases by the hot filament often reacted and recombined before being deposited on the substrate or on the growing film.

UNIVERSITY of the
WESTERN CAPE

It has been found by Song *et al.*[2.8] that the preparation of silicon carbide (SiC) thin films by HWCVD is problematic with the employment of CH_4 gas as a carbon source because the incorporation of C atoms into the SiC film is small and, consequently, results in a narrower optical band gap (less than 2.0 eV).

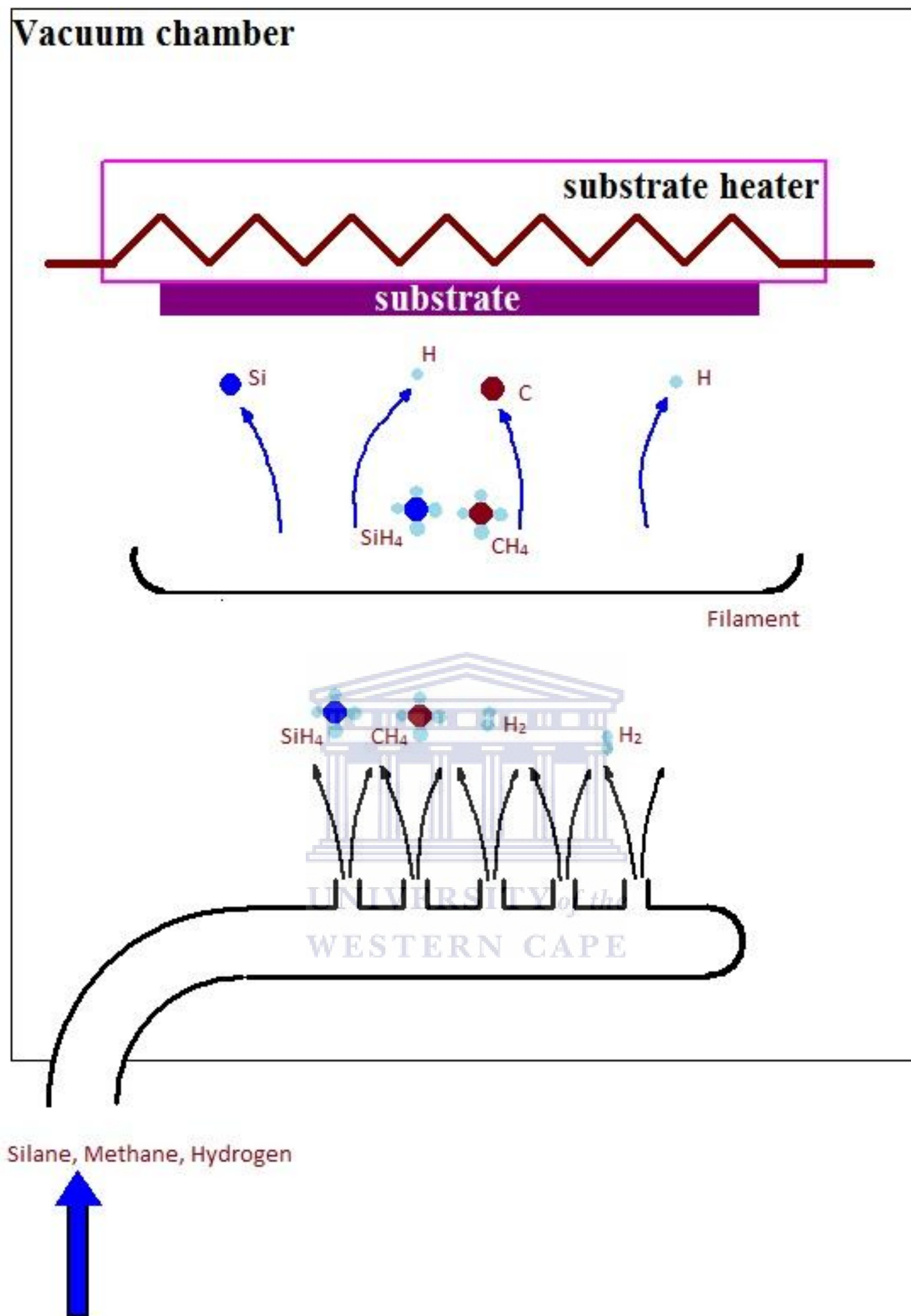

UNIVERSITY of the
WESTERN CAPE

Figure 2.1. *Schematic cross-section of the HWCVD chamber and the possible radicals formed after reaction with the hot filament.*

2.3 Thin film deposition

The substrates used in this study were crystalline silicon (c-Si) and corning 7059 glass of the size 2.5 cm x 2.5 cm. The substrates were ultrasonically in bath of acetone followed by methanol for 5 minutes respectively; in order to remove the native oxide from the c-Si substrates, they were thereafter dipped for one minute in a 5% HF acid solution. A de-ionized water bath can be applied at this stage before drying. The dried substrates were then inserted in the load-lock chamber. When the background vacuum in the load-lock has reached approximately 1 x 10^{-3} mbar, a gate linking the load lock to the UHV chambers is opened and the substrate holder is pulled in the UHV part by a magnetic rod.

UNIVERSITY of the
WESTERN CAPE

Once the background pressure in the UHV chamber is better than 1 x 10^{-7} mbar, the filament was set to the desired temperature by monitoring through a transparent side window by an optical pyrometer. Prior to deposition, the filament was etched by pure hydrogen gas to remove or decrease the crystalline defects on its surface for about 3-5 minutes with the shutter closed to block deposition on the substrate. The precursor gases were then introduced and the deposition pressure was set to its desired value. After the deposition pressure was reached, the shutter was opened for deposition of the film on the substrates. All samples were deposited for a given time and removed from the chamber after a slow cooling under vacuum in order to avoid oxidation. The deposited films on c-Si were used for FTIR, TEM, ERD and Raman scattering characterization methods while samples deposited on glass were used for optical and Raman scattering measurements.

References

2.1. C.J. Arendse, Hydrogenated amorphous silicon: Optical properties and hydrogen concentration, M.Sc. thesis, University of the Western Cape (1998).

2.2. A. H. Mahan, J. Carapella, B. P. Nelson, R. S. Crandall, I. Balberg, J. Appl. Phys., 69, (1991) 6728.

2.3. H. Shen ., T. Wu, Y. Pan, L. Zhang, B. Cheng, Z. Yue, Thin Solid Films 522 (2012) 36–39.

2.4. M.M. Kamble, V.S. Waman, S.S. Ghosh, A. Mayabadi, V.G. Sathe, T. Shripathi, H.M. Pathan, S.R. Jadkar, Bull. Mater. Sci., Vol. 36, No. 7, December 2013, pp. 1177–1185

2.5. T. Itoha, K. Fukunagaa, T. Fujiwaraa, S. Nonomurab, Thin Solid Films 430 (2003) 33–36

2.6. H. Wiesmann, A. K. Ghosh, T. McMahon, and M. Strongin, J. Appl. Phys. 50, 3752 (1979)

2.7. H. Matsumura, Japan. J. Appl. Phys. 25, L949 (1986).

2.8. Song, E.C. Cho, G. Conibeer, C. Flynn, Y. Huang, M.A. Green, Sol. Energy Mater. Sol. Cells 92 (2008) 474

UNIVERSITY of the
WESTERN CAPE

Chapter 3. Characterization Methods

3.1 Infrared Spectroscopy

3.1.1 Introduction

Fourier Transform Infrared (FTIR) spectroscopy is one of the most used spectroscopic techniques for structural characterization and the identification for elements in a sample. FTIR measurements are non-destructive and easy to perform, giving chemical analysis of samples with little preparation. In FTIR spectroscopy, spectra can be obtained either in absorption or in transmission mode. IR spectra arise due to molecular vibrational modes following interaction of infrared light with matter. Information on hydrogen incorporation in the deposited films and Hydrogen content in its associated bonding configurations can be revealed by FTIR spectroscopy [3.1].

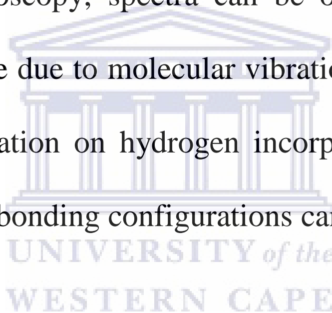
UNIVERSITY of the
WESTERN CAPE

3.1.2 Theory

Molecular vibration have frequencies in the IR region; the illumination of IR light will thus be resonant to vibrating molecules. A selective absorption will follow when one of the wavelengths of the radiation matches the frequency of the vibrating molecule. A molecule that contains two or more bonded atoms can undergo various modes of mechanical vibrations by absorbing frequencies equal to those of the molecular vibrations. A resulting spectrum allow not only to identify the nature of bonding but also the quantification by combining the integrated intensity

of the absorption band and known information on the thickness of the sample. The fundamental vibration of frequency for a diatomic molecule in terms of wavenumber $\bar{\nu}$ is given by;

$$\bar{\nu} = \frac{1}{2\pi c}\sqrt{\frac{k}{\mu}} \tag{3.01}$$

where k is the force constant of the oscillator and μ is the reduced mass of two particles and expressed as;

$$\mu = \frac{m_1 m_2}{m_1 + m_2}. \tag{3.02}$$

In addition to the above criterion of the matching between the vibrational/rotational frequency of the molecule and the absorbed electromagnetic radiation, a change in the magnitude and/or direction of the dipole moment must take place. Thus since infrared active molecular bonds need to have a dipole moment that changes as a function of time, symmetric bonds such as H_2 are not detectable in FTIR spectroscopy [3.2].

UNIVERSITY of the
WESTERN CAPE

In the electromagnetic spectrum, the infrared region is found in the wavenumber range of 13000 cm^{-1} to 10 cm^{-1}. The typical vibrational frequencies are in the range 10^{13} to 10^{14} Hz while the rotational frequencies are of the range 10^{10} to 10^{12} Hz which implies that these frequencies fall within the electromagnetic infrared spectrum region [3.3]. FTIR spectra in this thesis were collected in transmission mode using the Perkin-Elmer Pentagon 1000 FTIR Spectrophotometer in the wavelength range of 400-4000 cm^{-1} with a resolution of 4 cm^{-1}. An example of the obtained spectra is shown in Fig. 3.1. The thin films were deposited on c-Si substrates which is partially transparent to infrared light. The film transmission was obtained by subtracting the reference spectrum from that of the film on the c-Si substrate.

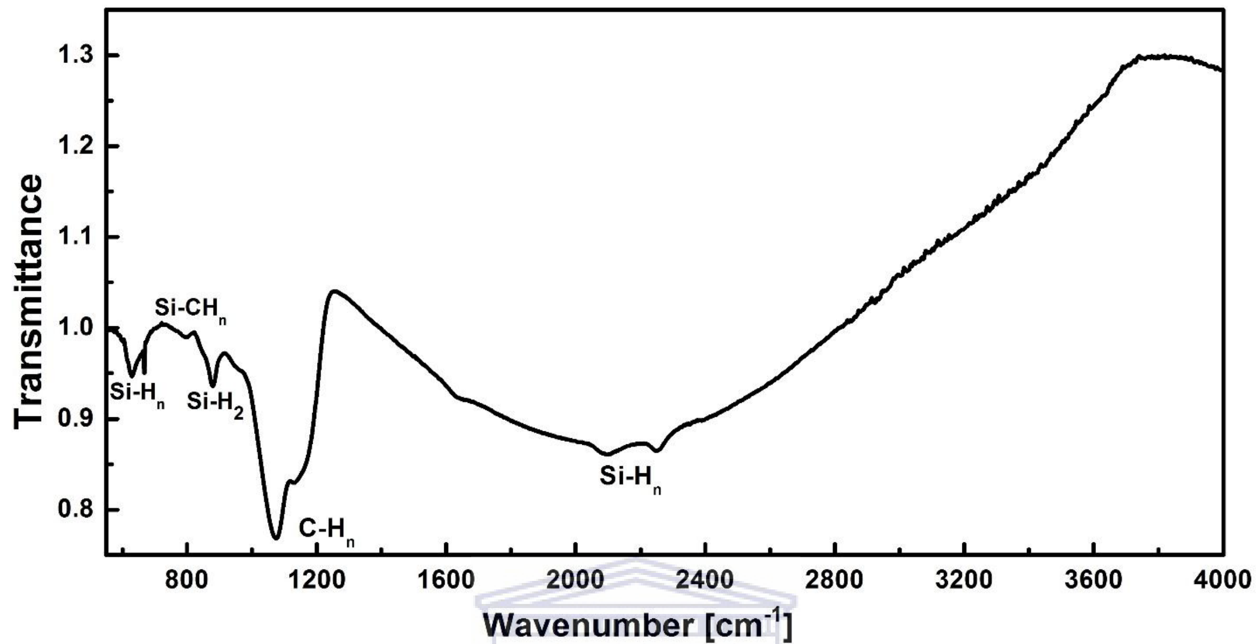

Figure 3.1. *An example of a spectrum taken from an a-SiC:H film.*

UNIVERSITY of the
WESTERN CAPE

Transmittance is defined as the ratio of the transmitted infrared beam (*I*) to the incident infrared beam on the sample (I_0).

$$T = \frac{I}{I_0} = e^{-kcl} \tag{3.03}$$

where *l* is the depth the transmitted beam travels; c is the concentration of the absorbing material; k is the absorption coefficient which corresponds to the imaginary part of the refractive index **n** and the dimensionless quotient $\frac{I}{I_0}$ is the transmittance *T*.

A linear expression of the transmittance is as follows,

$$log_{10}\left(\frac{I_t}{I_0}\right) = \varepsilon cl \tag{3.04}$$

where the constant $\varepsilon = k/\ln 10$ is known as the absorption cross-section; the term $log_{10}\left(\frac{I_t}{I_0}\right)$ is known as the absorbance.

3.1.3 Background Theory on Vibrational modes

The analysis of FTIR measurements is based on vibrational bonds in molecules within the observed samples. When an infrared radiation of a given frequency is absorbed by a molecule, i.e. the bond frequency matches the exact frequency of the infrared radiation, the molecule will vibrate according to a particular motion called vibrational modes. These molecular vibrations are said to be restricted to certain degrees of freedom. A molecule that is made up of N number of atoms has 3N degrees of freedom with motions in the three directions of the Cartesian plane. Additionally the molecule can vibrate in the three dimensions and this applies to rotational motions. For linear molecules only two degrees can describe rotational motion. Vibrations of non-linear and linear molecules result in 3N-6 and 3N-5 degrees of freedom respectively. Examples of vibrational modes for water (H_2O) and carbon dioxide (CO2) are illustrated in Fig. 2.2 as non-linear and linear molecules respectively, they are categorized in two major types: stretching and bending.

UNIVERSITY of the
WESTERN CAPE

In Fig. 2.2(a) we observe for the non-linear molecule H_2O with three atoms, three degrees of freedom (3(3)-6 = 3) that change either the bond lengths either the bond angles, classified as in-phase stretching, out-of phase stretching for the first and bending for the second.

In Fig. 2.2(b) for the linear CO_2 molecule with 3 atoms as well, four degrees of freedom (3(3)-5 =4) are obtained as in-phase stretching, out-of-phase stretching and 2 bending vibrations mutually perpendicular to each other.

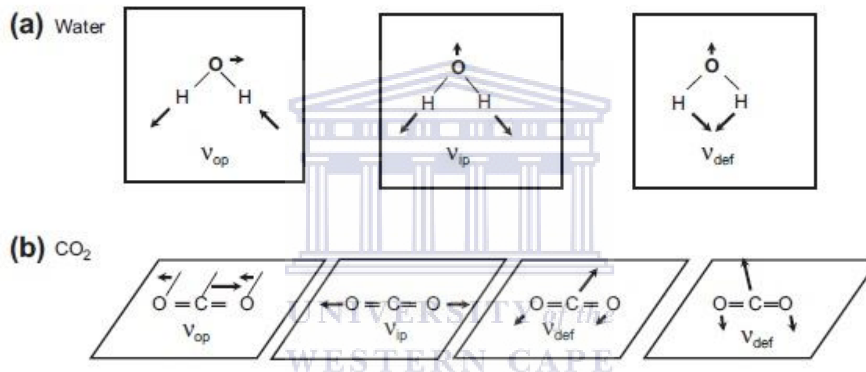

Figure 2.2. *Illustration of the normal mode of vibrations showing a change in atomic distances and bond angles in molecular motions of water (a) and of carbon dioxide (b).*

Since the absorption of an infrared radiation can cause molecules to vibrate in linear motion as well as rotational motion, absorption bands are observed instead of expected discrete lines, as absorption involves discrete and quantized energy levels [3.2].

3.1.4 Bonding in Silicon Carbide films

Silicon carbide films consist of various chemical bonds depending on the film composition, the stoichiometry and on the microstructure. All these listed characteristics are sensitive to the deposition conditions [3.4]. Table 2.1 lists the possible infrared absorption bands in amorphous and crystalline silicon carbide films that can be grouped in six spectral regions:

i. The Si-C stretching vibration mode at 670 cm^{-1} was assigned by Wierda *et al.* [3.5] and a broad band centered around 780 cm^{-1} is attributed to the Si-CH_3 rocking or wagging mode or to Si-C stretching mode [3.5, 3.6]. The center of this last band was observed to shift to higher wavenumbers in μc-SiC:H films and the shift was attributed to a variation in the electronegativity of the bonded atoms [3.7, 3.8].

ii. The band in the spectral region between 950 and 1100 cm^{-1} is assigned to the CH_n rocking or wagging vibration modes. [3.9].

UNIVERSITY of the
WESTERN CAPE

iii. The well-known stretching vibration of Si-H at 2000 cm^{-1} shifts toward 2100 cm^{-1} due to the presence of nearest neighbor C atoms [3.10]. The 2100 cm^{-1} is partially attributed to the SiH_2 groups also found in the spectral region between 845 and 890 cm^{-1}.

iv. The spectral region between 1500 and 1600 cm^{-1} is attributed to the C=C (sp^2) stretching mode [3.11].

v. The spectral region between 2800 and 3000 cm^{-1} is attributed to the CH_n stretching modes with peaks centered at 2880 cm^{-1} from the C-H_n (sp^3) stretching mode; this band is reportedly been found in a-SiC:H films with high C content having a diamond like structure. The band centered around 2960 cm^{-1} is due to C-H (sp^2) stretching mode found in films with high C incorporation having a graphitic like structure [3.12, 3.13].

vi. The well-known band centered around 640 cm^{-1} is attributed to the Si–H_n wagging or rocking modes and is known to account for the combination of the 2000, 2090 and 2100 cm^{-1} centered peaks and can employed in order to evaluate the total hydrogen bonded to silicon in the films [3.14].

Table 3.1. *Infrared absorption bands in a-SiC:H and nc-SiC:H and their assignments.*

Bonding	**Wavenumber (cm^{-1})**	**Assignment**
Si-H	630 – 650	Wagging
Si-CH_3,	750 – 790	Wagging
Si-C	800	Stretching
Si-H_2	845 – 900	Bending
C-H_n	960 – 1050	Wagging, Rocking
Si-O-Si	1100	Stretching
Si-CH_3, Si-CH_2	1250-1350	Bending
C=C (sp^2)	1500 – 1600	Stretching
Si-H_n	2000-2100	Stretching
C-H_n (sp^3)	2880	Stretching
C-H (sp^2)	2960	Stretching

UNIVERSITY of the WESTERN CAPE

Fig. 3.3 shows major vibrational modes commonly found in IR spectroscopy

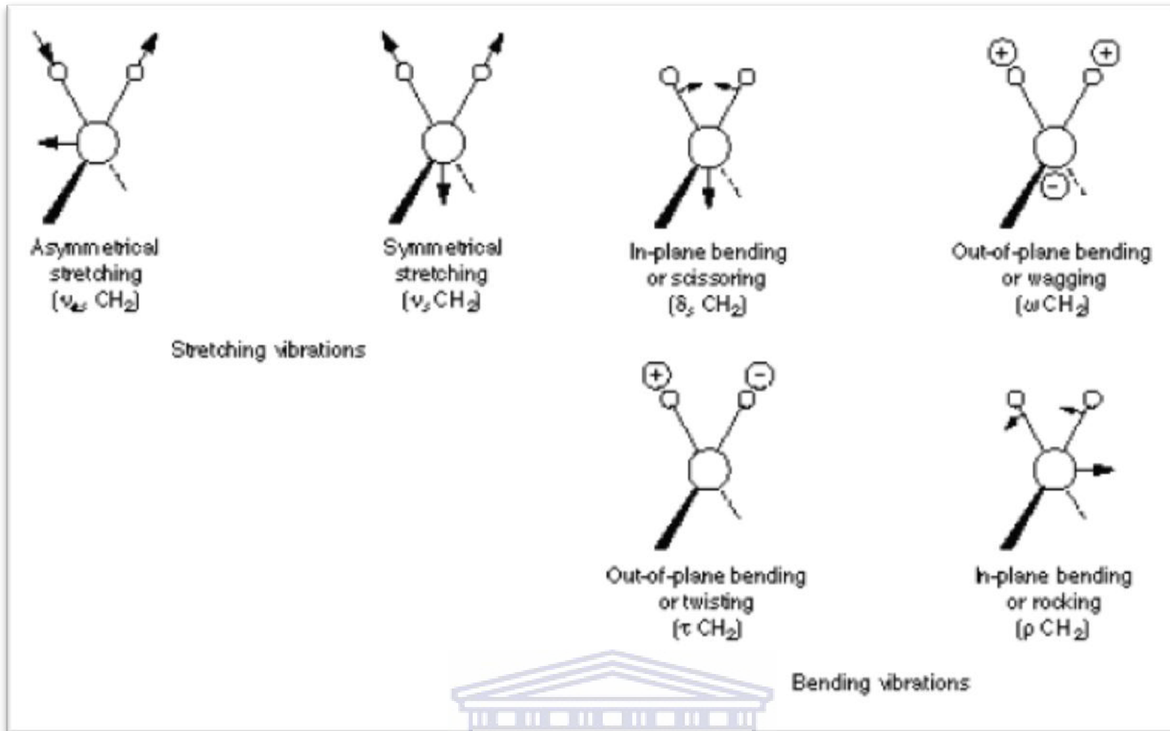

Figure 3.3. *Major vibrational modes for a nonlinear group, CH_2. The + sign indicates motion from the plane of page toward the reader; – sign indicates motion from the plane of page away from the reader [3.2].*

UNIVERSITY of the
WESTERN CAPE

3.1.5 Determination of Hydrogen and Silicon Carbide concentration in the Deposited Films

Hydrogen inclusion in the films deposited at low substrate temperatures using precursor gases such as silane (SiH_4) and methane (CH_4) is expected, since both source gases consist of molecules with four hydrogen atoms per molecule. Hydrogen atoms are known to passivate and reduce the number of dangling bonds in a-Si-C network that act as recombination sites; the bonds breakage is caused by the irregular atomic arrangement of silicon atoms in the amorphous

layer. The passivation of dangling bonds by hydrogen incorporation in the amorphous layer positively influences the structure of the films, reducing the defect density in the material and consequently improving the electronic and optoelectronic properties of the material. The reduction of the defect density in the material allows for an increase in the doping efficiency of the material, making it useful as p- or n-type doped layers [3.14].

Hydrogen concentration in samples by FTIR spectroscopy is generally determined from the integrated absorption intensity of the Si-H_n and C-H_n bands centered around 640 cm^{-1} and 2800 – 3000 cm^{-1} respectively following by the equation

$$I_{x-H} = \int_{-\infty}^{+\infty} \frac{\alpha(\omega)}{\omega} d\omega \qquad x = Si, C \tag{3.05}$$

where α(ω) is the infrared absorption coefficient and ω is the frequency. Bond densities of Si-H_n and C-H_n, i.e. the concentration of oscillators in the film, determine the bonded hydrogen concentration of the films; they are given by the product of the integrated absorption intensity of the infrared excited peaks and the absorption cross-section given by,

$$N_{x-H} = A_{x-H} I_{x-H} \qquad x = Si, C \tag{3.06}$$

where A_{x-H} represents the absorption cross-sections of Si-H and C-H vibration bonds. The absorption cross section and the film thickness are both required for the evaluation of H content in the samples. The absorption cross-section constants are $2.1 \times 10^{19}\ cm^{-2}$ for Si-H band at 640 cm^{-1} and $1.35 \times 10^{21}\ cm^{-2}$ for C-H band at between 2800 – 3000 cm^{-1} as obtained from literature [3.15, 3.16]. The absorption cross-section constant for the C-H band at 960-1100 cm^{-1} has not been reported in literature and thus was suggested in this investigation. Both the

UNIVERSITY of the WESTERN CAPE

procedure and the obtained results are discussed in section 3. The hydrogen concentration is calculated by,

$$C_H = \frac{N_{Si-H}}{N_{Si} + N_{Si-H}} \times 100\% \tag{3.07}$$

N_{Si} represents the density of silicon atoms and is given by 5 x 10^{22} cm^{-3} [17]. The amount of Si-C bonds ($N_{Si\text{-}C}$) can also be determined by Eqn. 3.06 where by it can be rewritten as,

$$N_{Si-C} = A_{Si-C} I_{Si-C} \tag{3.08}$$

where I_{Si-C} is the integrated absorption intensity of the Si-C bonds and A_{Si-C} is the absorption cross-sections of Si-C band centred at 800 cm^{-1} equal to $2.13 \times 10^{19}\ cm^{-1}$ [3.18].

Brodsky *et al.* [3.19] introduced the Brodsky-Cardona-Cuomo (BCC) method used in FTIR spectroscopy to calculate hydrogen concentration from Si-H wagging/rocking bond at 640 cm^{-1}. However the BCC method does not account for errors accumulated from the interference fringes that may occur through the mismatch of refractive indexes of the deposited layer and the substrate. Maley [3.20] developed a method that corrected the BCC method and was able to perform accurately baselines fit of the coherent and incoherent multiple reflections in the film and the substrate respectively. This method was however developed for a-Si:H films, therefore its use in a-SiC:H should be implemented cautiously with respect to C inclusion. The overly estimated value of the absorption coefficient was corrected by relating α_{BCC} to the measured transmission T(ω) by [3.19];

$$T(\omega) = \frac{4T_0 e^{-\alpha_{BCC} d}}{[(1 + T_0)^2 - (1 - T_0)^2 e^{-2\alpha_{BCC} d}]} \tag{3.09}$$

UNIVERSITY of the
WESTERN CAPE

where d is the film thickness and T_0 the baseline transmission which is equal to 0.54 for c-Si (substrate).

The corrected absorption coefficient due to the effect of the coherent reflections in the deposited layer is given by [3.20];

$$\alpha_{TRUE} = \frac{\alpha_{BCC}}{1.72 - 12\omega d}\ , for\ \omega d \leq 0.06 \tag{3.10}$$

or,

$$\alpha_{TRUE} = \alpha_{BCC}\ , for\ \omega d > 0.06 \tag{3.11}$$

3.2 Elastic Recoil Detection Analysis

3.2.1 Introduction

Elastic Recoil Detection Analysis (ERDA) is a widely used non-destructive ion beam technique for depth profiling of light elements in solid state materials. Hydrogen and Deuterium concentration profiles can be determined by ERDA technique utilizing particles with energies of a few MeVs as projectile in samples up to thicknesses of a few microns.

3.2.2 Background theory of ERDA

The working principle of an elastic recoil detection experiment is based on the analysis of recoiled lighter target atoms ejected from a sample by a heavier high-energy ion beam. In this

investigation ERDA is used to determine hydrogen concentrations in the deposited films. Basically a spectrum taken from an ERDA experiment involves two events where energy is transferred from the incident particle to the target atom and the loss of energy experienced by incident beam and the recoiled atoms [3.21].

Fig. 3.4 shows a schematic representation of an elastic collision between the incident beam consisting of projectile ions with mass M_1 and energy of E_0 and a target atom of mass M_2 initially at rest, which are scattered at an angle φ and their energies measured by a detector. The elastic recoil process can be expressed using the physics of kinematics of elastic collisions.

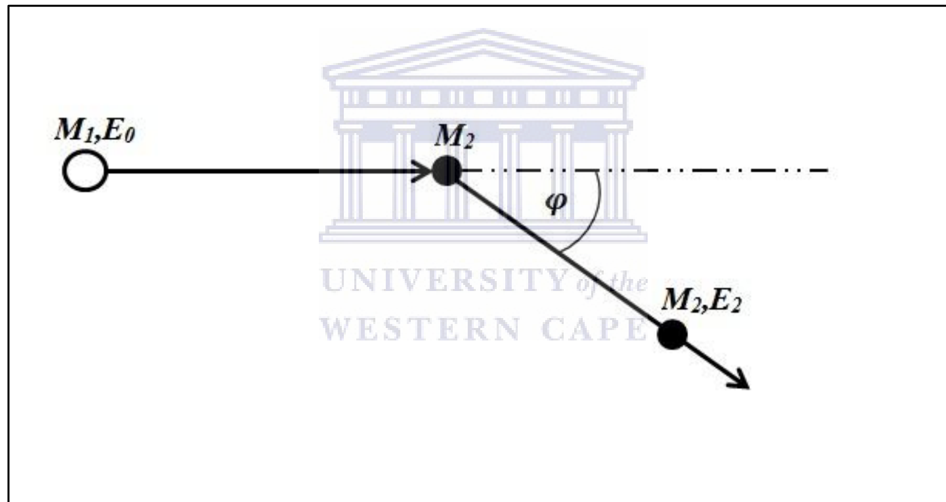

UNIVERSITY of the
WESTERN CAPE

Figure 3.4. *Basic schematic representation of the elastic recoil process of two masses showing the geometry of a scattering experiment.*

From the conservation of energy and momentum, the ratio of the recoiled and the projectile energies, also known as the kinematic factor is given by Eqn 3.12;

$$K = \frac{E_2}{E_0} \tag{3.12}$$

where E_0 is the energy of the projectile ion and E_2 is the energy of the recoil.

The kinematic factor determines the amount of energy E_2 transferred to the recoil nucleus and is derived from the law of conservation of energy and momentum and is given by [3.22];

$$K = \frac{4M_1M_2}{(M_1 + M_2)^2} cos^2 \varphi \tag{3.13}$$

where φ is the grazing angle of the projectile and $M_1$and M_2 denotes the primary and recoil particles respectively.

During the elastic collision process, the probability that a target atom will be knocked off from the sample by a projectile particle and scattered in such a way that it is directed towards the energy detector is described by the Rutherford differential scattering cross section and is given by [3.21];

$$\frac{d\sigma}{d\Omega} = \left(\frac{Z_0Z_2e^2}{2E_0}\right)^2 \left(1 + \frac{M_0}{M_2}\right)^2 \frac{1}{cos^3\varphi} \tag{3.14}$$

where e is the charge of an electron and Ω is the solid angle subtended by the detector. $\sigma(\varphi)$ is the scattering cross section defined as the average differential scattering cross section given by [3.22];

$$d\sigma = \frac{1}{\Omega}\int_{\Omega} \frac{d\sigma}{d\Omega} \cdot d\Omega. \tag{3.15}$$

where Ω is the small detector solid angle.

The solid angle for the small detector with an active area A at a distance l from the target is defined is given by:

$$\Omega = \frac{A}{l^2} \tag{3.16}$$

It is expressed in steradians. The measure of the atomic concentration of the target atoms is related to the cross section. The yield, which is the number of detected target particles Q_D is dependent on the number of target atoms per centimeter square N_s and is given by;

$$Q_D = \sigma(\varphi)\Omega Q N_s \tag{3.17}$$

where $\sigma(\varphi)$ is the differential cross section, and Q is the number of the projectiles, determined by the time integration of the current of charged particles incident on the target.

3.2.3 The experimental set up

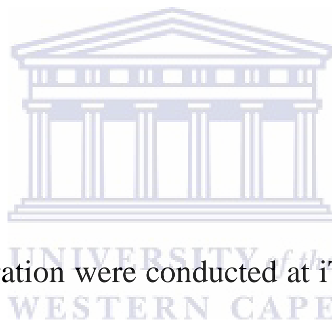
UNIVERSITY of the
WESTERN CAPE

ERDA experiments in this investigation were conducted at iThemba LABS in Cape Town using a Van de Graaf accelerator. Alpha particles ($^4He^{++}$) of energies in the range of 2 and 3 MeV were used as projectile particles, the chamber was pumped down to pressures lower than 10^{-4} mbar before irradiation and an Al coated Si detector was used for measuring scattered hydrogen atoms.

Fig. 3.5 shows a basic set-up for ERD measurements. During the experiment, incident alpha particles of 3 MeV are directed towards the target material placed at a grazing angle $\phi = 15°$ and recoil hydrogen atoms from the deposited layer. The scattered alpha particles are prevented from reaching the detector by a Mylar stopper foil placed in front of the detector. The Mylar foil has enough stopping power for He in this range of energy but it is transparent to the recoiled H nuclei due to their smaller mass.

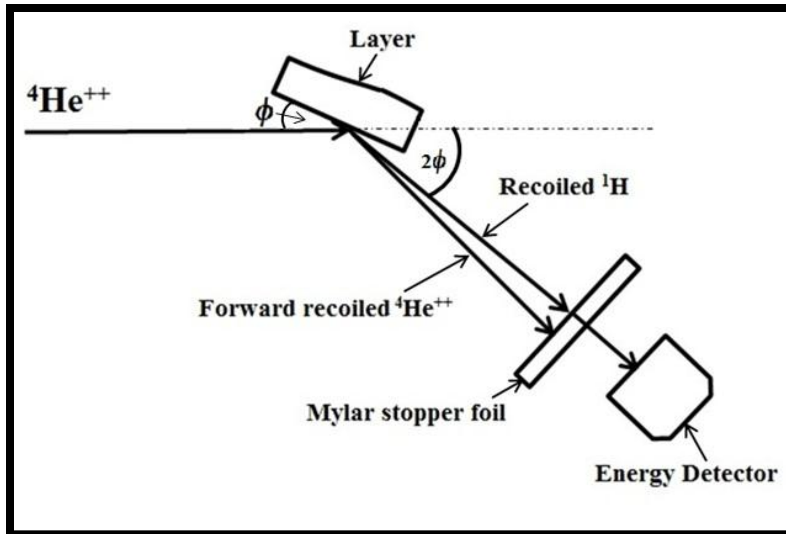

Figure 3.5. *Schematic representation of a basic experimental setup for ERDA measurements where the sample is by tilted by an angle of* $\phi = 15°$ *with respect to the incident the recoiled nuclei are scattered at an angle of* 2ϕ *with respect to the direction of the incident beam.*

UNIVERSITY of the
WESTERN CAPE

The detected recoiled hydrogen particles are generated into electronic signals that are amplified and processed by analogue and digital electronics. The electronic signals are then sorted and stored in different band channels according to their energies. The correlation between the channel number and the energy of the recoiled nuclei is done by recording spectra from He+ projectiles accelerated at least with three different energies.

A Mylar foil ($C_{10}H_8O_4$) was used in order to perform an energy-channel calibration by bombarding the foil with beam energies of 2, 2.5 and 3 MeV.

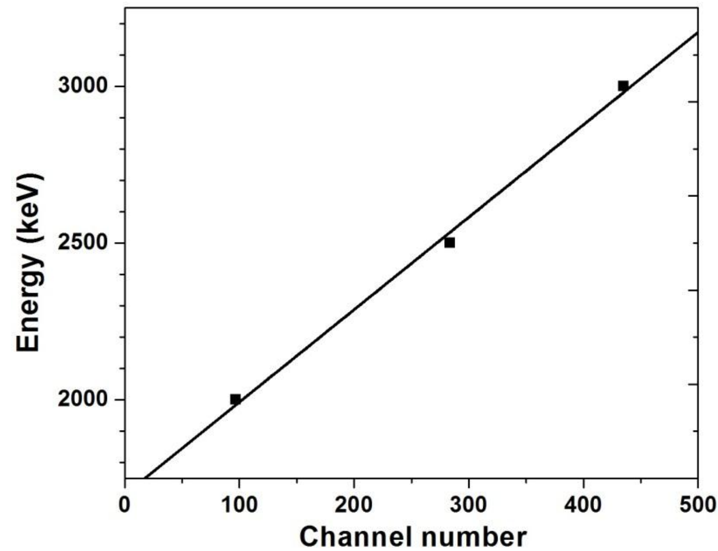

Figure 3.6. *Energy-channel calibration experiment displaying three points obtained from three different He beam energies of 2, 2.5 and 3 MeV. The energies of the recoiled H from the surface were stored in the 97, 284 and 435 channels respectively.*

UNIVERSITY of the
WESTERN CAPE

An example of the calibration for one of our experiments is shown in Fig. 3.6 where a graph of energy versus channel number is plotted. The cut-off on the energy axis gives the energy offset. The linearity of the detector can be described by the equation;

$$E\ [keV] = A * channel + B \tag{3.18}$$

where E is the calculated particle's energy, the slope A will give energy per channel factor and B gives the energy offset. The depth profiles of the deposited films were determined from ERDA measurements where all spectra were accumulated from the same measurement ladder as the Kapton ($C_{22}H_{10}N_2O_5$) for channel-energy calibration of the system.

3.2.4 Real Time-ERD

Real-time ERDA (RT-ERDA) is a relatively new technique used to determine the diffusion mechanism of light elements in thin films [3.23]. RT-ERDA is able to determine the kinematic parameters, activation energy (E_a) and pre-exponential factor, from a single ramped anneal. In this study, RT-ERDA offers the advantage to determine kinetic parameters i.e. the activation energy (E_a) and pre-exponential factor, from a single ramped anneal. In this study, RT-ERDA was used in determining the behavior of hydrogen in a-SiC:H films by studying the kinematic effects during isochronal annealing of the films.

UNIVERSITY of the
WESTERN CAPE

3.2.3.1 Background on Kinematics Studies by Real Time-ERD

In the hydrogen evolution experiment, the temperature is raised monotonically with the time and the evolution rate dN/dt is measured. For a diffusion limited evolution, hydrogen concentration profile $C(x,t)$ across the film must be compatible with the diffusion equation;

$$\frac{\partial c}{\partial t} = D(t)\frac{\partial^2 c}{\partial x^2} \tag{3.19}$$

where D is a time-dependent diffusion coefficient $D(T(t))$. For a typical diffusion out of a plane sheet of thickness l, through which the diffusing substance is initially uniformly distributed and the surface of which is kept at zero concentration, the conditions are

$$C = C_0, \qquad 0 < x < L, \qquad t = 0 \tag{3.20}$$

$$C = 0, \qquad x = 0, \qquad x = L, \qquad t > 0 \tag{3.21}$$

The solution to the diffusion equation is given [3.24]

$$C = \frac{4C_0}{\pi}\sum_{n=0}^{\infty}\frac{1}{2n+1}exp\left\{-Dt\left(\pi\frac{2n+1}{L}\right)^2\right\} * \sin\left(\frac{2n+1}{L}\pi x\right) \tag{3.22}$$

For $D.t > 0$ and in the approximation $n = 0$

$$C = \frac{4C_0}{\pi}exp\left(-Dt\frac{\pi^2}{L^2}\right) * \sin\left(\frac{\pi x}{L}\right) \tag{3.23}$$

The average concentration of retained hydrogen is

$$C_{av} = \frac{1}{L}\int_o^L \frac{4C_0}{\pi}exp\left(-Dt\frac{\pi^2}{L^2}\right) * \sin\left(\frac{\pi x}{L}\right)\, dx \tag{3.24}$$

$$C_{av} = \frac{8C_0}{\pi^2}exp\left(-Dt\frac{\pi^2}{L^2}\right) \tag{3.25}$$

We can write,

UNIVERSITY of the
WESTERN CAPE

$$Dt = \frac{L^2}{\pi^2}\ln\frac{8C_0}{C_{av}\pi^2} \tag{3.26}$$

The ramp constant is given by,

$$\beta = \frac{T - T_0}{t} \tag{3.27}$$

Therefore,

$$D = \frac{\beta L^2}{(T - T_0)\pi^2}\ln\left(\frac{8C_0}{C_{av}\pi^2}\right) \tag{3.28}$$

As all the parameters featuring on the right of Eqn. 3.28 are either constants or can be determined experimentally, $D(t)$ can be determined.

But,

$$D = D_0 \, e^{-E_a/kt} \tag{3.29}$$

The best linear fit of the Arhenius plot $D \sim 1/T$ yields both D_0 and E_a.

3.2.3.2 Experimental set up for Real-time ERDA measurements

The RT-ERDA set up is the same as that of normal ERDA with respect to the geometry, with a difference in that for RT-ERDA, the set up consists of a heating plate which acts as a substrate holder, as shown in Fig. 3.7. The heating plate has a thermocouple attached to it for measurement of the temperature. The substrate with its back attached by a conducting silver paste to the heating plate is assumed to possess the same temperature as the heated plate during annealing.

UNIVERSITY of the
WESTERN CAPE

Figure 3.7. *A RT-ERDA set up at iThemba LABS for isochronal annealing of a-SiC:H films.*

3.3 Raman Spectroscopy

3.3.1 Introduction

Raman spectroscopy is a non-destructive technique used for material identification and determination of the structural properties of the materials such as crystallinity of the films by the measure of its crystalline volume fraction [3.25]. Features obtained in a Raman spectrum are also used to estimate the degree of stress and disorder in thin-films [3.26]. Raman scattering arises from an inelastic scattering process when a sample is irradiated by intense laser beams in the UV-visible region. In Raman spectroscopy the vibrational frequency is measured as a shift from the incident beam frequency. Raman spectroscopy was used in the investigation to study the structural nature of the deposited films. The a-SiC:H and μc-SiC:H films were deposited on Corning 7059 glass substrates for Raman measurements.

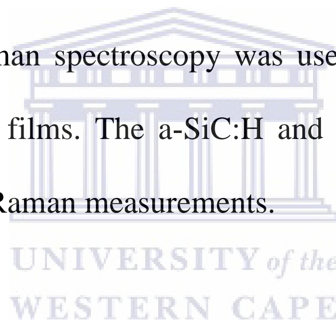
UNIVERSITY of the
WESTERN CAPE

3.3.2 Theoretical background

When an incident beam strikes a sample, the scattered light consists of two types. The 1st process where the incident light is elastically scattered is called Raleigh scattering, the scattered photons have thus the same energy as that of those in incident beam. Due to an exchange in energy with the molecule, the scattered light can be of higher or lower frequency than the incident, the process is then called Raman scattering. The molecule is thus said to be in a higher or lower vibration state depending on original state of the molecule before the interaction with light. In Raman scattering, the two processes which describes a shift of frequency are named Stokes and

anti-Stokes scattering. Stokes scattering occurs when the frequency of light is decreased or shifted down after interaction with the sample; phonon emission occurs in this process. Anti-stokes scattering occur if there is an up-shift in the frequency and phonon absorption takes place during this process. Phonons are vibrations of the atoms in a crystal lattice that contain resonant frequencies in the infrared spectral region, and they are used to describe vibrational or acoustic energy in quantum mechanical form [3.27].

The law of conservation of energy and momentum in Raman process can be written:

$$v_{incident} = v_{Raman} \pm v_{phonon} \tag{3.30}$$

and

$$k_{incident} = k_{Raman} \pm k_{phonon} \tag{3.31}$$

UNIVERSITY of the
WESTERN CAPE

where the + sign illustrates Stokes scattering and the – sign corresponds to anti-stokes scattering [3.27]. Fig. 3.8 illustrates a schematic the Stokes scattering process.

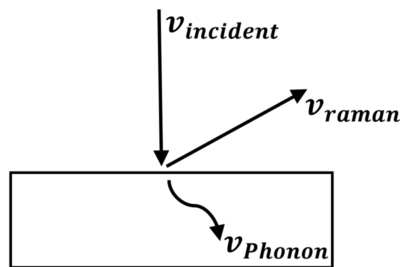

Figure 3.8. *The Stokes scattering as represented by a down-shift in frequency and a phonon is emitted during the process.*

As molecules are most of the time in their ground state and energy is required to be absorbed from the system for anti-Stokes scattering, this process is unlikely at room temperature. In contrast there is no temperature condition needed to satisfy the Stokes scattering process. The ratio of intensity of anti-Stokes to Stokes scattering events dependent of the number of molecules in the ground and excited vibrational levels can be written as [3.43];

$$\frac{N_n}{N_m} = \frac{g_n}{g_m} exp(-(E_n - E_m)/k_B T) \quad (3.32)$$

where N_n is the number of molecules in the excited vibrational energy level (n), N_m is the number of molecules in the ground vibrational energy level (m), g is the degeneracy of the levels n and m, $E_n - E_m$ is the difference in energy between the vibrational energy levels, k_B is Boltzmann’s constant. By the study of the frequency of lattice vibration also known as phonons as well as of the intensity of the detected inelastically scattered beam, Raman is used as a complementary technique to FTIR.

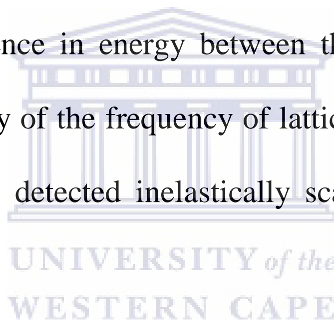
UNIVERSITY of the
WESTERN CAPE

The selection rule for modes to be Raman active requires that the polarizability of the induced dipole must change.

When an incoming beam in the form of electromagnetic wave interacts with an optical medium; neglecting the magnetic effects, the induced dipole moment P is given by;

$$P = \alpha E \quad (3.33)$$

where α is the polarizability and E is the strength of the electric field of the incoming electromagnetic wave. The proportionality constant α is a material property that depends on the molecular structure and nature of the bonds. The time (t) dependent electric field can be written;

$$E = E_0 \cos 2\pi\nu_0 t \quad (3.34)$$

where E_0 is the vibration amplitude. The dipole moment can thus be written:

$$P = \alpha E_0 \cos 2\pi\nu_0 t \tag{3.35}$$

The nuclear displacement $q(t)$ as response to the changing $E(t)$ in a molecule vibrating at a frequency ν_i can be expressed as;

$$q = q_0 \cos 2\pi\nu_i t \tag{3.36}$$

where q_0 is the maximum vibrational amplitude. For small amplitudes of vibration, the polarizability can be expressed by a Taylor series expansion such that α is a linear function of q and is given by;

$$\alpha = \alpha_0 + \left(\frac{\partial\alpha}{\partial q}\right)_0 q \tag{3.37}$$

where α_0 is the polarizability at equilibrium position and $\left(\frac{\partial\alpha}{\partial q}\right)_0$ is the rate of change of α with respect to the change in q evaluated at the equilibrium position. Now by substituting Eqn. 3.36 into Eqn. 3.37 we end up with the polarizability given by;

UNIVERSITY of the WESTERN CAPE

$$\alpha = \alpha_0 + \left(\frac{\partial\alpha}{\partial q}\right)_0 q_0 \cos 2\pi\nu_i t. \tag{3.38}$$

Finally when Eqn. 3.38 is substituted into Eqn. 3.35, the dipole moment is now given by;

$$P = \alpha_0 E_0 \cos 2\pi\nu_0 t + \left(\frac{\partial\alpha}{\partial q}\right)_0 q_0 E_0 \cos 2\pi\nu_0 t\, cos 2\pi\nu_i t. \tag{3.39}$$

Using the trigonometric identities, Eqn. 3.39 can be written as;

$$P = \alpha_0 E_0 \cos 2\pi\nu_0 t + \frac{1}{2}\left(\frac{\partial\alpha}{\partial q}\right)_0 q_0 E_0 \{\cos[2\pi(\nu_0 + \nu_i)t] + \cos[2\pi(\nu_0 - \nu_i)]t\}. \tag{3.40}$$

The first term represents an oscillating dipole of frequency $\nu_0$of the original beam (i.e. the Rayleigh scattering), while the second term represents the Raman scattering as anti-Stokes for $\nu_0 + \nu_i$and Stokes for $\nu_0 - \nu_i$.

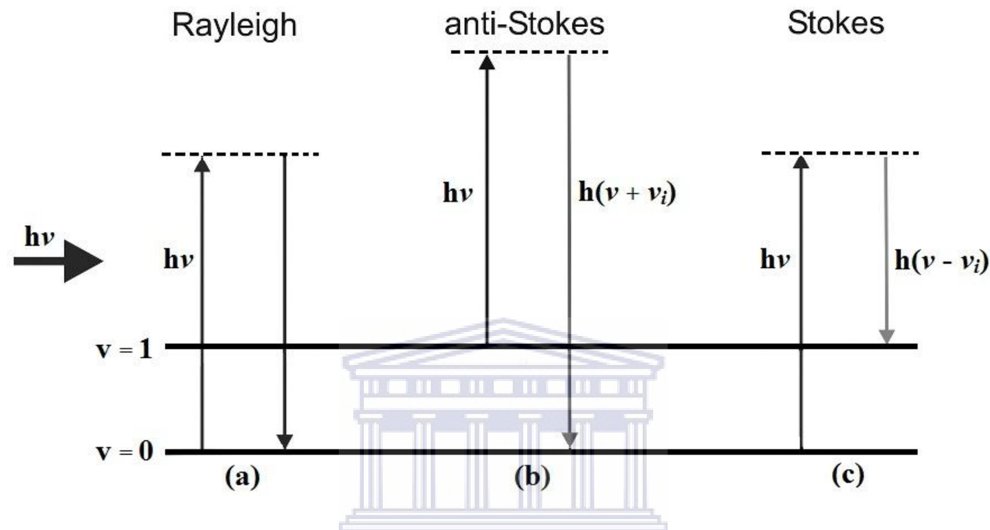

Figure 3.9. *Energy diagram representing elastic Raleigh scattering (a) and inelastic Raman scattering whereby in the process, a shorter wavelength is deflected, known as anti-Stokes (b) and a longer wavelength is deflected is known as Stokes Raman scattering (c).*

UNIVERSITY of the
WESTERN CAPE

From Eqn. 3.40, it can be stated that if $(\partial\alpha/\partial q)_0$ is zero, the vibration is not Raman active; to be thus Raman active, it must be a change in the rate of the polarizability.

3.3.3 Thin films applications

The Raman Spectroscopy can be used in determining phonon modes related to hydrogenated amorphous silicon carbide (a-SiC:H) and hydrogenated nanocrystalline silicon carbide (nc-SiC:H) in the range between 100 – 1600 cm^{-1}. However a band around 1500 cm^{-1} attributed to phonon density of states of amorphous graphite is usually obtained in samples with high carbon content [3.28]. It was suggested by Tessler *et al.* [3.29] that this band around 1500 cm^{-1} can be attributed to C-C bonds in sp^3 configuration. The characterization of samples using Raman spectroscopy in this thesis was done in the wavenumber range of 100 – 1100 cm^{-1} since the samples observed revealed no indication of the presence of graphitic contributions as discussed in section 3 of results and discussions.

In addition, a shift to lower or higher wavenumbers from the Si (TO) peak is known to be caused by polytypism in SiC thin films. For example, 6H-SiC crystallites are known to be found at ~965 cm^{-1} due to LO mode with corresponding double peaks at 767 cm^{-1} and 789 cm^{-1} due to modes, [3.44], while 3C-SiC modes are expected at ~794 cm^{-1} and at ~ 968 cm^{-1} for TO and LO modes [3.45].

UNIVERSITY of the
WESTERN CAPE

Phonon modes characteristic to hydrogenated amorphous silicon (a-Si:H), hydrogenated microcrystalline silicon (μc-Si:H), hydrogenated amorphous silicon carbide (a-SiC:H) and micro- or nanocrystalline (μc-SiC:H/nc-SiC:H) are found having bands illustrated in Table 3.2. These phonon modes can be grouped together because Raman spectroscopy is capable of identifying homo-nuclear phases in silicon carbide related films [3.8].

Deposition conditions are the key factors in the incorporation of different bonding modes; thus all listed bands in Table 3.2 will not be necessarily observed.

Table 3.2. *Raman scattering of Si-C related bands* [3.30, 3.31, 3.32]

Bonding	**Wavenumber (cm^{-1})**	**Phonon modes**
a-Si	160	Transverse acoustic (TA)
a-Si	330	Longitudinal optical (LA)
Si-Si	480	Transverse optical (TO)
c-Si	520	Transverse optical (TO)
c-Si	970	Transverse optical (TO)
Si-C	790	Transverse optical (TO)
Si-C	940-980	Longitudinal optical (LO)

UNIVERSITY of the
WESTERN CAPE

3.3.4 Structural Characterization in Raman Spectroscopy

The crystalline volume fraction X_C, as defined in Eqn. 3.41 is widely used to quantify the amount of crystallinity in the amorphous Si network.

$$X_C = \frac{I_{500} + I_{520}}{I_{480} + I_{500} + I_{520}} \tag{3.41}$$

where I_{480}, I_{500}, and I_{520} are the integrated intensities of the amorphous, intermediate and crystalline peaks centered at wavenumbers 480 cm^{-1}, 500 cm^{-1}, and 520 cm^{-1}, respectively [3.33]. The integrated intensities at 500 cm^{-1} and 520 cm^{-1} are related to small crystallites in the deposited films whereby the former corresponds to a distribution of the small crystallites and the last to crystalline silicon.

3.4 Transmission Electron Microscopy

3.4.1 Introduction

Transmission electron microscopy (TEM) was used to investigate the structure of the deposited films; cross-section specimen were prepared using the Tripod Polishing method to study the crystallographic characteristics, amorphous nature and elemental composition of the films. The Field Emission TECNAI F20 TEM was used in this investigation.

UNIVERSITY of the
WESTERN CAPE

3.4.2 Theory

A microscope makes use of optics in order to transform an object into an enlarged image. Basic principles of the transmission electron microscopes are based on those of the light microscopes. In light microscopy, glass lenses are used to magnify the fine details of specimen, while in electron microscopy magnets are employed to bend a beam of electrons. TEM makes use of electrons in probing the structure of the thin films by passing a beam through the thin material and projecting the transmitted beam on a fluorescent screen as a visual image. This conventional

approach of specimen imagery is similar to that applied in Light Microscopy (LM) with the difference that in LM, a source of light is used in probing specimens.

The principle of imagery in light microscopy involves the illumination by a beam of light focused by the condenser lens on a transparent specimen where the transmitted light experiences absorption and refraction through various dense regions in the specimen. An enlarged image of the specimen carried by the transmitted beam is then generated in the objective lens and then finally magnified by the projection lens [3.34].

In theory, by applying multiple lenses, it is possible to obtain as high magnification of an object as desired; however magnification of images with focused and clearly distinct features is highly dependent on the resolution of the microscope. Objects which are smaller than the wavelength of light (about 200 nm for light microscopes) are considered unresolved and thus cannot be finely distinguished in light microscopy. Since the human eye is able to resolve an object up to 0.2 mm in size, magnification of an image with objects smaller than the microscope's resolving power exhibit indistinct features in the projected images [3.35]. The resolution, also known as the resolving power, of a microscope is said to be the smallest separation at which two points can be seen as distinct entities.

UNIVERSITY of the
WESTERN CAPE

In a microscope, when light passes through a series of lenses or apertures, diffraction takes place causing causes the beam of light to be transformed into cone-like shapes detected as circles known as airy rings. The airy rings are characterized by the sizes of the centered spot which is inversely proportional to the diameter of the aperture the beam of light passes through; thus a small center spot represents a passage of light through a large aperture. This diffraction effect has a considerable influence on the resolution of a microscope in that very small spots are seen as airy discs and in order to resolve the effect a larger aperture must be used.

Lord Rayleigh proposed a solution to resolve objects in a microscope exhibiting these airy rings: if the maximum of intensity of the first ring coincides with the minimum of the second then the separation between the two objects can be established. The resolution in light microscopy can be described from the diffraction theory and is given by Abbe's equation as [3.36];

$$\delta = \frac{0.61\lambda}{\mu \sin \beta} \tag{3.41}$$

where λ is the wavelength of the radiation, μ is the refractive index of the viewing medium, and β is the semi-angle of collection of the magnifying lens described in Fig. 3.10. Eqn 3.42 above suggests that in order to achieve the best resolution of a microscope the value of δ has to be its smallest value, obtained if the following three conditions are satisfied;

a. λ is decreased, that is the use of short wavelength radiation
b. μ is increased, that is the use a medium with a large refractive index (optically dense material such as an oil immersion objective lens)
c. β is increased, that is the objective aperture is increased.

UNIVERSITY of the
WESTERN CAPE

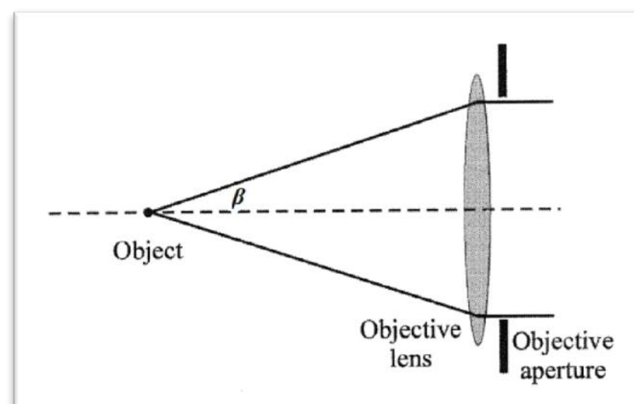

Figure 3.10. *The definition of the semi-angle, β, subtended by an aperture (in this case the objective aperture) [3.35].*

Abbe's equation describes the relationship between the resolution of a microscope and the wave nature of light.

In TEM, since magnetic lenses are used for controlling electrons, thus the refractive index μ has a negligible effect to the resolution. The semi-angle of collection β for the deflected electrons is generally a few degrees and thus for $sin\,\beta$ the small angles approximation applies. Eqn 3.42 can now be written as;

$$\delta = \frac{0.61\lambda}{\beta} \quad (3.42)$$

to describe the theoretical resolution of an electron microscope.

UNIVERSITY of the WESTERN CAPE

Another parameter in TEM is the depth of field and it is defined as the range of positions of an object that an observer can view an image with no loss of sharpness within the specimen [35]. The depth of field allows the end user to view a specimen over a range of positions without forfeiting its sharpness and can be described by a simple geometry where it can be expressed as h such that;

$$h = \frac{0.61\lambda}{\mu \sin\beta \tan\beta}. \quad (3.43)$$

Equation 3.43 shows that an increase in the depth of field will cause the resolution of the microscope to deteriorate. Thus for small electron deflections of the semi-angle, $\sin\beta = \tan\beta = \beta$ holds and thus equation 3.43 becomes

$$h = \frac{0.61\lambda}{\beta^2} \quad (3.44).$$

Therefore from Eqn. 3.43 and Eqn. 3.44, an increase in the semi-angle of collection causes the depth of field to increase rapidly with a better resolution.

Lens aberrations are common even in electromagnetic lenses although easier to correct compared to that from optical lenses. Two types of lens aberrations are to be considered in TEM; chromatic and achromatic aberrations. Chromatic aberration is a defect that occurs in a lens when electrons of different wavelengths are brought to focus on the optimal axis at different points whereas the best focus would be a disc of least confusion formed between the foci. This defect distorts the image of every point in the image thus causing a loss of quality and resolution of the image. Thus it is best to use an electron gun that produces an electron beam of monochromatic electrons. However electrons inevitably lose their energies due to their interaction with a specimen. The loss of electron energies is usually problematic for thick specimen leading to poor resolution. Thus the specimen prepared ought to be as thin as possible to avoid such problems.

UNIVERSITY of the
WESTERN CAPE

Achromatic (spherical) aberration is a defect in the lens caused by the difference in path lengths of different rays and electrons from the object point to the image point. This occurs when electrons from the optical axis are brought to focus closer to the lens and those near the axis are brought to focus further from the lens therefore forming a disc of least confusion as a focal plane. Thus to cancel out such aberration, small apertures are used in TEM [3.35, 3.36].

3.4.3 Operation of a TEM

The TEM instrument used in this investigation utilizes Field Emission Gun (FEG) as source of the electron beam. The electron sources are either made up of fine needle tips, usually made from tungsten wires that can be readily thinned to a radius of < 0.1 μm. By applying enough potential

on the tip, a high electric field can be formed and thus lowering the work function barrier sufficiently for electrons to escape from the surface of the tip. The work function can be defined as the natural barrier that prevents electrons from leaking out of a surface of a material [3.36]. A FEG consists of a two anode system where the first anode is used to extract electrons from the tip and the second anode for accelerating electrons to an appropriate voltage, the TECNAI F20 TEM is able to reach accelerating voltages of 200 kV. The beam is deflected between the two anodes which act as electrostatic lens and a crossover is formed; this is shown in Fig. 3.11.

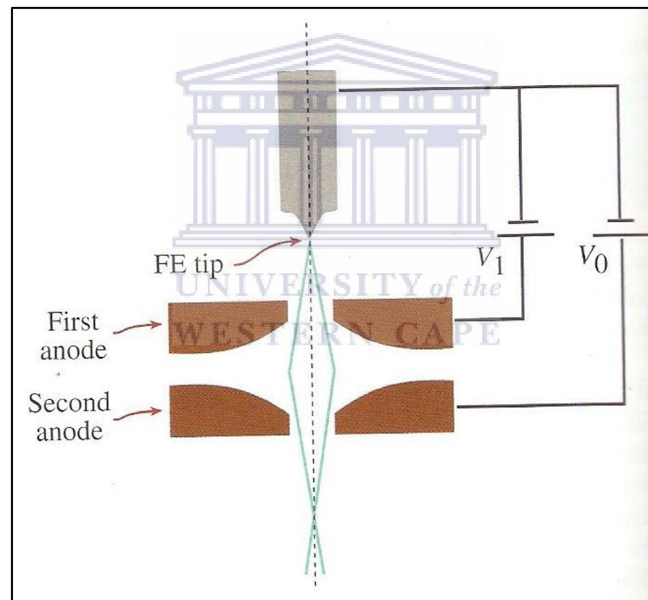

UNIVERSITY of the
WESTERN CAPE

Figure 3.11. *A schematic representation of a FEG showing electron paths from the field-emission source forming a crossover influenced by the two anodes acting as an electrostatic lens [3.36].*

The size and position of the resulting electron beam is said to be dependent on the electrostatic lens formed by the two anodes; thus an extra magnetic lens can be added to have an effective control over the beam.

The high energy electrons are then accelerated across a bias potential difference of high voltage (200 kV) towards the anode and then directed down the column of the microscope. The electron beam is then focused by a series of electromagnetic condenser lenses into the specimen. The optimization of the operation of the electron gun is dependent on three parameters which is the filament current, the Wenhelt cap and the accelerating voltage.

i. The filament current is set in such a way that the number of electrons emitted from the filament is at their maximum. A further increase in the filament's current results in no increase on the number of electrons emitted; this point is known as saturation of the filament. The filament current needs to be optimized since over saturation may reduce lifetime of the filament.

UNIVERSITY of the
WESTERN CAPE

ii. The Wenhelt cap consists of a grid situated near the filament and is connected to the voltage bias. The voltage across the Wenhelt cap is set slightly more negative compared to the filament's voltage to control the current released from the gun and also the size of the area on the filament from which it comes; implying that the voltage bias is used to control the brightness of the beam on the screen. This is useful in controlling contrast when specimens with thick regions are in view or to decrease the heating and damage that may be caused by the electron beam.

iii. The accelerating voltage is set based on the nature of the sample analyzed. An image of a specimen that possesses an area with thicker regions is seen having a lower contrast and therefore requires high energy electrons for viewing in the TEM. The value of the voltage

is usually not altered in a TEM as this will require the reset of other gun parameters and also the re-alignment of the microscope's column.

The establishment of the electron beam is then followed by a series of electromagnetic lenses that sets up an electromagnetic field symmetrically around the optical axis, thus focusing the beam to a spot on a specimen in view.

The electron gun produces a beam which passes through the anode and then is aligned onto the columns optical axis by the gun deflector coils. The first condenser lens then focuses the electron beam to a small spot, of which it's setting up defines the spot size obtainable in the TEM. The second condenser lens helps to control with ease the illuminated area and the convergence angle when projecting the beam on the specimen. The condenser aperture under the second condenser lens is used in controlling the amount of illumination needed with respect to the specimen's thickness. The objective lens focuses the beam on the specimen forming an intermediate image of a magnified size. The specimen holder sits within the objective lens when inserted in the microscope's column and the Selected Area Diffraction (SAD) aperture which is exerted at the back focal plane is used to allow certain groups of electrons for a diffraction pattern analysis over a selected desired area by reducing the diameter of the electron beam.

UNIVERSITY of the
WESTERN CAPE

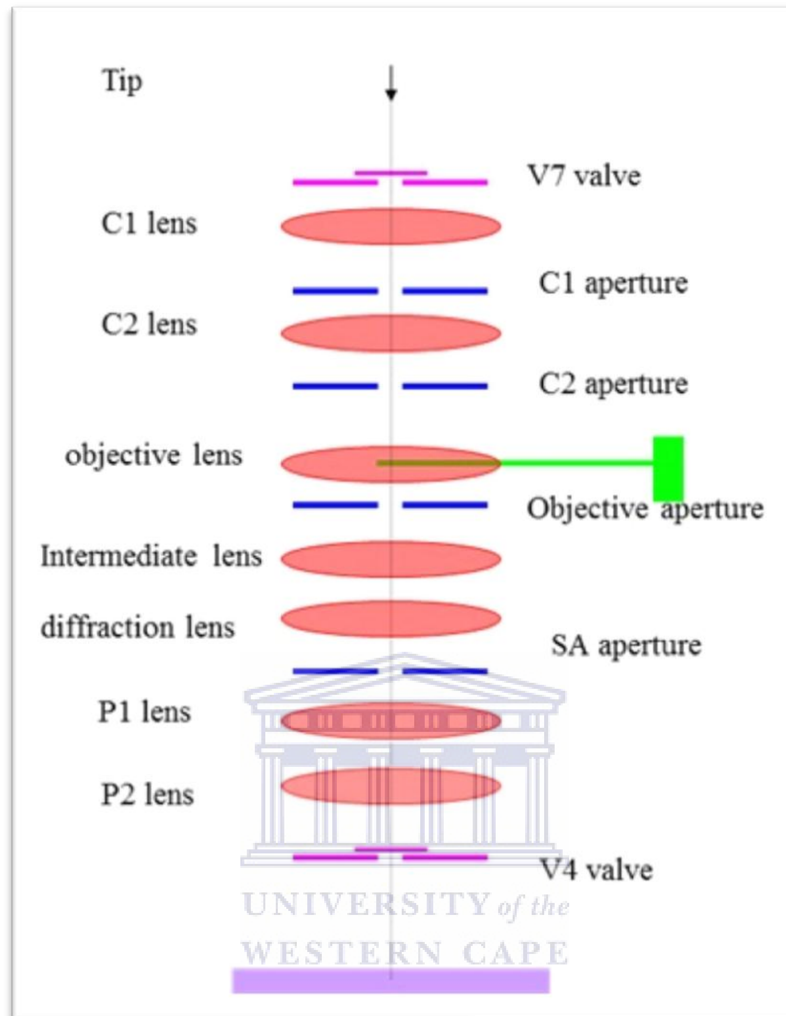

UNIVERSITY of the
WESTERN CAPE

Figure 3.12. *Ideal setup of a basic transmission electron microscope.*

The strength of the intermediate lens is set in such a way that the back focal plane of the objective lens is its object and the implication is to project an image of a diffraction pattern onto a fluorescent screen. The intermediate lens' strength can also be adjusted in which the image plane of the objective lens is its object, projecting a magnified image of the object onto the fluorescent screen. The projector lenses gives the final magnified upright image viewed on a fluorescent screen situated at the bottom of the microscope's column where a magnified image

can be seen with a naked eye, and a CCD camera below the fluorescent screen capture images that are viewed on a computer.

The structures of the specimens in this investigation are mainly amorphous and crystalline thus Dark-field images and Bright-field images are taken in order to account for the crystallinity in the samples since in dark-field imaging, crystalline regions appear as bright features and in bright-field imaging, crystalline regions appear as dark features [3.37]. Electron diffraction was also used to determine the lattice parameters and consequently the element or elements in crystalline structure.

3.4.5 Alternative techniques in the TEM

UNIVERSITY of the
WESTERN CAPE

Scanning Transmission Electron Microscopy (STEM) is a technique that is able to combine the analytical methods of the TEM and a SEM, and also provide information on elemental composition and electronic structure of samples, up to the scale of an atom [3.38]. The STEM technique involves a beam of electrons focused on a point by a set of condenser lenses and an objective lens, scanning across a selected area on the specimen by scan coils and collecting signals from the region, such as x-rays, transmitted, secondary or backscattered electrons. Thus the backscattered or secondary electrons are collected for imaging while the transmitted electrons are used for better spatial resolution making use of BF and DF imaging. The advantage a STEM carries is that by using multiple detectors, the different signals can be used for various analytical purposes at the same time. The High Angle Annular Dark Field (HAADF) detector in the STEM is usually situated around the transmitted beam and is used to collect transmitted electrons

scattered at high angles. The most common detector also available in STEM technique is an energy-dispersive x-ray (EDS) detector for elemental composition analysis.

3.4.6 Specimen Preparation

3.4.6.1 Tripod Polishing

Samples used in this were used in TEM were prepared using the Tripod Polishing technique. The tripod polishing method in this project was adapted from an instructional manual written by Daniel Richardson with aid from Dr. Richard Vanfleet from Brigham Young University and Prof. Basil Julies from the University of the Western Cape. Tripod polishing is a mechanical polishing technique where samples are reduced to thicknesses that are thin enough to be viewed in a TEM, usually around a few tens of nanometers to a micron. The samples to be prepared require being strong enough in order to handle such technique. Tripod Polishing can also be used as a pre-FIB or Focused Ion Beam thinning tool. The FIB instrument functions the same as an electron microscope for imaging, however a FIB utilize an ion beam. The ion beam is massive enough to remove material from the samples view in layers of atoms. Since this can be time consuming, tripod polishing can be used to remove material up to a certain thickness and then used FIB for final thinning of the sample.

UNIVERSITY of the
WESTERN CAPE

3.4.6.2 Procedure

The basic goal in Tripod polishing is to make samples that are electron transparent. Materials in tripod polishing are thinned into a wedge, where the thinnest part of the wedge and is viewed in a transmission electron microscope is the area towards the edge indicated in Fig. 3.13a.

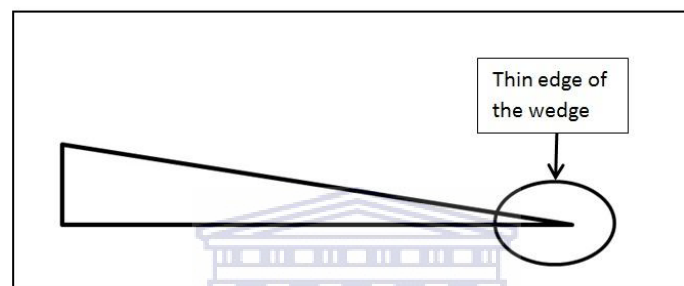

Figure 3.13a. *Example of a sample with a wedge shape after preparation from tripod polishing.*

UNIVERSITY of the
WESTERN CAPE

In preparation for tripod polishing, a sample was first cut into two 12.5 mm x 2.5 mm pieces which were then sandwiched using an epoxy, with the two films from each piece facing each other. A diamond saw was then used to cut the sample into 2.5 mm x 2.5 mm block shaped sizes, as shown in figure 3b. The sample was then placed on a melted wax on the glass rod attached to the L-bracket as shown in Fig. 3.13c, ready for polishing.

3.4.6.3 Polishing the backside of the sample

In Tripod polishing, the sample was polished on the backside using lapping films consisting of a thin layer embedded with diamond pieces of sizes 30, 15, 6, 3, 1 and 0.5 µm in sequence from the roughest grit to the finest grit to produce a fine polished sample side. After the last lapping film, colloidal silica was then applied on a felt pad for final smoothing on the surface of the sample.

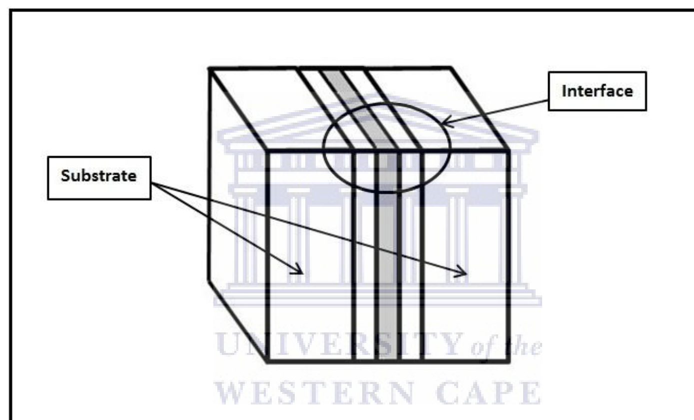

UNIVERSITY of the
WESTERN CAPE

Figure 3.13b. *Sample prepared by diamond saw cutter showing the interface with two deposited films on silicon substrates facing each other separated by a thin layer of epoxy.*

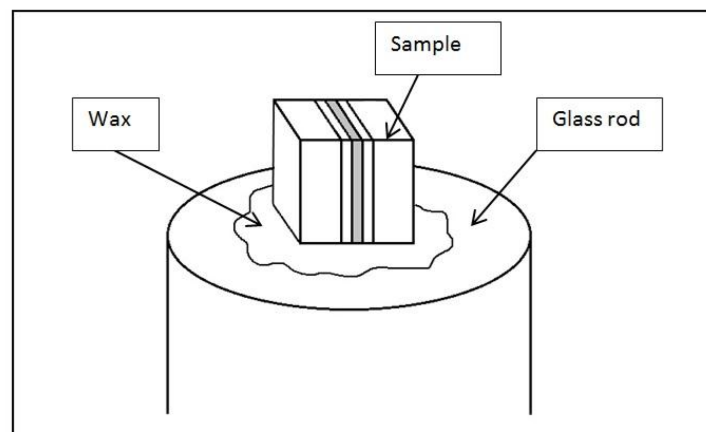

Figure 3.13c. *Sample attached on the glass rod located on the L-bracket by a thin layer of wax.*

3.4.6.4 Polishing the wedge side of the sample

After polishing the backside, the sample was then turned over and polished on the wedge side. This procedure is the same as that of the backside; however the tripod was adjusted in such a way that after the final polish the sample was presented as a wedge shaped specimen as shown in Fig. 3.13d.

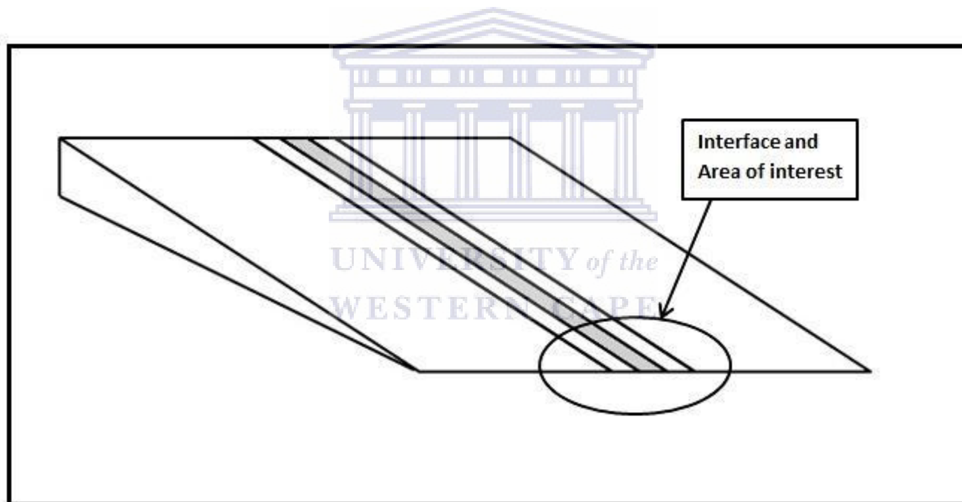

Figure 3.13d. *Wedge shaped specimen with its edge as the area of interest.*

The tripod polished sample was then mounted on a copper grid attached with M-bond to make sure it does not fall over in the microscope's column during analysis.

Arnold Bik, W. a. (1993). Elastic Recoil Detection. *Reports on Progress in Physics*, 859-902.

Ashby, M. F., Ferreira, P. J., & Schodek, D. L. (2009). *Nanomaterials, Nanotechnologies and Design: An Introduction for Engineers and Architects.* Oxford: Elsevier Ltd.

Feldman, L. a. (1986). *Fundamentals Of Surface And Thin Film Analysis.* Amsterdam: Elsevier Science Publishers B.V.

Fox, M. (2001). *Optical Properties of Solids.* Oxford: OUP Oxford.

Giorgis, F., Giuliani, F., Pirri, C., Rigato, V., Tresso, E., & Zandolin, S. (1998). Structural Information On a-SiC:H From Infrared and Raman Spectroscopy. In T. Searle, *Properties of Amorphous Silicon and Alloys Data Book* (p. 74). UK: INSPEC.

Goodhew, P. H. (2001). *Electron Microscopy and Analysis.* London: Taylor & Francis.

Hua, Z., Liaob, X., Diaob, H., & Kongb, G. (2004). Amorphous Silicon Carbide Films Prepared by H2 Diluted Silane–Methane Plasma. *264*(1), 7 - 12.

Janz, S. (2007). *Amorphous Silicon Carbide for Photovoltaic Applications.* Freiburg: Verlag Dr. Hut.

Kanekoa, T., Nemotoa, D., Horiguchia, A., & Miyakawa, N. (2005). FTIR Analysis of a-SiC:H Films Grown By Plasma Enhanced CVD. *Journal of Crystal Growth 275*, 1097–1101.

Kuenle, M., Janz, S., Eibl, O., Berthold, C., Presser, V., & Nickel, K. (2009). Themal Annealing of SiC Thin Films With Varying Stoichiometry. *159 - 160*(1), 355 - 360.

Langford, A., Fleet, M., Nelson, B., Langford, W., & Maley, N. (1992). Infrared Absorption Strength And Hydrogen Content of Hydrogenated Amorphous Silicon. *Physical Review B*, 13367-13377.

Larkin, P. (2011). *Infrared and Raman Spectroscopy: Principles and Spectral Interpretation* . Elsevier.

Lucovsky, G. (1979). Chemical Effects on the Frequencies of Si-H Vibrations in Amorphous Solids. *29*(8), 571 - 576.

Mahan, A. H., Von Roedern, B., Williamson, D. L., & Madan, A. (1985). Evidence for Graphitic-Type Bonding in Glow Discharge Hydrogenated Amorphous Silicon Carbon Alloys. *57*(1), 2717.

Mahan, A., Raboisson, P., & Tsu, R. (1987). Influence of microstructure on the photoconductivity of glow discharge deposited amorphous SiC:H and amorphous SiGe:H alloys. *Applied Physics Letters 50*, 335.

Pascual, E., Andlijar, J., Fernhndez, J., & Bertran, E. (1995). Optical and Structural Characterization of Hydrogenated Amorphous Silicon Carbide Thin Films Prepared by R.F. Plasma Chemical Vapour Deposition. *4*(1), 1205 - 1209.

Pennycook, S. J., Lupini, A. R., Varela, M., Borisevich, A., Peng, Y., Oxley, M. P., . . . Chisholm, M. F. (2007). Scanning Transmission Electron Microscopy for Nanostructure Characterization. In W. Zhou, & Z. Lin Wang, *Scanning Microscopy for Nanotechnology* (pp. 152-191). New York: Springer New York.

UNIVERSITY of the
WESTERN CAPE

Postek, M. H. (2001). *Scanning Electron Microscope: A Student's Handbook.* Vermont: Ladd Research Industries.

Rankin, D. W., Mitzel, N., & Morrison, C. (2013). *Structural Methods in Molecular Inorganic Chemistry.* John Wiley & Sons.

Razykov, T., Ferekides, C., Morel, D., Stefanakos, E., Ullal, H., & Upadhyaya, H. (2011). Solar Photovoltaic Electricity: Current Status and Future Prospects. *Solar Energy 85*, 1580–1608.

Shah, A. (2010). *Thin Film Silicon Solar Cells.* New York: Taylor & Francis.

Sherman Hsu, C.-P. (1997). Infrared Spectroscopy. In F. Settle, *Handbook of Instrumental Techniques for Analytical Chemistry* (pp. 247-283). New Jersey: Prentice Hall PTR (ECS Professional).

Sherman Hsu, C.-P. (1997). Infrared Spectroscopy. In F. Settle, *Handbook of Instrumental Techniques for Analytical Chemistry* (Vol. First Edition). New Jersey: Prentice Hall PTR (ECS Professional).

Swain, B. (2006). Influence of Process Pressure on HW-CVD Deposited a-SiC:H Films. *201*(1132 - 1137).

Tabata, A., Komura, Y., Narita, T., & Kondo, A. (2009). Growth of Silicon Carbide Thin Films by Hot-Wire Chemical Vapor Deposition From SiH4/CH4/H2. *517*(1), 3516 - 3519.

Tessler, L., & Solomon, I. (1995). Photoluminescence of tetrahedrally coordinated a-Si1-xCx:H. *Physical Review B 52*, 10962–10971.

Wieder, H., Cardona, M., & Guarnieri, C. R. (1979). Vibrational Spectrum of Hydrogenated Amorphous Si-C Films. *92*(1), 99 - 112.

William, D. C. (2009). *Transmission Electron Microscopy Part 1: Basics.* New York: Springer.

Yu, W., Lu, W., Han, L., & Fu, G. (2004). Structural and Optical Properties of Hydrogenated Amorphous Silicon Carbide Films by Helicon Wave Plasma-Enhanced Chemical Vapour Deposition. *37*(1), 3304 - 3308.

Zahorowskit, W., Wiecht, G., & Mell, H. W. (1989). The Valence Band Structure of a-Si1-xCx:H Studied by X-ray Emission Spectroscopy. *1*(9571).

UNIVERSITY of the
WESTERN CAPE

3.5 Atomic Force Microscopy

3.5.1 Introduction

Atomic Force Microscopy (AFM) is an imaging technique used for surface morphology characterization. Atomic force microscopy can be applied in the quantification of the surface morphology and root mean square (RMS) surface roughness of the specimen surface at the nanometer range scale.

3.5.2 Theoretical Background

In AFM, a sample is scanned by placing a very sharp needle tip on a cantilever a few angstroms (Å) from the surface of the specimen and the atomic force between them is measured. Unlike the Scanning Tunneling Microscope which depends on electrically conducting surfaces for imaging, AFM can also be used to scan non-conducting surfaces down to the atomic scale. A mechanical lever, the cantilever, holds a fast force-sensing tip which interacts with the specimen surface. A force between them causes the cantilever to deflect as it is scanned over the sample. The deflection of the cantilever is monitored by a laser beam incident on the top of the lever and reflected directly onto a photodetector.

UNIVERSITY of the
WESTERN CAPE

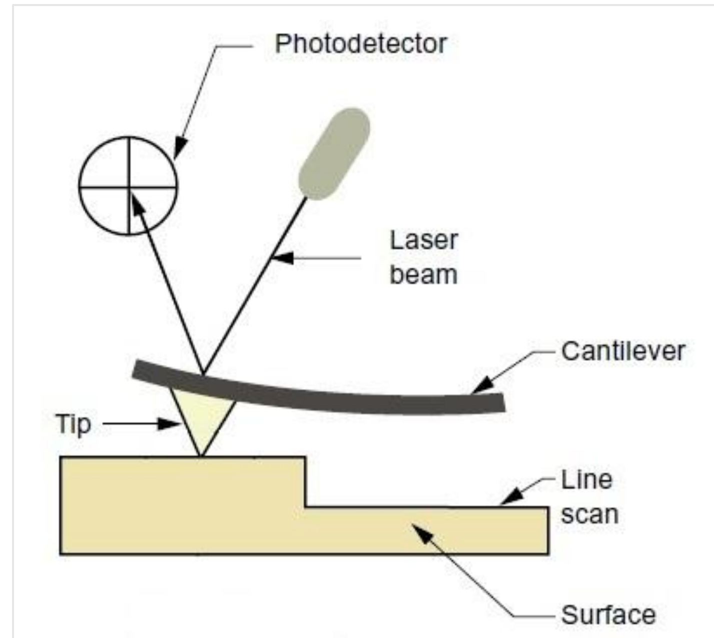

Figure 3.14. *Schematic representation of the scanning tip in AFM subtended on a cantilever. the photodector records the vertical position ot the cantilever using a laser beam as shown [3.39].*

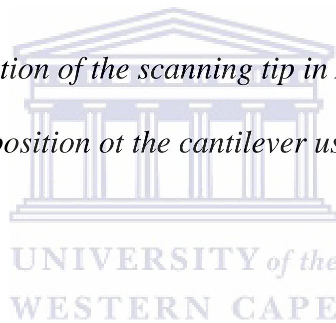
UNIVERSITY of the
WESTERN CAPE

As the cantilever deflects, the motions of the lever are detected and recorded while scanning across the specimen. There are two modes an AFM can use to probe the surface morphology; contact mode and tapping mode. In the tapping mode, the cantilever is caused to vibrate at a constant frequency while tapping the surface of the specimen; this allows the lever not to drag across the specimen therefore reduces the chances of damaging the specimen. In contact mode, a constant force is applied by the cantilever on the sample, and the tip is scanned across the sample for measurements; on very smooth surfaces the cantilever can cause damage on the sample. The importance of the relation between the range of forces the tip is able to apply and the elastic modulus of the material is vital.

In this investigation, a high resolution AFM imaging system equipped with a DI Nanoscope V SPM control station, a Dimension V Scan head with a hybrid XYZ closed loop scanner, a motorized stage with a sample chuck size of 150 mm in diameter, and an optical microscope which provides real-time colour video display at a 1.5 μm resolution with a maximum field of view of 675 μm, was used. Measurements of the specimen were taken in contact mode. An image of the Atomic Force Microscope used in this thesis is shown in Fig. 3.15. The RMS surface roughness was evaluated using the software NanoScope.

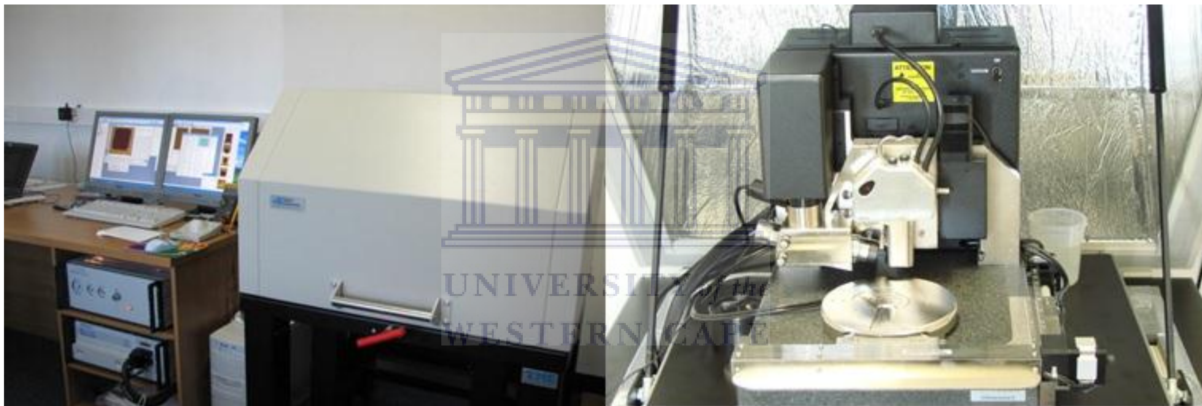
UNIVERSITY of the
WESTERN CAPE

Figure 3.15. *Images of a Veeco manufactured Nanoman AFM showing an acoustic enclosure (left) and a Dimension V close loop scanner (right).*

3.5.3 Surface Morphology and Roughness Measurements

AFM is capable of acquiring three dimensional (3D) images of the surface of the specimen: these images can be used in the investigation of the evolution of surface morphology of the samples deposited at varied deposition parameters and annealed samples. Roughness measurements

provide complementary information to the 3D images. The roughness statistics are measured from images taken at 5 µm x 5 µm and the estimated values given from NanoScope software are provided as the mean roughness, *Ra* and the root mean square roughness (RMS), also referred to Rq [3.40]. *Ra* measurements are the mean roughness value of the surface height from the image viewed, while the RMS roughness gives the standard deviation of the Z values in the given area and its least-square based algorithms are structured to calculate the roughness based on the best fit of all the point heights.

In this thesis, we will report the RMS roughness Rq given by

$$Rq = \sqrt{\frac{1}{N}\sum_{i=1}^{N}(z_i - \tilde{z})^2} \tag{3.45}$$

where N is the number of data points, and z_i and $\tilde{z}$ are the ith position and the average surface level respectively.

UNIVERSITY of the
WESTERN CAPE

3.6 XRD characterization

3.6.1 Introduction

The use of X-ray diffraction in probing nanomaterials is motivated by the fact that x-ray photons have wavelengths of the order less than a nanometer; making it possible to examine interatomic distances in crystals. XRD was used to study crystallinity in the films and to estimate the crystal size.

XRD characterization was performed on the samples deposited on glass substrates in order to study crystallinity in the deposited films.

3.6.2 Absorption of X-rays

The interaction of x-rays with atoms can cause electronic transitions within the atoms. When x-rays encounter any form of matter, a part of its intensity is transmitted and another part is absorbed. A fraction of intensity I of the x-ray beam is extinguished as it passes through any homogeneous substance of distance traversed x, and it can be written in the differential form as

$$-\frac{dI}{I} = \mu dx \tag{3.46}$$

UNIVERSITY of the
WESTERN CAPE

where μ the proportionality constant called the linear absorption coefficient which is dependent on the substance considered, its density, and the wavelength of the x-rays. A solution of the above equation is given by:

$$I_x = I_0 e^{-\mu x} \tag{3.47}$$

where I_0 is the intensity of incident x-ray beam and I_x is the intensity of transmitted beam after traversing through a thickness x. Since μ is dependent on the substance's density, then μ/ρ is a constant of the material and it is called mass absorption coefficient. Eqn. 3.47 can be rewritten as:

$$I_x = I_0 e^{-(\frac{\mu}{\rho})x} \tag{3.48}$$

The mass absorption coefficient for a compound with more than one chemical element is given as the weighted average of its constituent elements:

$$\frac{\mu}{\rho} = \omega_1 \left(\frac{\mu}{\rho}\right)_1 + \omega_2 \left(\frac{\mu}{\rho}\right)_2 + \cdots \qquad (3.49)$$

where $\omega_1, \omega_2,\ldots$ are the weight fractions of elements 1, 2, etc., in the substance and $\left(\frac{\mu}{\rho}\right)_1$, $\left(\frac{\mu}{\rho}\right)_2$, etc, their mass absorption coefficient.

3.6.3 Diffraction of X- rays

X-ray diffraction (XRD) was used to study crystallinity within the virgin deposited and annealed thin films. A monochromatic x-ray beam radiated on a sample can undergo diffraction if the beam is diffracted at an angle θ that satisfies the Bragg law. Diffraction in XRD is observed at selective angle θ_B, known as Bragg angles when the following equation is satisfied:

UNIVERSITY of the
WESTERN CAPE

$$\lambda = 2d \sin \theta_B \qquad (3.50)$$

where λ is the wavelength of the incident monochromatic radiation and d is the interplanar spacing.

The estimation of particle size in the films consisting of very small crystals is dependent on the width of the diffraction peak B, which is defined as:

$$B = \frac{1}{2}(2\theta_1 - 2\theta_2) \qquad (3.51)$$

where $2\theta_1$ and $2\theta_2$ are successive angular positions of the diffraction peak with zero intensity [3.41].

A relation to estimate the particle size t of small spherical crystals is given by the Scherrer formula [3.42]:

$$t = \frac{0.9\lambda}{B \cos \theta_B} \tag{3.52}$$

The crystal size is thus inversely dependent on the width of the diffraction peak.

Sharp peaks in XRD are characteristic of constructive interference originating from the reflection of X-ray radiation from regularly spaced atoms in a big crystal. A broad peak will be observed in case of small crystallites that do not preserve the long-range order.

References

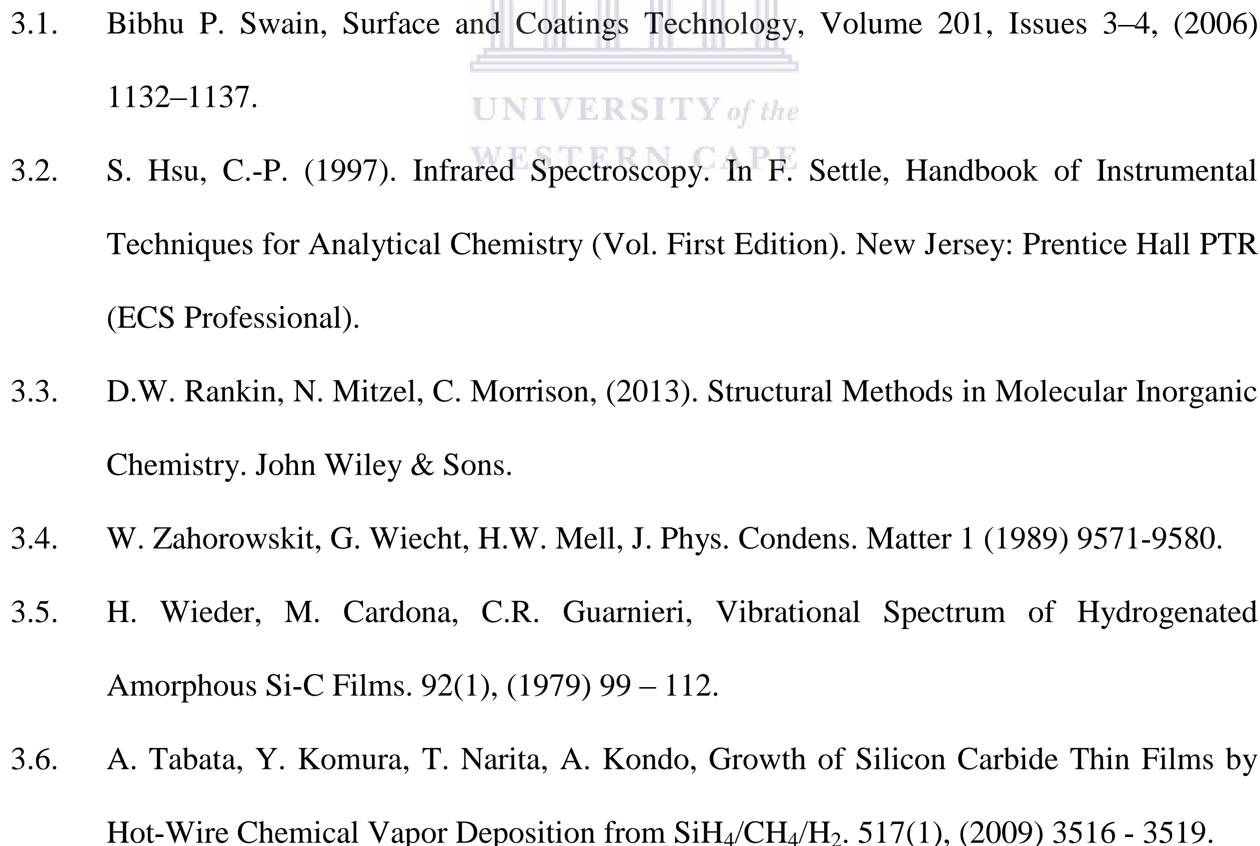
UNIVERSITY of the WESTERN CAPE

3.1. Bibhu P. Swain, Surface and Coatings Technology, Volume 201, Issues 3–4, (2006) 1132–1137.

3.2. S. Hsu, C.-P. (1997). Infrared Spectroscopy. In F. Settle, Handbook of Instrumental Techniques for Analytical Chemistry (Vol. First Edition). New Jersey: Prentice Hall PTR (ECS Professional).

3.3. D.W. Rankin, N. Mitzel, C. Morrison, (2013). Structural Methods in Molecular Inorganic Chemistry. John Wiley & Sons.

3.4. W. Zahorowskit, G. Wiecht, H.W. Mell, J. Phys. Condens. Matter 1 (1989) 9571-9580.

3.5. H. Wieder, M. Cardona, C.R. Guarnieri, Vibrational Spectrum of Hydrogenated Amorphous Si-C Films. 92(1), (1979) 99 – 112.

3.6. A. Tabata, Y. Komura, T. Narita, A. Kondo, Growth of Silicon Carbide Thin Films by Hot-Wire Chemical Vapor Deposition from $SiH_4/CH_4/H_2$. 517(1), (2009) 3516 - 3519.

3.7. M. Kuenle, S. Janz, O. Eibl, C. Berthold, V. Presser, K. Nickel, Thermal Annealing of SiC Thin Films with Varying Stoichiometry. 159 - 160(1), (2009) 55 – 360

3.8. S. Janz, (2007) Amorphous Silicon Carbide for Photovoltaic Applications. Freiburg: Verlag Dr. Hut.

3.9. E. Pascual, J. Andlijar, J. Fernhndez, E. Bertran, Optical and Structural Characterization of Hydrogenated Amorphous Silicon Carbide Thin Films Prepared by R.F. Plasma Chemical Vapour Deposition. 4(1), (1995) 1205 – 1209.

3.10. Z. Hua, X. Liaob, H. Diaob, G. Kongb, Amorphous Silicon Carbide Films Prepared by H2 Diluted Silane–Methane Plasma. 264(1), (2004) 7 – 12.

3.11. A.H. Mahan, B. Von Roedern, D.L. Williamson, A. Madan, Evidence for Graphitic-Type Bonding in Glow Discharge Hydrogenated Amorphous Silicon Carbon Alloys. 57(1), (1985) 2717

3.12. W. Yu, W. Lu, L. Han, G. Fu, Structural and Optical Properties of Hydrogenated Amorphous Silicon Carbide Films by Helicon Wave Plasma-Enhanced Chemical Vapour Deposition. 37(1), (2004) 3304 – 3308.

3.13. T. Kaneko, D. Nemoto, A. Horiguchi, N. Miyakawa, Journal of Crystal Growth 275 (2005) e1097–e1101.

3.14. T. Razykov, C. Ferekides, D. Morel, E. Stefanakos, H. Ullal, H. Upadhyaya, Solar Photovoltaic Electricity: Current Status and Future Prospects. Solar Energy 85, (2011) 1580–1608.

3.15. A. Langford, M. Fleet, B. Nelson, W. Langford, N. Maley, Infrared Absorption Strength and Hydrogen Content of Hydrogenated Amorphous Silicon. Physical Review B, (1992) 13367-13377.

UNIVERSITY of the
WESTERN CAPE

3.16. F. Giorgis, F. Giuliani, C. Pirri, V. Rigato, E. Tresso, S. Zandolin, Structural Information On a-SiC:H, (1998), Infrared and Raman Spectroscopy. In T. Searle, Properties of Amorphous Silicon and Alloys Data Book (p. 74). UK: INSPEC

3.17. P. Danesh, B. Pantchev, K. Antonova, E. Liaroskapis, B. Schmidt, D. Grambole, J. Baran, J. Phys. D: Appl. Phys., 37, (2004) 250.

3.18. T. Kanekoa, D. Nemotoa, A. Horiguchia, N. Miyakawa, FTIR Analysis of a-SiC:H Films Grown By Plasma Enhanced CVD. Journal of Crystal Growth 275, (2005) 1097–1101.

3.19. M.H. Brodsky, M. Cardona, J.J. Cuomo, Phys. Rev. B, 16 (1977) 3556-3571.

3.20. N. Maley, Phys. Rev. B, 46 (1992) 2078-2085.

3.21. W. Arnold Bik, Elastic Recoil Detection. Reports on Progress in Physics, (1993) 859-902

3.22. L. Feldman, (1986). Fundamentals of Surface and Thin Film Analysis. Amsterdam: Elsevier Science Publishers B.V.

3.23. D. Smeets, B.C. Johnson, J.C. McCallum, C.M. Comrie, Real-time in situ study of hydrogen diffusion on amorphous Si formed by ion implantation, Nucl. Instr. Meth. B (2011)

3.24. W. Beyer, H. Wagner, J. Appl. Phys. 53 (1982) 12.

3.25. J. Longa, Y. Yin, S. Sian, Z. Ren, J. Wang, P. Vayalakkara, S. Venkataraj, A.G. Aberle, Energy Procedia 15 (2012) 240 – 247.

3.26. H. Mukaida, H. Okumura, J. Lee, H. Daimon, E. Sakuma, S. Misawa, K. Endo, S. Yoshida, Raman scattering of SiC: Estimation of the internal stress in 3C-SiC on Si, Journal of Applied Physics 62, Issue 1, (1987) 254.

3.27. M. Fox, (2001). Optical Properties of Solids. Oxford: OUP Oxford

UNIVERSITY of the
WESTERN CAPE

3.28. F. Giorgis, F. Giuliani, C. F. Pirri, V. Rigato, E.Tresso, S. Zandolin "Structural information on a-SiC:H from Infrared and Raman spectroscopy", in IEE emis Data Reviews Series 19 "Properties of Amorphous Silicon and Alloys data book", ed. T. Searle (INSPEC, UK, 1998) 74

3.29. L. Tessler, I. Solomon, Photoluminescence of tetrahedrally coordinated a-$Si_{1-x}C_x$:H. Physical Review B 52, (1995) 10962–10971

3.30. A. Dasgupta, S. Klein, L. Houben, R. Carius, F. Finger, M. Luysberg, Thin Solid Films 516 (2008) 618–621.

3.31. P. Bibhu, B. Swain, Surface & Coatings Technology 201 (2006) 1132–1137.

3.32. S. Klein, L. Houben, R. Carius, F. Finger, W. Fischer, Journal of Non-Crystalline Solids 352 (2006) 1376–1379.

3.33. P. Brogueira, J. P. Conde, S. Arekat, V. Chu, J. Appl. Phys. 79, (1996) 8748.

3.34. M.H. Postek, (2001) Scanning Electron Microscope: A Student's Handbook. Vermont: Ladd Research Industries.

3.35. P.H. Goodhew, (2001) Electron Microscopy and Analysis. London: Taylor & Francis.

3.36. D.C. William, (2009) Transmission Electron Microscopy Part 1: Basics. New York: Springer.

3.37. A. Shah, (2010) Thin Film Silicon Solar Cells. New York: Taylor & Francis.

3.38. S.J. Pennycook, A.R. Lupini, M. Varela, A. Borisevich, Y. Peng, M.P. Oxley, M.F. Chisholm, (2007) Scanning Transmission Electron Microscopy for Nanostructure Characterization. In W. Zhou, & Z. Lin Wang, Scanning Microscopy for Nanotechnology (pp. 152-191). New York: Springer New York.

UNIVERSITY of the
WESTERN CAPE

3.39. M. F. Ashby, P.J. Ferreira, D.L. Schodek, (2009) Nanomaterials, Nanotechnologies and Design: An Introduction for Engineers and Architects. Oxford: Elsevier Ltd.

3.40. J. D. Miller, S. Veeramasuneni, J. Drelich, M. R. Yalamanchili, Polymer Engineering and Science, July 1996, Vol. 36, No. 14.

3.41. D. Cullity, 'Elements of X-ray diffraction', Addison-Wesley Publishing Company, Reading, Massachusetts (1978).

3.42. D. Phan, G. Chung, Applied Surface Science 257 (2011) 3285–3290.

3.43. E. Smith, G. Dent, 'Modern Raman Spectroscopy – A Practical Approach', John Wiley & Sons, Ltd, Manchester (2005).

3.44. S. Nakashima, H. Harima, Phys. Stat. Sol. A 162 (1997), pg. 39.

3.45. J. Wasyluk, T.S. Perova, S.A. Kukushkin, A.V. Osipov, N.A. Feoktistov, and S.A. Grudinkin, Materials Science Forum Vols. 645-648 (2010) 359-362.

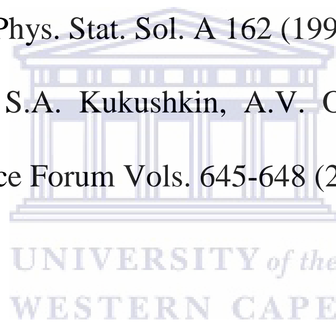

UNIVERSITY of the
WESTERN CAPE

Chapter 4. Structural Properties of the Deposited Materials

4.1 Deposition conditions

The samples presented in this study were deposited using a HWCVD system with deposition conditions summarized in Table 4.1. The filament to substrate distance, deposition time and deposition pressure were kept unchanged at 3.6 cm, 80 minutes and 15 Pa respectively, during the processing of all the samples.

The samples were deposited using hydrogen (H_2), methane (CH_4) and silane (SiH_4) gases. The H_2 and SiH_4 flow rates were maintained at 100 standard cubic centimeters per minute (sccm) and 2 sccm, respectively, while the CH_4 gas flow rate was varied between 0.5 – 6 sccm.

A high H_2 gas ratio was used for two reasons: the first reason is that hydrogen dilution in Si based films is known to passivate the dangling bonds and the number of those defective bonds is even expected to increase in non-stoichiometric amorphous SiC as found by several reporters; in this regard several reporters found that the use of high hydrogen gas flow rate promotes a deposition of quality device materials [4.1]; secondly, M. Mori *et al.* [4.2] showed that high hydrogen dilution, in HWCVD technique, produces films with high deposition rates compared to those deposited by PECVD.

Park *et al.* [4.3] showed that, due to an increase in hydrogen dilution, a shift in frequency of the *G* band in Raman spectroscopy to lower wavenumber was observed. This change results from the etching away of sp^2 bonded carbon as the ratio of sp^2/sp^3 carbon fluctuates.

UNIVERSITY of the WESTERN CAPE

The samples were deposited at low substrate temperature of 280°C; since crystalline silicon carbide films are known to be deposited under high temperatures of 1000°C and above, low temperature deposition is desirable in order to deposit films on cheap substrates such as glass and flexible materials [4.4, 4.5, 4.6, 4.7]. The samples were deposited at varied filament (Tungsten) temperatures of 1700°C and 2000°C in order to study the influence of the filament temperature on the structural properties of the films. The distance from filament to substrate, silane and hydrogen gas flow rate, deposition time and deposition pressure were kept unchanged at 3.6 cm, 2.0 sccm 100 sccm, 80 min and 15 Pa respectively, during the deposition of all the samples presented in Table 4.1.

Table 4.1 *Summary of deposition conditions and other useful characteristics of the samples.*

Sample name	CH_4 (sccm)	T_f (°C)	C [EDS] (at.%)	Thickness d_{TEM} (nm)	Thickness d_{ERDA} (nm)	Comment
S_1	6	1700	5.40		680	Samples used to study the effect of the filament temperature
S_6		2000	7.15	777	795	
S_2	0.5	2000	7.84	1152	1113	Samples used to study the effect of CH_4 flow rate
S_3	1				695	
S_4	2		7.64		882	
S_5	4		7.78	980	994	
S_6	6			777	795	

UNIVERSITY of the WESTERN CAPE

The reported thickness was obtained from measurements on the cross-sectioned specimen used in TEM (as measured from fig. 4.9) and also from ERDA simulations. The thickness reported from TEM were compared with the thickness deduced from SIMNRA simulations in ERD analysis. The agreement between the results from the two techques was very good. The accuracy of the thickness measured by the direct TEM technique is very good, but the preparation of TEM cross section specimen can be extremely expensive when the FIB is used and time consuming when mechanical thinning-polishing techniques; for samples not studied by TEM, the simulated thickness in ERD analysis is thus reported.

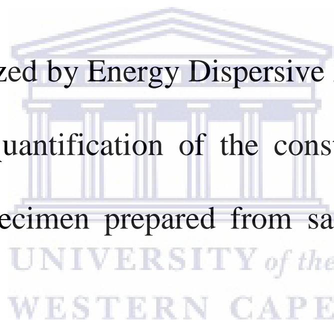
UNIVERSITY of the
WESTERN CAPE

The deposited films were all analyzed by Energy Dispersive X-ray Spectrometry (EDX) in TEM for elemental identification and quantification of the constituent elements. Fig. 4.1 shows a typical spectrum taken from a specimen prepared from sample $S_{6,}$ in this case an atomic C content of ~7% was obtained.

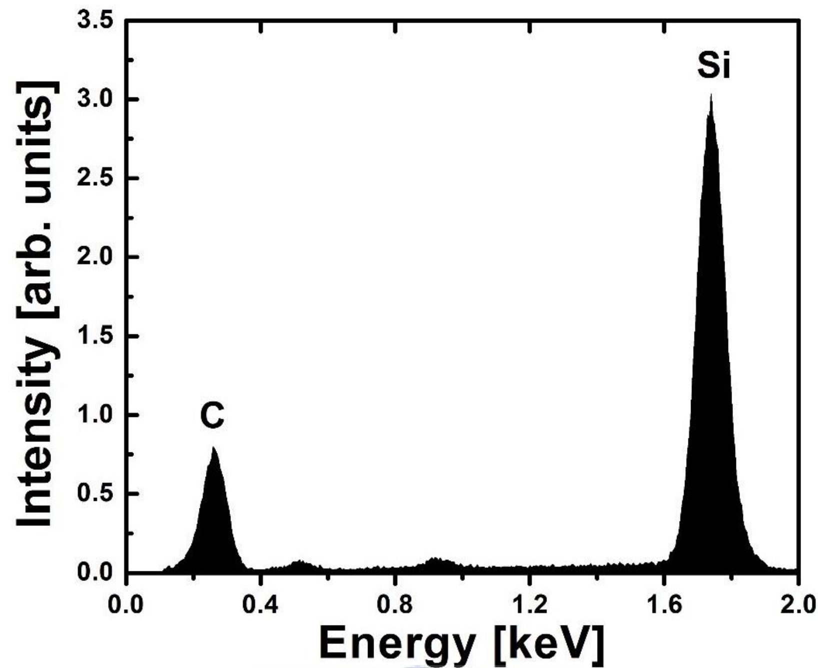

Figure 4.1 *EDS spectrum of the a-SiC:H film S_6.*

UNIVERSITY of the
WESTERN CAPE

All measured spectra confirmed the presence of silicon and carbon at energies of 1.74 keV and 0.277 keV. A particular observed feature was that high H diluted films yielded low atomic C content as low as 5 at% indicating a low incorporation of C at high hydrogen dilution.

4.2 The effect of the filament temperature

4.2.1 The effect of the filament temperature on deposition rate

The high deposition rate of silicon carbide thin films is required in order to produce solar cells at a reduced processing time in order to lower production costs, however without compromising the material quality. Thus the deposition rate is an important parameter in the deposition of a-SiC:H or μc-SiC:H films. HWCVD technique is recognized as a possible alternative to the established

Plasma Evaporated Chemical Vapor Deposition (PECVD) technique for large scale deposition of such films [4.8]. The use of high filament temperature during deposition of a-Si:H and a-SiC:H films lead to high deposition rates; this is attributed to the effectiveness of the filament kept at high temperatures to decompose the feed gases in respective radicals that form the thin films.

The deposition rate is defined as the ratio of the thickness of the deposited film d and the depostion time t_d as:

$$r_d = \frac{d}{t_d} \tag{4.1}$$

It is known that high hydrogen dilutions in the silane or methane gases lead to low deposition rates because of the etching effect of hydrogen; however it has been shown in this study that the combination of high H_2 dilutions and the setting of the filament to high temperatures can improve the deposition rate. This is supported by the data obtained in samples S_1 and S_6 (see deposition conditions in Table 4.1) where the deposition rates were found to be 8.50 and 9.71 nm/min respectively; this indicates that the SiH_4 and CH_4 gases are better decomposed in the radicals that participate to the film growth at high temperature of the filament as long as the saturation point has not been reached.

UNIVERSITY of the
WESTERN CAPE

We have used different characterization techniques to study the influence of the temperature of filament on the structural properties of the films. We compare the results obtained from samples deposited using a tungsten (W) filament maintained at two different temperatures of 1700°C and 2000°C.

4.2.2 AFM topography of films deposited at varied filament temperatures

AFM analysis was used to determine the surface roughness of the films deposited at varied filament temperatures; the results are presented in Fig 4.2.

Fig. 4.2 reveals that the as-deposited samples S_1 (fig. 4.2(a)) deposited with a filament's temperature of 1700°C is characterized by a smoother surface with a calculated roughness value of ~13 nm compared to S_6 (fig. 4.2(b)) deposited with a filament's temperature of 2000°C, which showed a roughness value of 31 nm. The roughening of the film deposited with a higher filament temperature can be attributed to the formation of crystallites; this is consistent with the results reported previously by Tabbal *et al.* [4.9]. A roughness of about 40 nm was reported by J Kraussl ich *et al.* [4.10] in SiC films consisting of crystalline columns of about 320 nm length as determined by TEM. In our AFM results, while the 3D images are conclusive on the roughness profiling, the 2D images give extra information on the crystallinity of the samples; the planar image on fig. 4.2(a) shows few dispersed grains contrasting with a higher density of grains observed on the 2D image in fig. 4.2(b). Thus a higher temperature of the filament promotes more crystallization of the films; this is consistent with the XRD and TEM findings.

UNIVERSITY of the
WESTERN CAPE

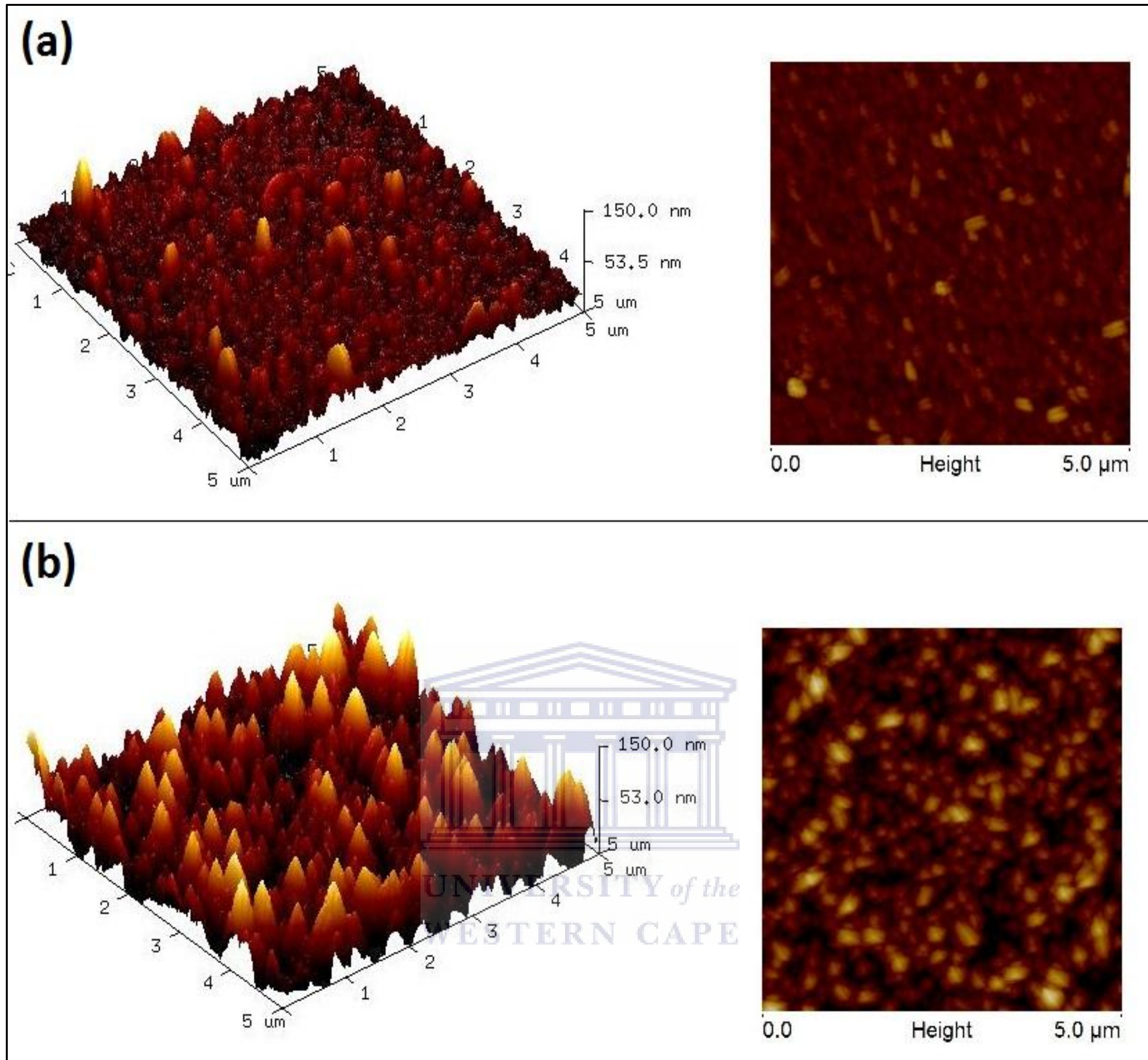

UNIVERSITY of the
WESTERN CAPE

Figure 4.2 *AFM 3D profile images of as-deposited a-SiC:H thin films and its corresponding 2D at varied filament temperatures (a)* S_1 *(b)*S_6.

4.2.3 Effect of filament temperature on microstructure by FTIR analysis

Variation in the microstructure of the films due to the effect of filament temperature was also investigated using FTIR analytical technique. We present in Fig. 4.3 the results obtained from samples S_1 and S_6 whose temperature of the filament was varied as in Table 4.1.

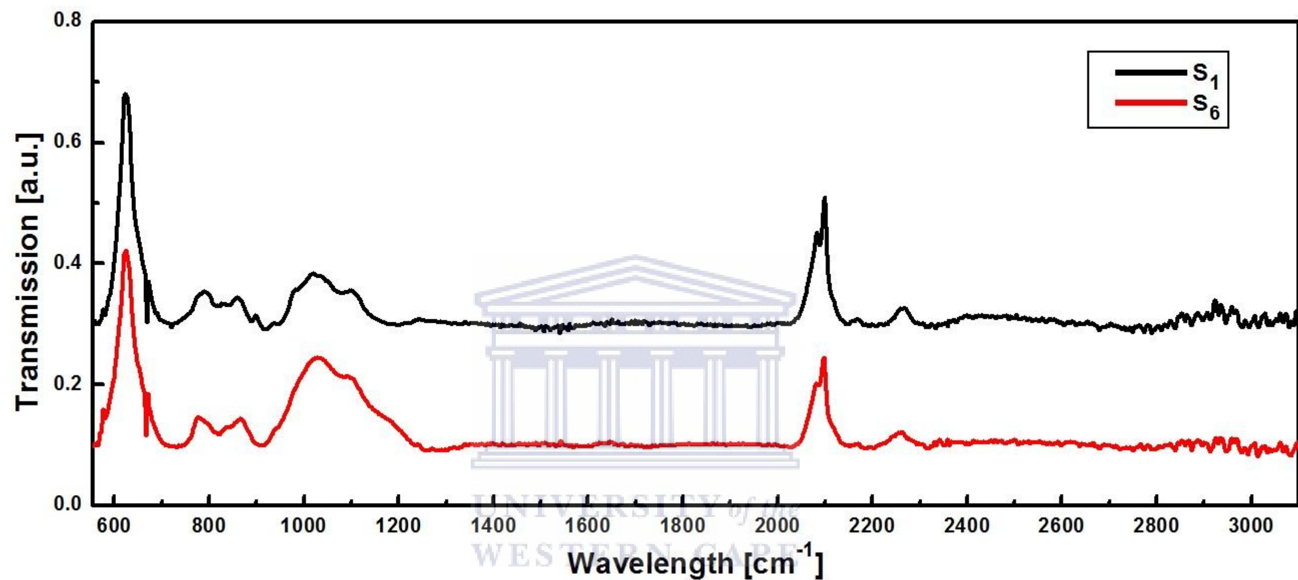

Figure 4.3 *FTIR spectra of as-deposited samples S_1 and S_6.*

A vibrational band at around 780 cm^{-1} in both samples, assigned to Si-CH_3 rocking/wagging modes was observed [4.11]. Less pronounced peaks have been observed at ~2070 cm^{-1} and ~2100 cm^{-1} and they have been attributed to Si-H and Si-H_2 stretching modes respectively [4.12]. Additional peaks around 1050 cm^{-1} and 1100 cm^{-1} were noted in both spectra; they are due to C-H_n rocking/wagging mode [4.2] and Si-O-Si stretching mode respectively [4.13].

The bands due to C-H stretching vibrations expected between 2800 cm^{-1} and 3000 cm^{-1} in sp^2 (towards lower wavenumber) and sp^3 (towards higher wavenumber) configurations respectively[4.14] were not detected in both samples. The features detected at around 800 cm^{-1} and 780 cm^{-1} attributed to Si-C bonds [4.15] and Si-CH_3 bonds [4.2] respectively, are observed to be less prominent compared to the Si-H rocking/wagging mode identified at wavenumber ~630 cm^{-1}. The C-H rocking/wagging modes in S_6 are also observed to be more prominent compared to S_1, suggesting a greater C content in films processed at higher temperature of the filament. The prominence of Si-H stretching modes over the C-H rocking/wagging modes in the spectra of both samples may suggest that the hydrogen is bound to Si in a much higher number; of course the bond strength constants of Si-H_n and C-H_n play a big role in the quantification of the actual H content contributing to these bands. A quantitative analysis on both samples revealed the measure of H concentration from the 640 cm^{-1} band to be 2.31 at.% and 1.74 at.% in S_1 and S_6 respectively.

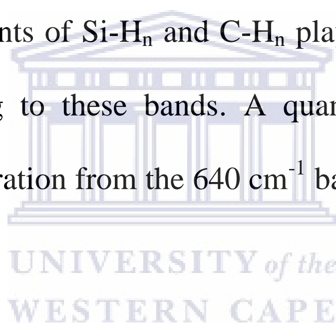

Higher hydrogen concentration in S_1 compared to S_6 in the 640 cm^{-1} band can be due to the lower temperature of the filament favouring a less effective splitting of SiH_4 molecules into the respective Si and H species. Higher density of heavy Si hydrides are expected in the films as there is not enough atomic H formed to provide the etching of the weak bonds neither the abstraction of hydrogen from heavy SiH_n radicals.

4.2.4 Effect of the filament temperature on the microstructure as studied by Raman scattering spectroscopy.

Raman spectroscopy can be used as a complementary technique to FTIR in thin films characterization. The as-deposited Raman spectra of films S_1 and S_6 are presented in Fig. 4.4 in the range 200–650 cm^{-1}.

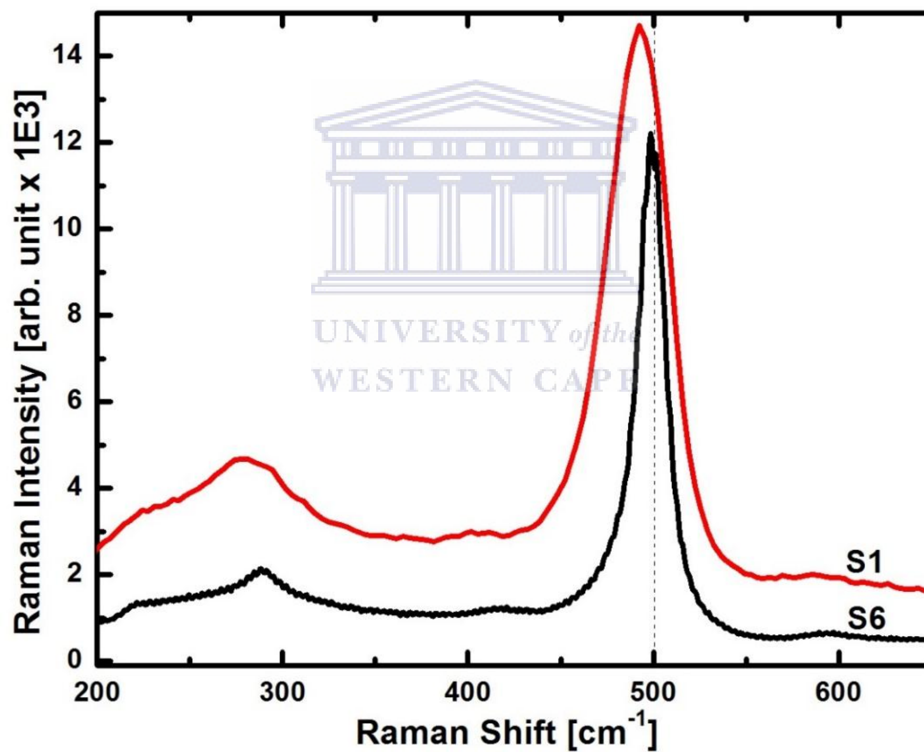

UNIVERSITY of the
WESTERN CAPE

Figure 4.4 *Raman spectra of a-SiC:H films S_1 and S_6 deposited by HWCVD at varied filament temperatures.*

Both spectra showed a small band centered at ~300 cm^{-1} which corresponds to Si–Si longitudinal optic (LO) mode and its intensity is predominant in S_1. A large Gaussian shaped peak was observed in S_1 with its center at ~496 cm^{-1}; it is usually reported in a-SiC:H films to originate from the contribution of the amorphous phase and small Si nanocrystals [4.21]. On the other hand a narrow Lorentzian - like peak centered at 500 cm^{-1} due to crystallization was observed in S_6.

High temperatures of the filament lead thus to a narrowing of the Si-Si TO peak and also to a shift toward higher wavenumber. The sample deposited at lower temperature of the filament showed a broad amorphous band that extends to much lower wavenumbers than 480 cm^{-1} known for a-Si. While the shifting of TO peak towards higher wavenumber is usually interpreted in terms of the crystallization in the Si network, a shift in the TO peak to lower wavenumber than 480 cm^{-1} was attributed, in our a-SiC:H films, to a local deformation caused by the carbon atoms as previously found by Kamble *et al.* [4.23].

UNIVERSITY of the
WESTERN CAPE

The Si–C band, which is expected to be within the range 750 – 980 cm^{-1}, is very weak as the Raman scattering efficiency in Si–C band is much smaller than that in C–C and Si–Si bands [4.18]. Fig. 4.5 presents Raman spectra of as-deposited films of S_1 and S_6 in the 700 – 1100 cm^{-1} range.

The figure shows peaks centred at wavenumbers ~870 cm^{-1} and ~900 cm^{-1} for S_1 and S_6 respectively; the first overtone above the fundamental Si (TO) mode is normally observed at ~960 cm^{-1}; the shift to lower wavenumbers in our films were attributed to the inclusion of C atoms in the a- or μc-Si:H matrix. Y. Huang et al. [4.16], in earlier studies observed in their nc-SiC films, Raman spectra at wavenumbers of about 796 and 965 cm^{-1} and assigned them to

transverse optical mode and the longitudinal optical mode of SiC [4.16]. The assignment of the second peak, in their study might be ambiguous as it overlaps with that of the 1st overtone above the 520 cm^{-1} Si TO, which is expected at ~960 cm^{-1}.

It is remarkable in our samples how the effect of C inclusion in the films was resolved by a much clearer downshift from the (1st overtone) TO Si peak center. Although only a small amount of SiC nanocrystals were observed in FTIR as indicated by a small contribution of the band 780 - 800 cm^{-1}, Raman scattering spectroscopy is found to be a powerful technique in the characterization of nc-SiC:H thin films by analyzing the downshift of the 1st overtone of 970 cm^{-1} peak. Its downshift towards ~900 cm^{-1} can be concluded to be due to the inclusion of C atoms in the films, resulting in the local short range strain detected by Raman spectroscopy.

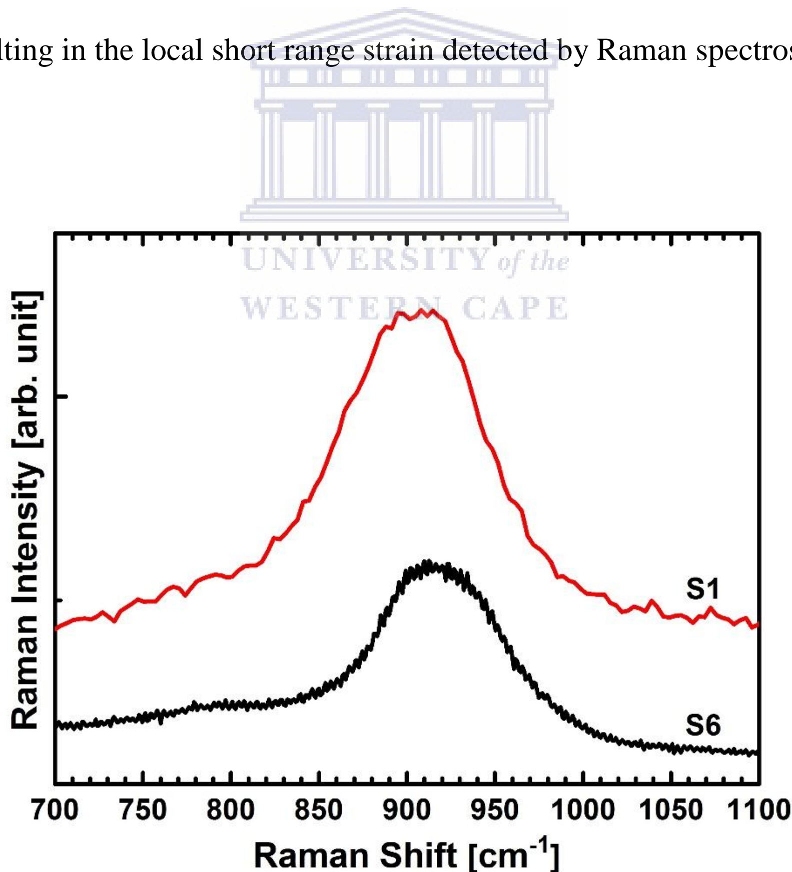

Figure 4.5 *Raman spectra of as-deposited samples S_1 and S_6 deposited at varied filament temperature.*

4.2.5 Effect of the filament temperature on the microstructure as studied by XRD analytical technique

Fig. 4.6 displays XRD patterns obtained from S_1 and S_6 films deposited on glass substrate. A broad peak between 20° and 28° at 2θ is characteristic of Si found in the glass substrate. The structure of the film showed prominent features of peaks centered around 28.50°, 47.40° and 56.30° known to crystalline Si(111), Si(220) and Si(311), this shows once again that the studied films are Si-dominated in the bulk. The absence of SiC signature in the XRD patterns of the films suggests that the Si-C related features embedded in the films observed from FTIR spectra are amorphous.

UNIVERSITY of the
WESTERN CAPE

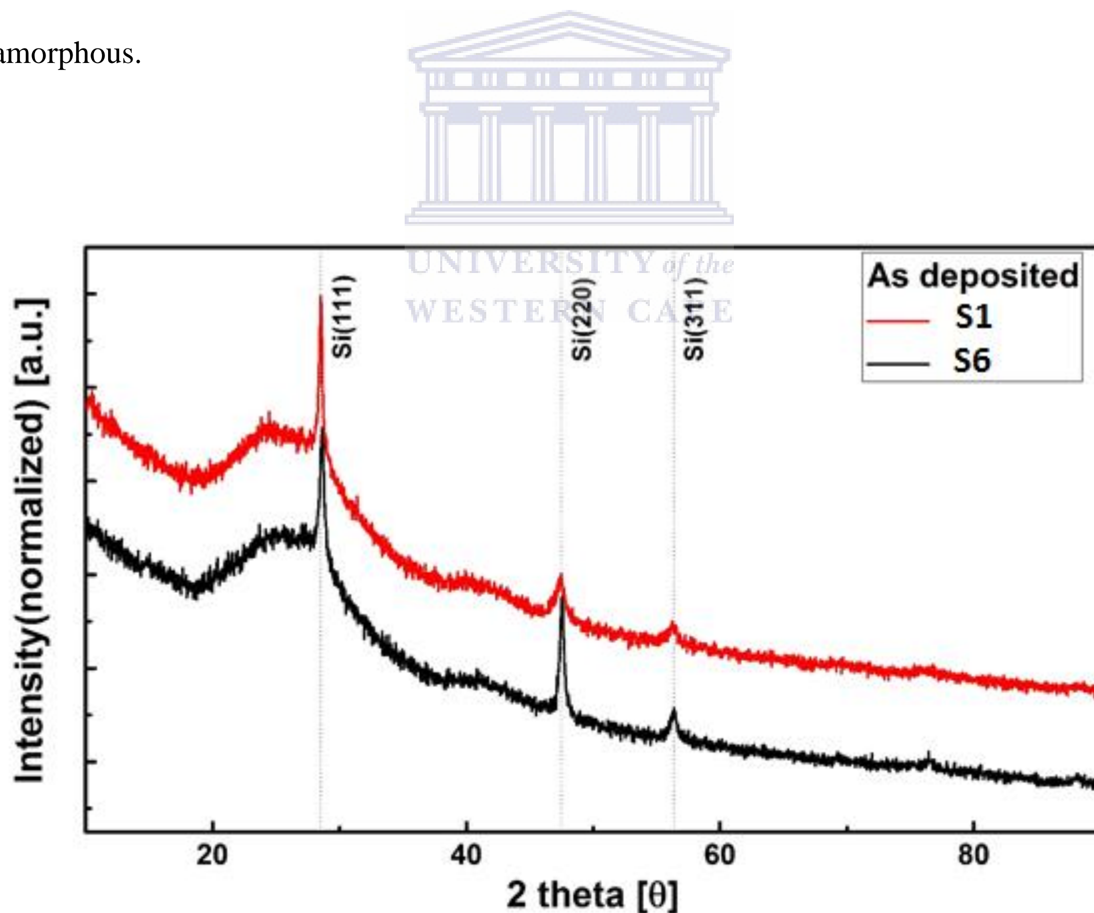

Figure 4.6 *XRD patterns of samples S_1 and S_6 deposited on glass substrate.*

The evaluation of the XRD peak Si(220) was used to determine the crystallite sizes in using the Scherrer equation mentioned in section 3.6.3. A crystalline size of 15 nm and 21 nm were estimated in S_1 and S_6 respectively. It is found that S_6 sample deposited at a higher temperature of the filament contained slightly larger crystal size.

4.2.6 Effect of the temperature of the filament on hydrogen incorporation in the films as studied by ERDA

Figure 4.7 presents ERD spectra of sample S_1 and S_6. The observed depth profile of H in the samples suggests a bulk hydrogenation with a small surface component contribution. While in a uniform a-Si:H containing equal H content , a rapidly decreasing yield with depth is expected; it is clear that the spectra obtained for a-SiC:H S_1 and S_6 samples suggest a different hydrogenation process in the films.

UNIVERSITY of the
WESTERN CAPE

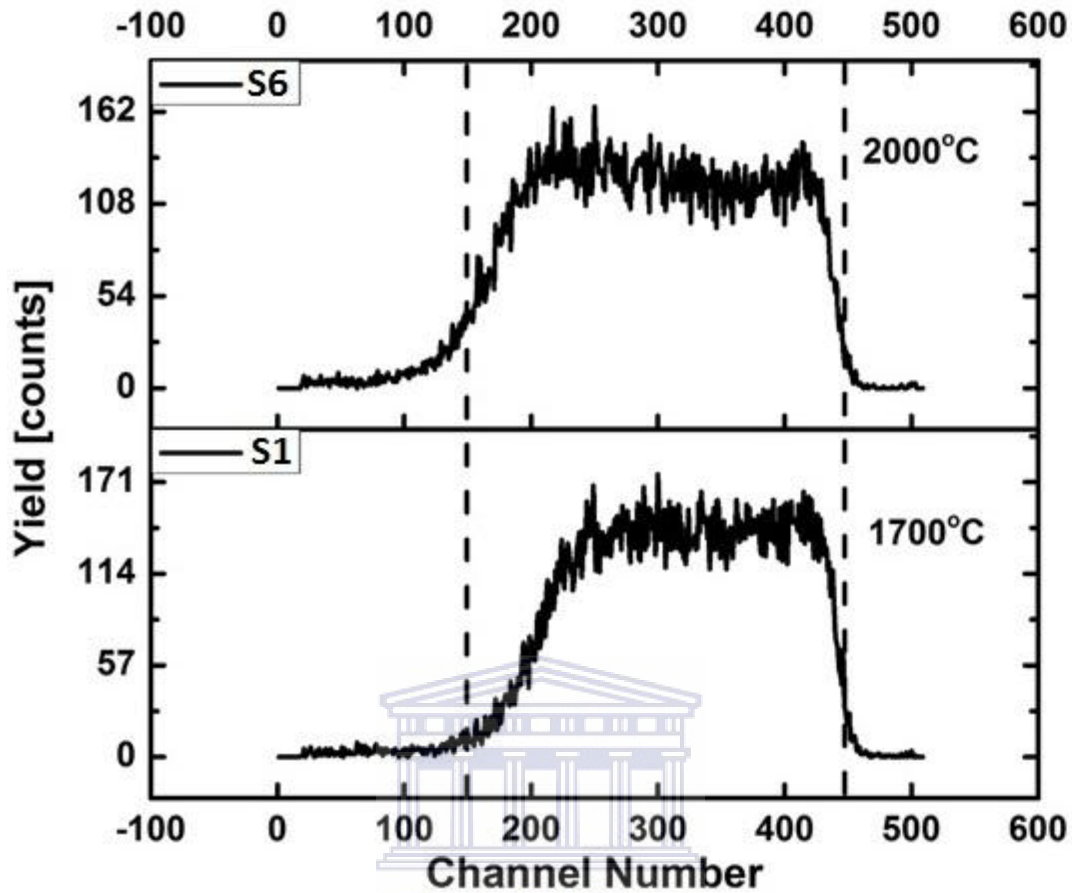

UNIVERSITY of the
WESTERN CAPE

Figure 4.7 *Hydrogen depth profile of the deposited a-SiC:H films S_1 and S_6 at varied filament temperature.*

The observed almost zero gradient in S_1 spectrum and a small negative gradient of the curve in S_6 point to an increasing hydrogenation with depth. Hydrogen content from the samples yielded H content values of 5.80 at.% and 5.56 at.% for S_1 and S_6, respectively; greater H-content in S_1 are calculated as expected. The observation of the spectra indicates more incorporation of H towards the interface. It should be noted that there is a preferential bonding in C-H compared to S-H forms due to the higher H – C binding energy [4.24]. Thus it can be suggested that a C rich microstructure is situated near the interface.

As mentioned in section 4.1, the thickness of S_6 measured from TEM cross section (thus direct true thickness) was comparable with the thickness obtained from the simulation of the hydrogen profile in ERD. It may thus be suggested that hydrogen was distributed throughout the entire deposited layer.

.

4.2.7 Influence of the temperature of the filament on the microstructure as investigated by TEM

TEM studies were done on a specimen prepared from S_1 in order to investigate the phase changes in the film's microstructure; Fig. 4.8 presents a planar view micrograph.

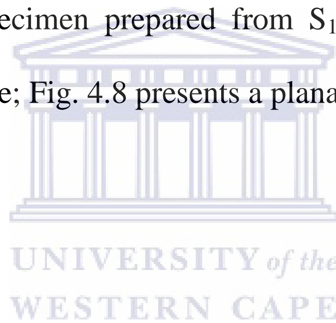
UNIVERSITY of the
WESTERN CAPE

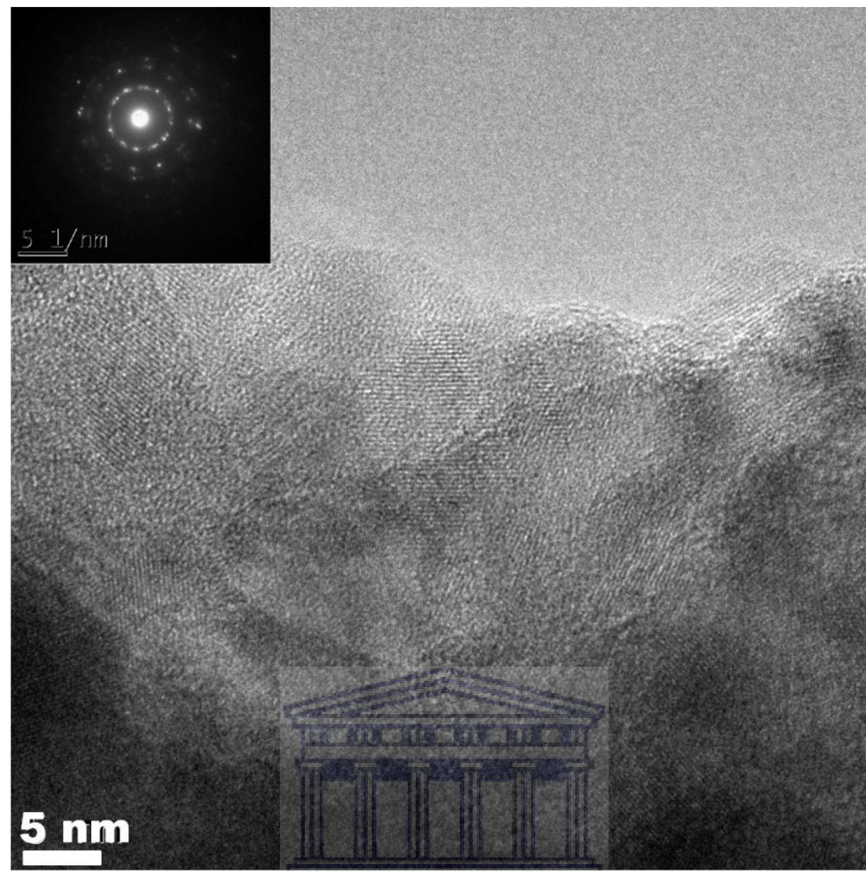

UNIVERSITY of the
WESTERN CAPE

Figure 4.8 *A planar view TEM image of S_1 prepared using the Tripod polishing technique; a diffraction pattern of a spot taken from the edge of the sample is shown in the insert.*

In Fig. 4.8, crystalline ordered regions can be observed at the edge of the sample. An average size of the crystal grains was estimated at ~14 nm, it is in agreement with the size measured from XRD with an error of 7%. A Selected Area Diffraction (SAD) pattern taken from a spot at the edge the sample is inserted; it shows that the film consists of a polycrystalline structure. The SAD pattern was used to determine the nature of the crystals. Measurements of the distance between the bright spots were used to determine the interplanar distances for lattice studies. Table 4.2 presents interplanar distances determined from the SAD patterns of sample S_1 and S_6

assuming a FCC system. The distance between the bright spots and the center of the diffraction pattern were measured in scale with the SAD pattern.

Table 4.2. *Determination of d spacing from the SAD patterns of S_1 and S_6.*

Sample	distance center –to ring position (mm)	g (1/nm)	*d* (nm)	*d* (Å) for Si Standard
S_1	27.8	3.31	0.30	~3.13 for 111
	43.8	5.21	0.19	~1.92 for 220
	51.0	6.07	0.16	~1.64 for 311
S_6	38.0	4.13	0.24	
	61.0	6.63	0.15	
	73.0	7.93	0.13	

UNIVERSITY of the
WESTERN CAPE

From Table 4.2, the calculated *d spacings* measured from the SAD pattern of S_1 are close to those of a silicon standard whose values are given in the last column of the table for the specified *(hkl)*; they are in agreement with XRD findings at 2θ diffracted peaks from silicon crystals [4.25]. Such similarity was also previously reported by Nonomura *et al.* [4.52] from the measurements of their microcrystalline and a-SiC:H films.

However, the determined *d spacings* in S_6 sample, where more C content was noted, shows values that deviate from those of a silicon standard, implying that there exist crystalline grains of different nature from those found in S_1. As the only major difference between the two samples

was the difference in C content due to different processing conditions, it seems that alloying of C atoms in a μc-Si:H films alters the *d* spacings within the Si crystal lattice if a given threshold in C-content is reached.

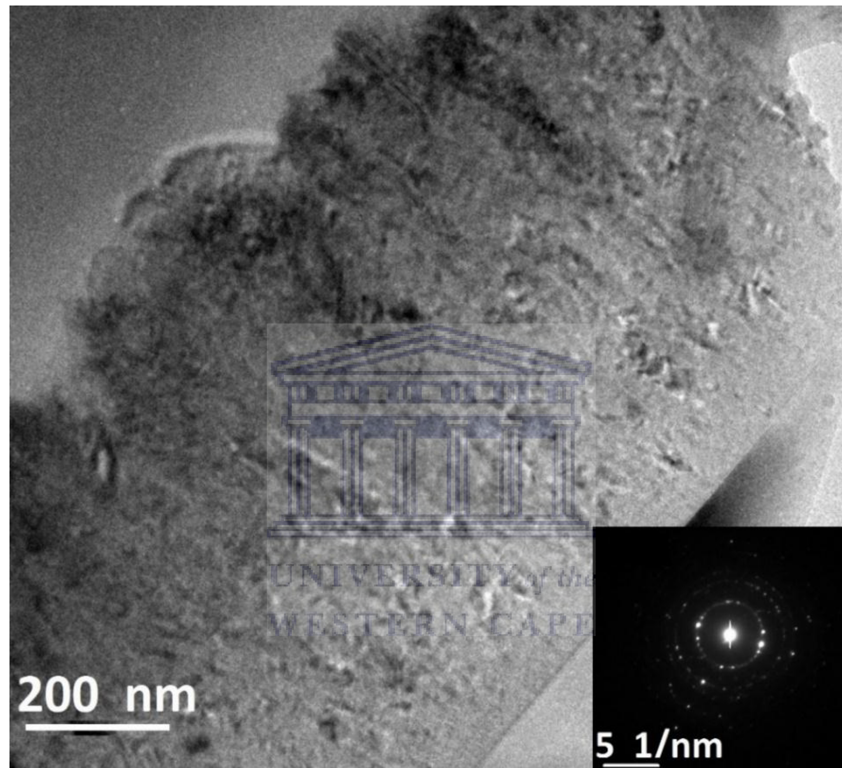

UNIVERSITY of the
WESTERN CAPE

Figure 4.9 *A bright filed TEM microgram of S_6 cross section prepared using the Tripod polishing technique with a diffraction pattern of a spot taken in the bulk of the deposited film (Inserted image).*

Fig. 4.9 presents a bright field TEM micrograph of sample S_6. A microcrystalline columnar growth similar to the one known for μc-Si:H can be observed towards the surface of the sample [4.26, 4.27]. The size of the crystalline columns was observed to increase in size as the film grew

thicker. The inserted SAD pattern taken in the bulk of the deposited film indicates that the film is polycrystalline. At the interface region between the substrate and the deposited film, an incubation amorphous layer ~ 40 nm the film was observed; it is usually interpreted as a buffer and nucleation layer due to the mismatch between the lattice parameters of the substrate and those of the growing film [4.53].

This finding suggests that the films consist of amorphous silicon carbide region embedded in μc-Si:H matrix in agreement with the obtained results by XRD technique. The departure of the *d*-data in the S_6 SAD patterns from the Si standard, suggests a distortion of the Si lattice due to the inclusion of more C atoms in the film.

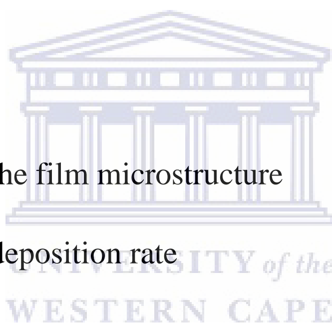
UNIVERSITY of the
WESTERN CAPE

4.3 Effect of CH_4 flow rate on the film microstructure

4.3.1 Effect of CH_4 flow rate on deposition rate

Figure 4.10 gives a plot of the deposition rate against the methane flow rate for the samples whose deposition conditions are given in Table 4.1; the filament temperature was maintained at 2000°C in the processing of all the films compared.

To study the effect of CH_4 flow on the deposition rate, we have maintained T_f at the optimized temperature of 2000°C and varied the CH_4 flow rate between 1 sccm and 6 sccm. The figure shows that the deposition rate is consistently increasing with the increase of CH_4 flow rate to a point beyond which it decreases. This should be understood in the context that SiH_n radicals are the ones that influence more the increase in deposition rate; once the gas pressure of CH_4

becomes excessive, the SiH_4 decomposition into growing radicals is not anymore efficient. Also it can be postulated that the increased rate of secondary reactions slows down the growth rate.

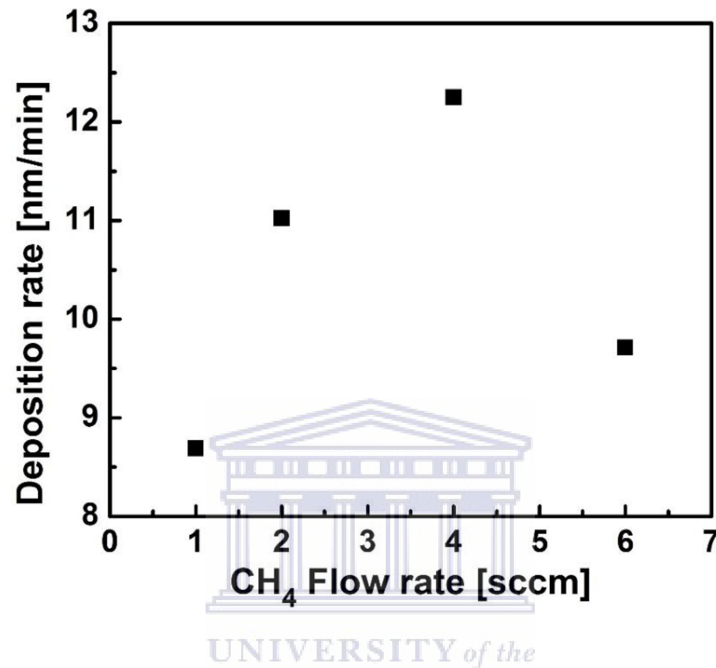

UNIVERSITY of the
WESTERN CAPE

Figure 4.10 *Deposition rate of a-SiC:H films as a function of CH_4 gas flow rate.*

4.3.2 Effect of CH_4 flow rate on the films' microstructure by TEM

Transmission electron microscopy (TEM) studies have been carried out on samples S_2 and S_6 deposited with different CH_4 flow rates in order to investigate the microstructural details of the samples. The specimen were prepared from samples deposited on c-Si (100) substrates. Fig. 4.11 presents a bright field TEM image of S_2 and S_6 deposited at different CH_4 gas flow rate. The deposited film shows dark features that suggest that the film is microcrystalline; they grow as columnar, a feature which is often reported in μc-Si:H films. It is observed that the columnar

crystalline growth starts beyond about 40 nm thickness in fig. 4.11(a), which suggests that there is an amorphous buffer layer near the interface.

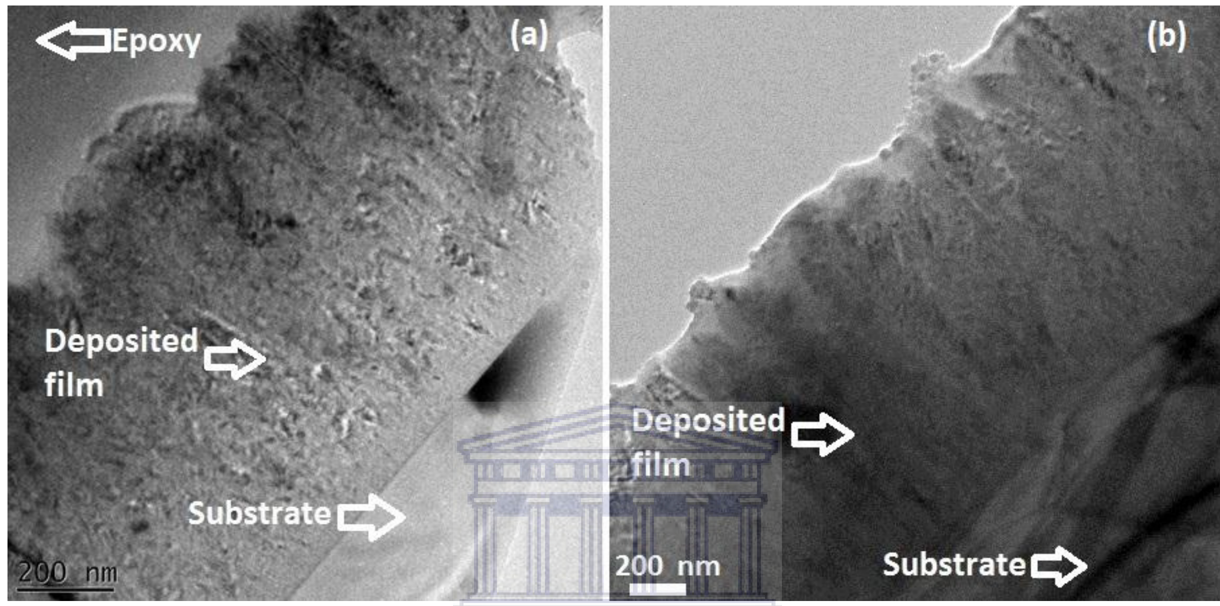

UNIVERSITY of the WESTERN CAPE

Figure 4.11 *Cross-sectional micrograph of the samples (a) S_6 and (b) S_2 deposited at CH_4 flow rate of 6 and 0.5 sccm respectively.*

These crystalline features appear more darker and wide toward the surface of the film. This means that the film becomes more crystalline as it grows thicker and the crystallites become bigger in size.

In fig. 4.11(b), the growth of the crystalline features are seen to start from the interface without any noticeable buffer layer as in S_6. The suppression of the incubation layer can be achieved by increasing hydrogen dilution during deposition of the film [4.57]. However, in sample S_6, CH_4 gas flow rate was increased during deposition which increased the CH_4 partial pressure in the chamber. As a result, the increased radicals originating from methane in addition to those coming

from the splitting of silane, subdue to the etching effect of atomic H on the growing surface; this explains the growth of an amorphous buffer layer in S_6. The incubation buffer layer is suppressed in S_2 grown in a CH_4 starving environment because the amount of atomic H is optimized on the growing surface.

The incubation layer in S_6 is interestingly accompanied with the high hydrogen concentration that was observed in its ERDA spectrum in Fig. 4.7 near the interface. EDX studies done on the sample showed that more C resided in the deeper part of the film near the substrate, thus more disordered network in the interfacial layer. The observed reservoir of H near the interfacial region is thus linked to the presence of C there, either in the form of CH_n and or as molecular hydrogen trapped in the voids introduced by C alloying.

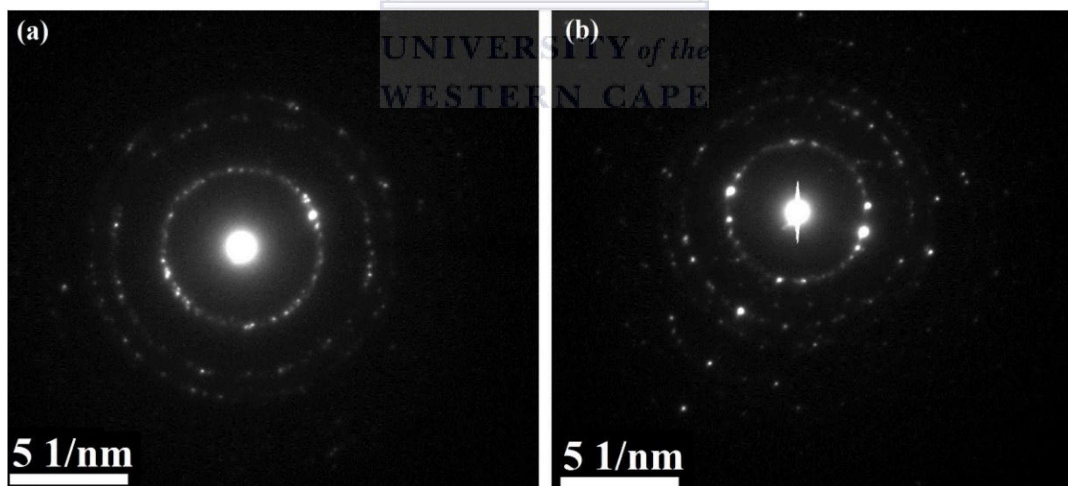

UNIVERSITY of the
WESTERN CAPE

Figure 4.12 *SAD images of sample S_2 taken (a) near the interface and (b) in the bulk of the film.*

Fig. 4.12 presents Selected Area Diffraction (SAD) patterns taken near the interface and in the bulk of sample S_2..Fig. 4.12 (a) taken near the interface shows ring-like features with a number of diffraction spots within the rings. The ring-like shaped patterns arre not solid circles as it would be expected in polycrystalline films with a large number of randomly oriented grains[4.58], which indicates that there exist a certain amount of amorphocity in the film. The bright spots seen on the image indicates the presence of few grown single perfect crystals. The calculated lattice constant *a*, assuming the crystal structure to be cubic, was estimated to be 0.50 nm which differs from that of silicon known to be 0.54 nm. This can be interpreted as a distortion of the Si lattice by the presence of C atoms and/or by the presence of SiC nanocrystals.

In contrast Figure 4.12 (b),SAD pattern of S_2 taken in the bulk of the film, is characterized of diffraction rings with bright spots with an increased intensity compared to the pattern taken near the interface. This indicates the improvement in crystallinity as the film grows thicker. The diffraction spots were also used to estimate the lattice constant of the film and it was calculated to be 0.431 nm, which is much far apart of from that of Si. This result suggests an increased C content in the bulk of films grown in the CH_4 starvation regime; this introduces a more severe distortion of the Si lattice yielding a smaller lattice constant; it fits then to refer to the formed material as nc-$Si_{1-x}C_x$:H film.

UNIVERSITY of the
WESTERN CAPE

4.3.3 Effect of CH_4 flow rate on microstructure as studied by FTIR spectroscopy

FTIR spectroscopy was employed to study the effect of CH_4 flow rate on the microstructure. We used samples S_1, S_2, S_3, S_4 and S_5 whose deposition conditions are given in Table 4.1. Fig 4.13

presents the FTIR spectra of samples deposited with different CH_4 flow rate. The spectra were translated along the Y-axis for a clearer view.

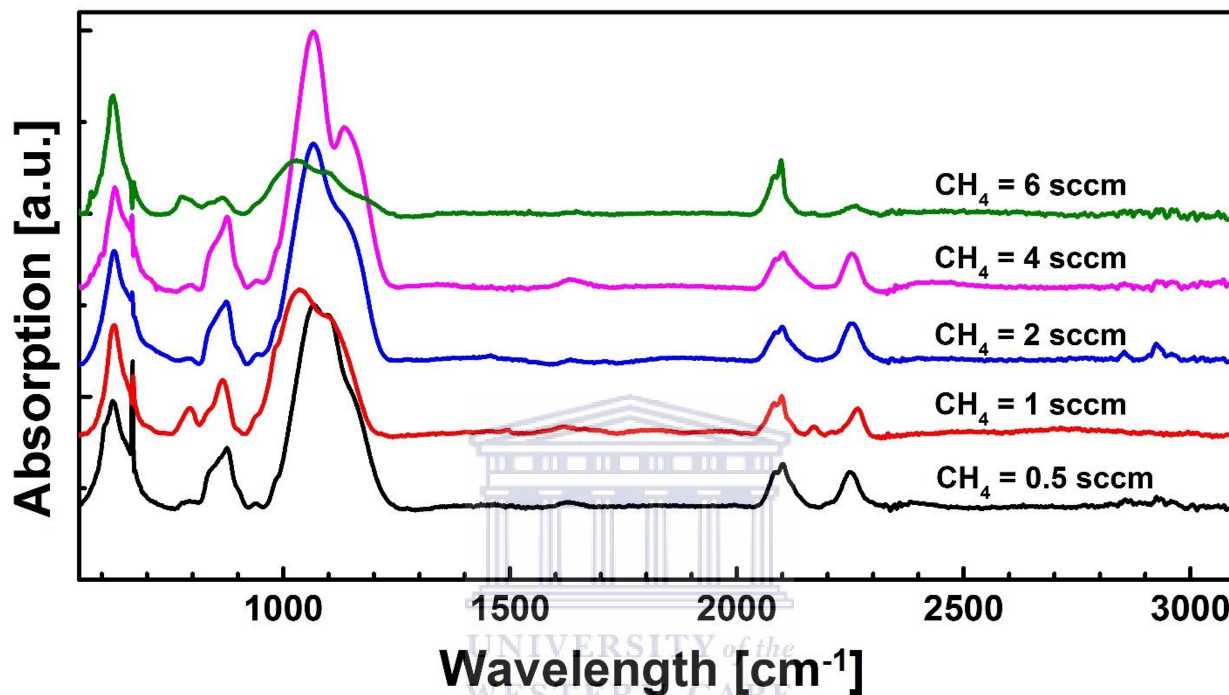

Figure 4.13 *FTIR spectra of samples S_1, S_2, S_3, S_4 and S_5 deposited with varied CH_4 flow rate.*

The figure reveals the existence of the 630 cm^{-1} centred band due to SiH_n in all the spectra. The 830 cm^{-1} – 890 cm^{-1} band due to SiH_2 bending mode was also noted in the spectra; it seems to decrease sharply in intensity for the film that was grown with the highest CH_4 flow rate at 6 sccm. The 960 cm^{-1} – 1050 cm^{-1} band due to CH_n wagging/rocking [4.31] was present in all samples. A shoulder at 1100 cm^{-1} due to oxidation effect in the form of assymetric Si-O-Si stretching modes [4.54] was observed to juxtapose on the peak and it was more apparent as the CH_4 flow was increased up to 4 sccm. This shoulder was interestingly absent in the spectrum of

the film grown with the highest CH_4 flow of 6 sccm however. A band between 770 – 800 cm^{-1} attributed to Si-CH_3 was as well observed, however its center position varied with CH_4 gas flow rate. In the wavenumber 1500 – 4000 cm^{-1} range, the most notable bands are the one between 2000 – 2100 cm^{-1} well known for SiH_n and the one centred around 2250 cm^{-1} attributed to H-SiO_3 indicative of oxidation [4.55]. It is interesting to note that this peak can be correlated to the shoulder observed on the 960 – 1050 cm^{-1} band. It is seen that, in the 6 sccm CH_4 grown film where this shoulder was absent, the 2250 cm^{-1} is suppressed as well. We can thus exclude the scenario where the oxygen will be included as bridging two Si in the form of Si-O-Si instead a polymeric H-SiO_3 is mostly likely due to post- deposition oxidation of inner exposed surfaces of the grain boundaries.

UNIVERSITY of the
WESTERN CAPE

The band found between 960-1050 cm^{-1} attributed to C-H_n wagging/rocking was observed to decrease however randomly with CH_4 gas flow rate. It was also observed that the increase of the C-H_n can be closely linked to increase with bands centered around 1100 cm^{-1} attributed to assymmetric Si-O-Si stretching modes [4.33] and 2250 cm^{-1} attributed to H-SiO_3 vibration, indicative of the presence of oxygen in the films [4.34, 4.35]. The bond densities of Si-H absorption bands were calculated according to Eqn. 3.08 that was expressed as $N_{Si-H} = A_{Si-H} I_{Si-H}$. The proportionality factor A_{Si-H}, or absorption strength is given by $2.1 \times 10^{19}\ cm^{-2}$ for the Si–H bonds at 640 cm^{-1}. Origin® data analysis and graphing software was used to determine the integrated absorption intensities of the Si-H and Si-C absorption bands.

Hydrogen concentration from Si–H_n bonds at 640 cm^{-1} and those obtained through the simulation of ERD spectra as a function of CH_4 gas flow rate will be presented in the following sections.

4.3.4 Effect of CH_4 flow rate on hydrogen incorporation, investigated by ERDA

Elastic Recoil Detection (ERD) can also be used for quantitative analysis of hydrogen concentration in the deposited samples. Unlike in FTIR technique where molecular H_2 cannot be detected, in ERD one can measure the absolute total hydrogen concentration in the samples. Hydrogen concentration is determined by Eqn. 3.05 – Eqn. 3.07 mentioned in Chapter 3.

Fig. 4.14 shows the depth profiles of hydrogen in the deposited films with varied CH_4 flow rate.

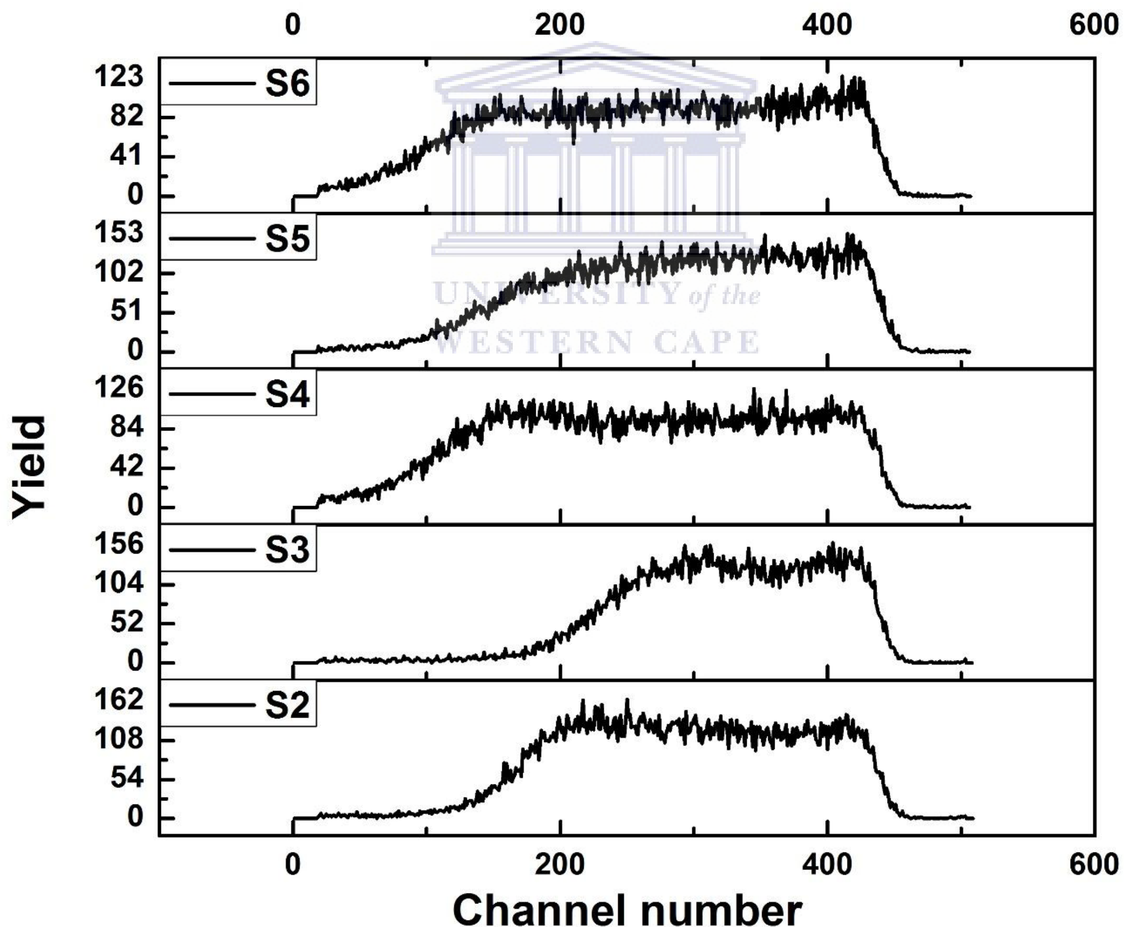

UNIVERSITY of the
WESTERN CAPE

Figure 4.14 *Hydrogen depth profile of the deposited a-SiC:H films at filament temperature of 2000°C.*

The first clear observation from the spectra is that samples S_4, S_5 and S_6 should be thicker than samples S_2 and S_3 since an appreciable yield is stored in smaller channel numbers in $S_4 – S_6$; this points to hydrogen recoils detected with lower energy and thus originating from deeper thickness.

SIMNRA was used to estimate the depth profile of hydrogen content by simulating ERD spectra split in many smaller layers. In data fitting, the quadratic deviation of the simulated from the measured data points is minimized by varying the input parameters of the calculation. SIMNRA uses the Simplex algorithm for fitting. The user has the freedom to fix the fit accuracy before the program converges. A fit accuracy of between 1% to 5% is generally reasonable. The free parameters: energy calibration (i.e. energy/channel and offset), Particles*sr, thickness of a layer and composition of a layer can be fitted independently or all at once. The layers were then combined to determine the total hydrogen in the sample. The thickness was obtained from the target tool once the simulation of the experimental data had converged. The total hydrogen concentration was obtained as a weighted average value of the set layers.

UNIVERSITY of the
WESTERN CAPE

Fig. 4.15 shows the comparison between the total hydrogen content calculated by ERDA and that from hydrogen content bonded to Si as calculated from the 640 cm^{-1} band, as a function of CH_4 flow rate for samples deposited with a filament temperature of 2000°C.

The results show that the profiles obtained from the two techniques are more or less the same; obviously the hydrogen content obtained by ERDA is greater than that obtained in FTIR. The excess in the ERDA hydrogen obtained content accounts for hydrogen bonded to C which is not included in the 640 cm^{-1} band as well as molecular H_2 which is not detected in FTIR. The latter is expected to be negligible in good quality constructed network because it resides in interstitial sites and in voids [4.56].

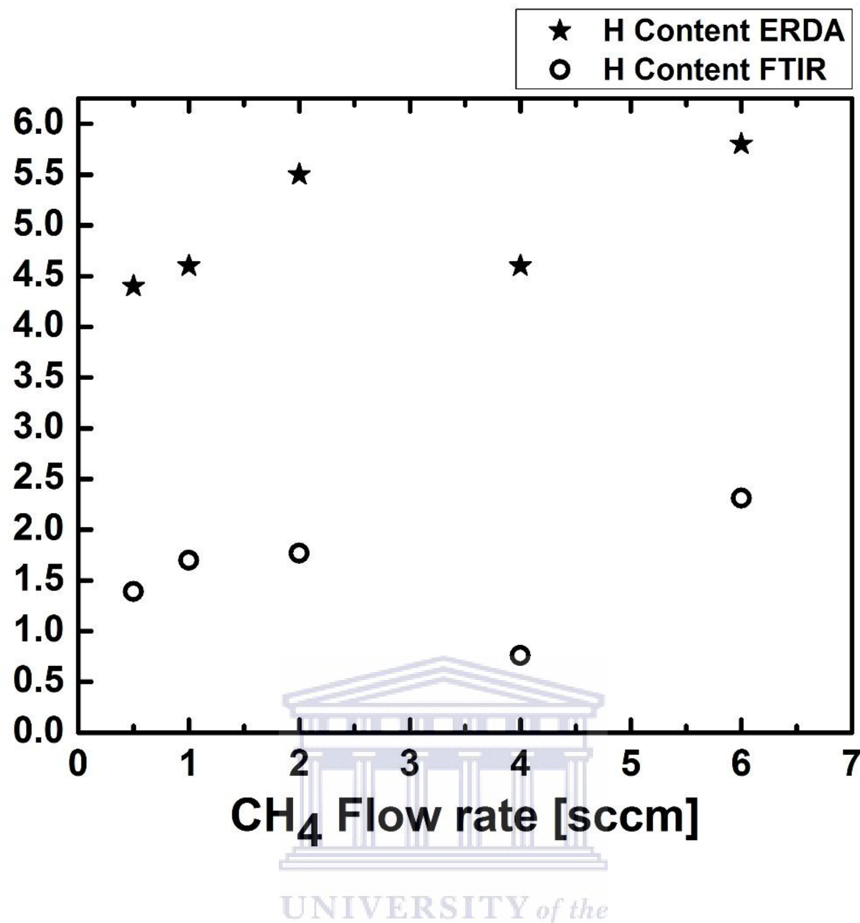

UNIVERSITY of the
WESTERN CAPE

Figure 4.15 *H concentration from ERDA and FTIR techniques obtained from samples deposited with varied CH_4 gas flow rate at filament temperature 2000°C.*

Taking into consideration that the total hydrogen in the film is obtained from Si-H_n bonds, C-H_n bonds and from H_2, the excess hydrogen content found by ERDA can thus be essentially attributed to H-content bonded to C in different forms in the band centered around 960 – 1050 cm^{-1} if H_2 is taken as negligible, a reasonable assumption in compact optimized films. With this assumption, the difference between the hydrogen contents calculated from the two techniques can be used to estimate the infrared absorption strength of CH_n bonds found between the 960 – 1050 cm^{-1} wavenumber's range.

4.3.5 Determination of the absorption strength of the 960 - 1050 cm^{-1} band due to CH_n bonds

FTIR technique is regularly used to determine hydrogen content from Si-H and C-H related bonds found at 640 cm^{-1} and 2800 – 3000 cm^{-1} bands respectively [4.36]. However, in this thesis, no peaks were observed in the band 2800 – 3000 cm^{-1}, with only $C\text{-}H_n$ contributions at 960-1050 cm^{-1} whose absorption strength constant has not been reported before. Therefore an attempt has been made to determine the absorption strength of this band in order to estimate the bonds density contributing to the IR absorption in the range 960 -1050 cm^{-1}.

The suggested absorption strength for the $C\text{-}H_n$ wagging/rocking mode was determined from the difference between the total hydrogen content obtained in ERDA and the total hydrogen content obtained from the 630 cm^{-1} centred band in FTIR spectra. Molecular hydrogen, which is undetectable in FTIR, was neglected because of its low contribution in the deposited films. Integrated absorption intensities of the $C\text{-}H_n$ bonds between 960 – 1050 cm^{-1} were determined from the FTIR spectra using the Maley method mentioned in section 3.4.1. Table 4.3 presents the absorption strength for the $C\text{-}H_n$ bonds determined from the as-deposited films with varied CH_4 flow rates.

UNIVERSITY of the
WESTERN CAPE

The absorption strength were determined only from samples with very well-known thicknesses measured from direct TEM analysis in order to avoid extra uncertainties that might result from non-very well thickness (determined from simulations). The average value of the absorption cross section was then used to estimate hydrogen concentration in C-H bonds from the 960 – 1050 cm^{-1} band.

Table 4.3 *$C\text{-}H_n$ absorption strength at 960 – 1050 cm $^{-1}$ band determined from ERDA and FTIR techniques.*

Sample	H ERDA (at.%)	H FTIR (at.%)	H [ERDA-FTIR] (at.%)	$A_{C\text{-}H}$ (cm^{-2})
S_2	4.40	1.39	3.01	7.30 E+19
S_5	4.60	0.76	3.84	6.29 E+19
S_6	5.56	1.74	3.82	7.29 E+19

An average value of the absorption strength from the above three samples was calculated to be 6.96 E+19 cm^{-2} and was used to determine the densities of C-H bonds for samples S_1 ,S_2, S_3, S_4, S_5 and S_6; the obtained results are tabulated in Table 4.4.

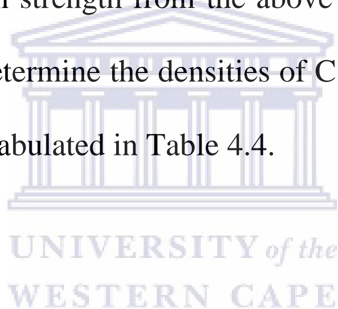
UNIVERSITY of the
WESTERN CAPE

Table 4.4 *Hydrogen concentration obtained from $C\text{-}H_n$ bonds compared with the total hydrogen content and hydrogen bonded to Si atoms.*

Sample name	H_{Total} [at.%]	$H_{Si\text{-}H}$ [at.%]	$H_{C\text{-}H}$ [at.%]
S_1	5.80	2.31	2.60
S_2	4.40	1.39	2.79
S_3	4.60	1.70	2.05
S_4	5.50	1.77	2.79
S_5	4.60	0.76	4.07
S_6	5.56	1.74	3.52

The obtained results of the hydrogen concentration from the C-H bonds at peak between 960 – 1050 cm^{-1} determined using the calculated absorption strength was found to consist of an error ranging between ±5% and ±19% in all samples in the assumptions that the H contents from ERD and from FTIR at 640 cm^{-1} are accurate.

The sources of errors maybe due to many factors including the contribution of molecular hydrogen known to reside in voids that was ignored, the thickness used in the calculations which is not 100% accurate, the contribution although negligible of Si-CH_3 at 770 - 800 cm^3 and of H-SiO_3 at 2250 cm^3 which were both ignored; finally and most importantly due to the fact that the integrated areas of the band between 960 – 1050 cm^{-1} may induce further error as this band overlaps, as it can be seen on fig. 4.13, with the absorption bad of oxygen found between 1600 – 1100 cm^{-1}.

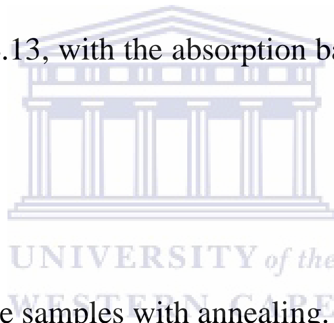
UNIVERSITY of the
WESTERN CAPE

4.5 Evolution of hydrogen in the samples with annealing.

4.5.1 Introduction on the annealing of a-SiC:H films

Annealing of samples has shown in previous studies to alter the microstructure of as deposited films depending of the annealing temperature [4.37, 4.38, 4.39]. Annealing of a-SiC:H films causes a relaxation of the stress in the films, and leads to recrystallization of the film as the hydrogen effuses [4.40, 4.41]. However, it has been shown that the rearrangement of the film structure upon annealing differs following respective periods of anneal [4.41].

Lin *et al.* [4.42] performed annealing experiments of a-SiC:H films at different temperature and studied the structural properties of the deposited films using IR absorption spectroscopy. Lin *et*

al. [4.42] observed that during the annealing process, there was an effusion of H, C-H bonds increased in intensity and there was formation of Si-C bonds, at the same time a decrease in dangling bonds density of Si and C was noted. However, because of the difference between the Si-H and C-H binding energies, hydrogen effusion is expected to occur at different stages during annealing leading to a rearrangement of the film's structure at specific temperature. In this study, we investigate the effect of the temperature and time period of anneal on structural properties of the films.

4.5.2 Annealing conditions

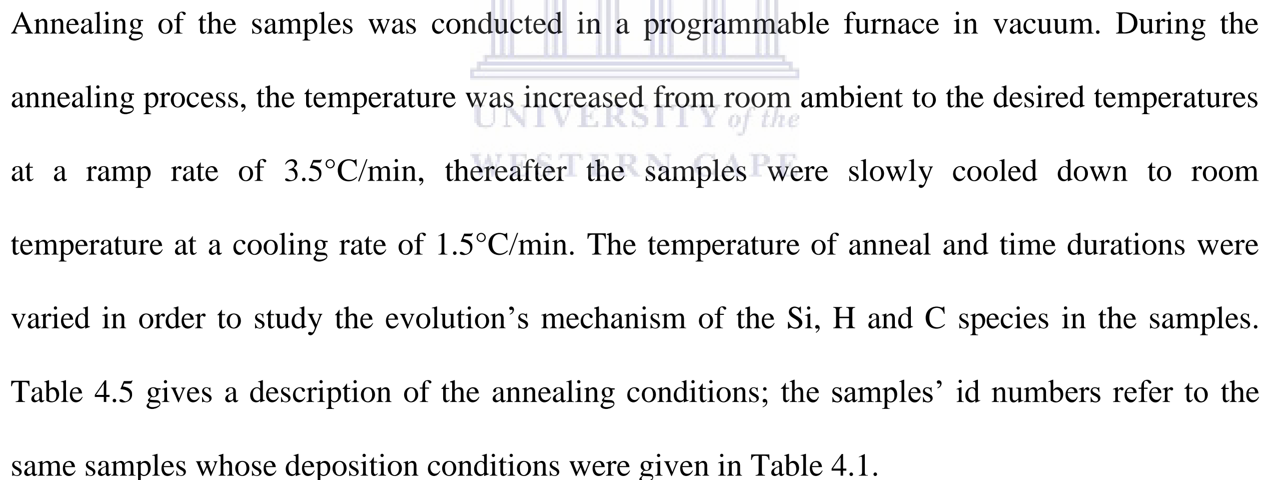

Annealing of the samples was conducted in a programmable furnace in vacuum. During the annealing process, the temperature was increased from room ambient to the desired temperatures at a ramp rate of 3.5°C/min, thereafter the samples were slowly cooled down to room temperature at a cooling rate of 1.5°C/min. The temperature of anneal and time durations were varied in order to study the evolution's mechanism of the Si, H and C species in the samples. Table 4.5 gives a description of the annealing conditions; the samples' id numbers refer to the same samples whose deposition conditions were given in Table 4.1.

Table 4.5 *Summary of annealing conditions.*

Sample name	T_f (°C)	Anneal Time (min)	Anneal Temp. (°C)	Comment
S_1	1700	60	900, 1100	Effect of the temperature of anneal
S_6	2000	30	900, 1100	

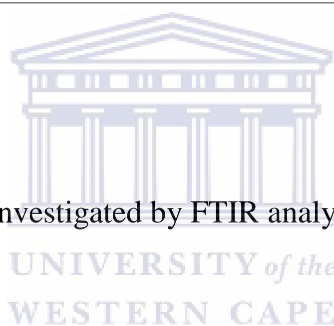
UNIVERSITY of the
WESTERN CAPE

4.5.3 Annealing induced effects investigated by FTIR analytical technique.

The vibrational properties are known to be closely related to the microstructure of the films [4.43]. Fig 4.16 shows overall FTIR spectra of as-deposited and of annealed samples S_1 and S_6 (the time durations of anneal are specified in the insert). The as-deposited films show vibrational signals of Si-H bonds at 640 cm^{-1} and of C-H bonds at 960 – 1050 cm^{-1} as discussed in section 4.2.3.

A notable difference in the Si-C stretching bands can be observed on the spectra of annealed samples and it is discussed in the following subsections.

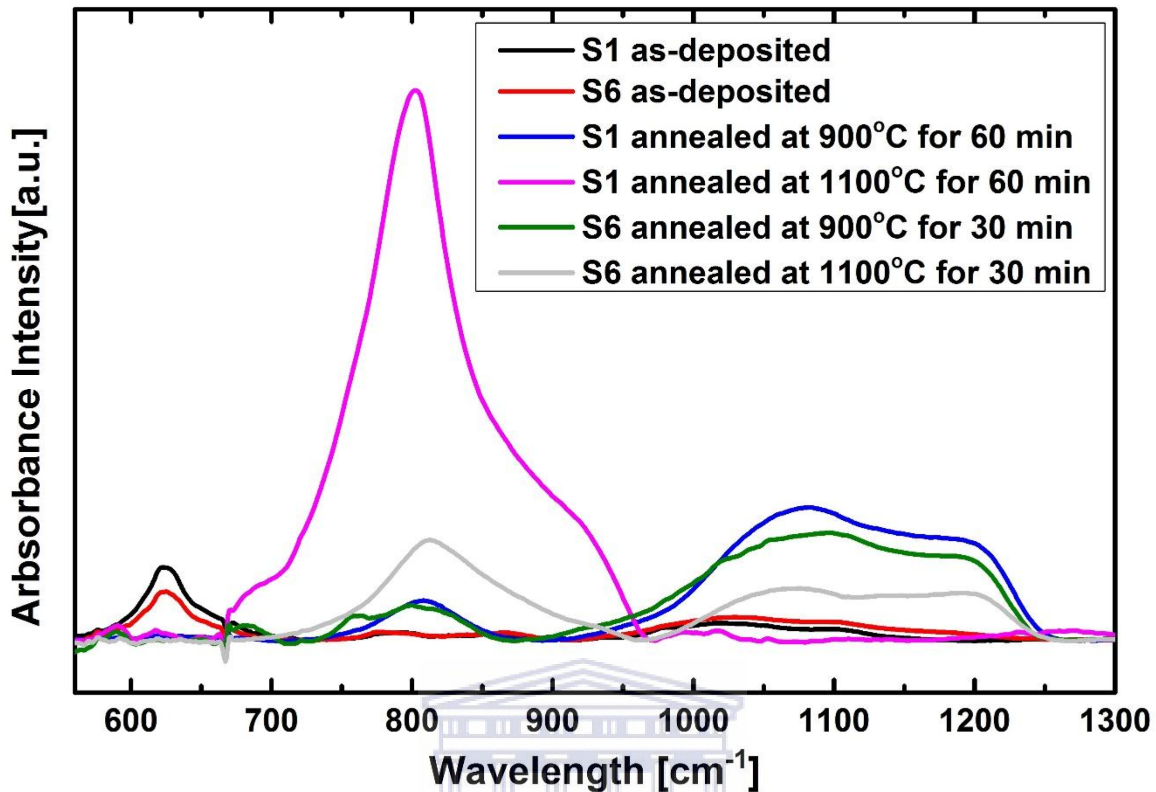

Figure 4.16 *FTIR spectra of as-deposited samples and annealed samples S_1 and S_6.*

UNIVERSITY of the
WESTERN CAPE

4.5.3.1 FTIR features from spectra of films annealed at 900°C

Fig. 4.17 presents the FTIR spectra of as-deposited spectra of samples S_1 and S_6 as well as the respective spectra annealed at 900°C for different time durations; the annealed samples S_1 and S_6 at 900°C showed that there was a sharp decrease in the intensity of the band centered around 640 cm^{-1}. Instead, the intensity of the broad band extending between wavenumbers 960 – 1050 cm^{-1}

attributed to C-H_n bonds, can be seen to increase with anneal (at a temperature of 900°C) in both S_1 and S_6 spectra.

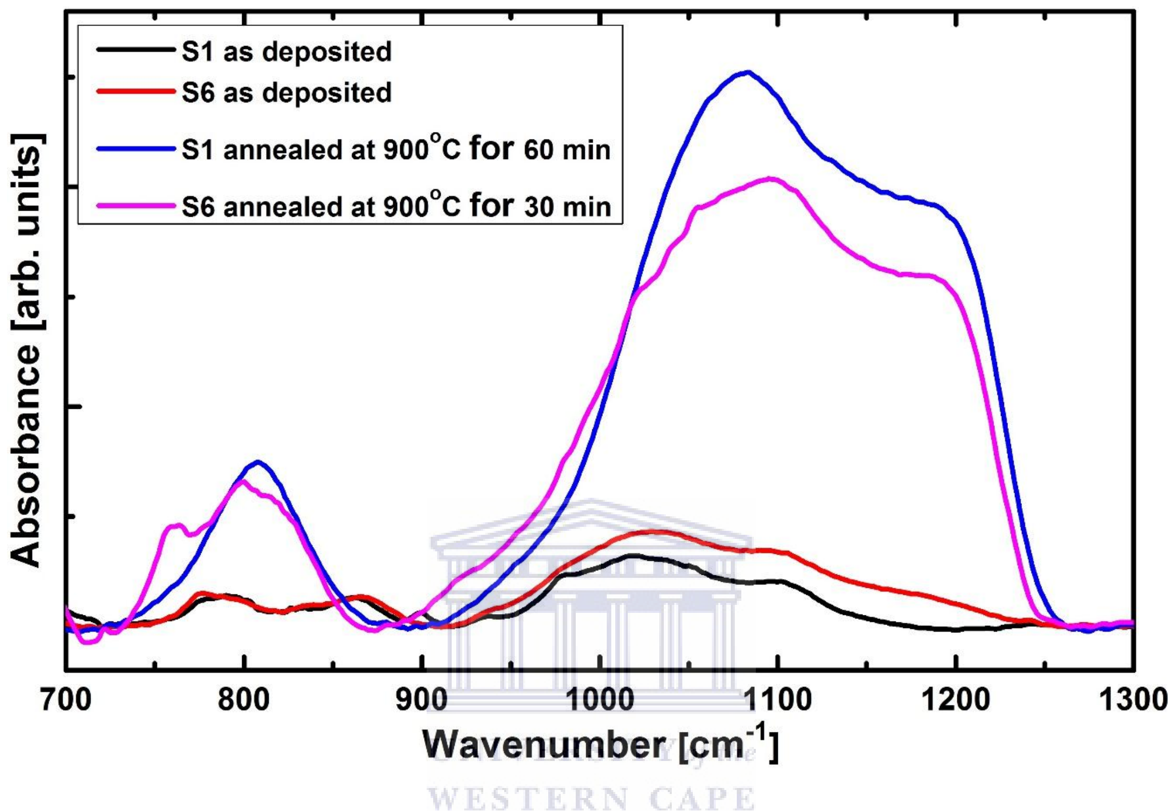

WESTERN CAPE

Figure 4.17 *FTIR spectra of as-deposited spectra of samples S_1 and S_6 as well as the respective spectra annealed at 900°C.*

These results indicate that as the temperature was increased, there was a complete breaking up of Si-H_n bonds and the released H bonded preferentially with the C atoms as supported by the increase in intensity of the 950 – 1100 cm $^{-1}$ band, while a concomitant crystallization in Si-C and in Si-Si for was observed; this is supported by the increase in intensity of the 800 cm^{-1} centred band in fig. 4.17 and by XRD results that will be presented in section 4.5.5 respectively.

The peak attributed to Si-C/Si-CH_3 stretching mode shifts from 780 cm^{-1} to 800 cm^{-1} and increases drastically in bond intensity with the anneal for both S_1 and S_6. A notable observation is that the intensity of the absorption bands is higher for longer annealed sample (S_1) and the 780 - 800 $cm^{-1}$was blue shifted; its shape became a perfect Gaussian and it was centred exactly at 800 cm^{-1}, this indicates that the Si-CH_3 bonds were all completely broken and only a crystalline Si-C mode was responsible for the IR absorption. This cannot be said about the sample annealed for a shorter time (S_6) because the low energy shoulder at ~780 cm^{-1} due to Si-CH_3 was still observable on the spectrum.

Table 4.6 *Si-C bond densities of the annealed samples.*

Sample	Anneal time [min]	Si-C [1x10^{21} cm^{-3}]	~ Si-C [at.%]
S_1 at 900°C	60	1.40	2.73
S_6 at 900°C	30	0.993	1.95
S_1 at 1100°C	60	12.1	19.5
S_6 at 1100°C	30	1.46	2.84

UNIVERSITY of the WESTERN CAPE

The presence of the C-H_n bonds in the films is a clear indication that at the anneal temperature at 900°C for a period of an hour, did not yield the required energy of C-H bonds breakage. On the other hand, the anneal temperature favours a reaction between C and H species since the bond energy of C - H is higher compared to that of Si - H or Si - C [4.40], which explains a sudden increase in C-H bonds at this temperature. Table 4.6 lists the calculated Si-C bond density at both temperatures of anneal, the results obtained from the samples annealed at 900°C are in the first two rows.

4.5.3.2 Annealing at 1100°C

Samples S_1 and S_6 were also annealed at a temperature of 1100°C for 60 minutes and 30 minutes respectively and the resulting FTIR spectra are shown in Fig. 4.18. The spectrum of the annealed sample S_6 at 1100°C for 30 minutes revealed an increase in bond density of the Si-C mode and a decrease in the C-H peak, while that of S_1 after annealing for 60 minutes showed only the Si-C peak without any remaining intensity of the C-H_n band, i.e. the film had crystallized completely in Si-C and in Si-Si.

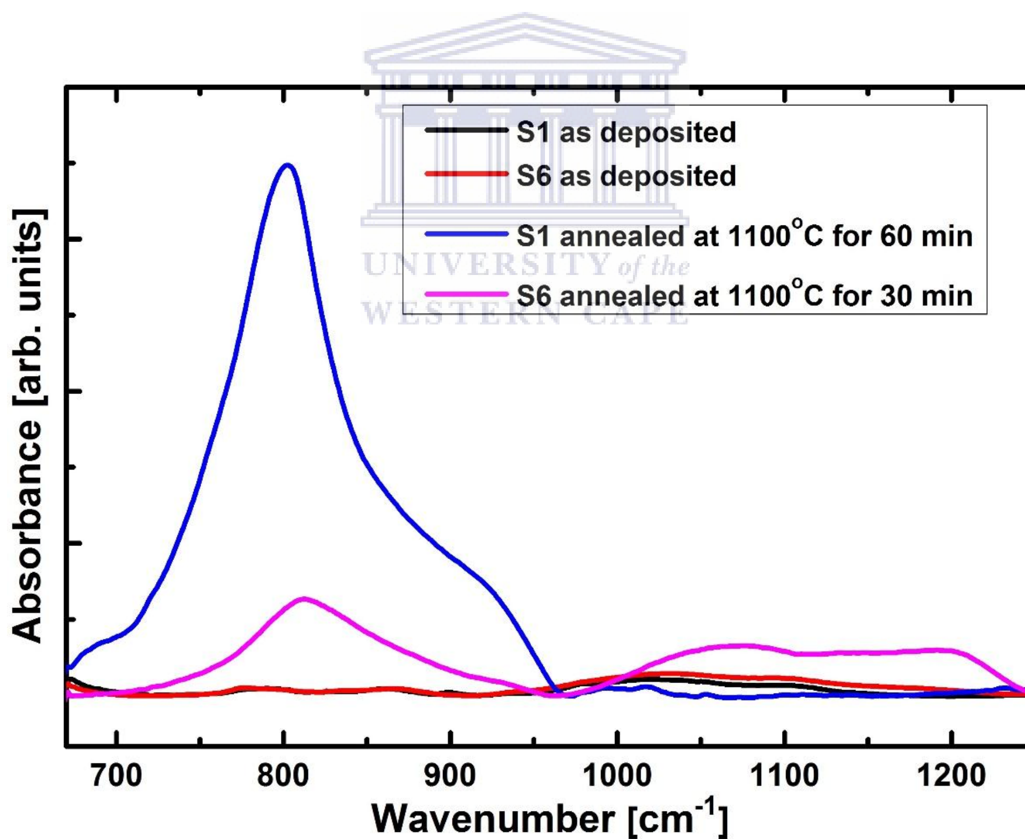

Figure 4.18 *FTIR spectra of as-deposited spectra of samples S_1 and S_6 as well as the respective spectra annealed at 1100°C.*

In S_1, a total dissociation of H from the C bonds was observed as the C-H_n bonds completely disappeared while in S_6 a certain amount of CH_n bonds remained. With no Si-H and C-H bonds observed from the spectra, one can conclude that a complete effusion of hydrogen was achieved at 1100°C.

Annealing of S_1 shows that with enough time applied in the process, fully crystallized material can be achieved following the rearrangement of the network through the effusion of H and the Si-Si and Si-C formation. In S_6, although the spectrum of the annealed film contained more Si-C bonds as supported by the improved intensity of the 800 cm^{-1} peak, if enough duration of time is not allowed for the rearrangement of the network, a residual amorphous structure persists in an otherwise microcrystalline structure as seen on the remaining broad band extending from 960 cm^{-1} to ~1200 cm^{-1} wavenumber.

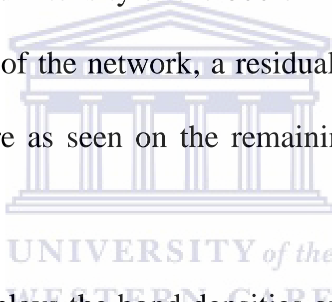
UNIVERSITY of the
WESTERN CAPE

The last two rows in Table 4.6 displays the bond densities of the formed Si-C after annealing at 1100°C. Note the improved SiC bond density in the longer time annealed and fully crystallized S_1.

4.5.4 Effect of annealing on the microstructure as studied by Raman spectroscopy

The annealed samples were characterized by Raman spectroscopy in order to learn about the local re-organization of the a-SiC:H network. From this method, we will study how the films crystallize and the nature of the obtained clusters with the temperature of anneal at different time

durations. Therefore from this method, clusters of a-Si, a-C, nc-Si, a-SiC and nc-SiC should be distinguished if they are present within the films [4.44 - 4.46].

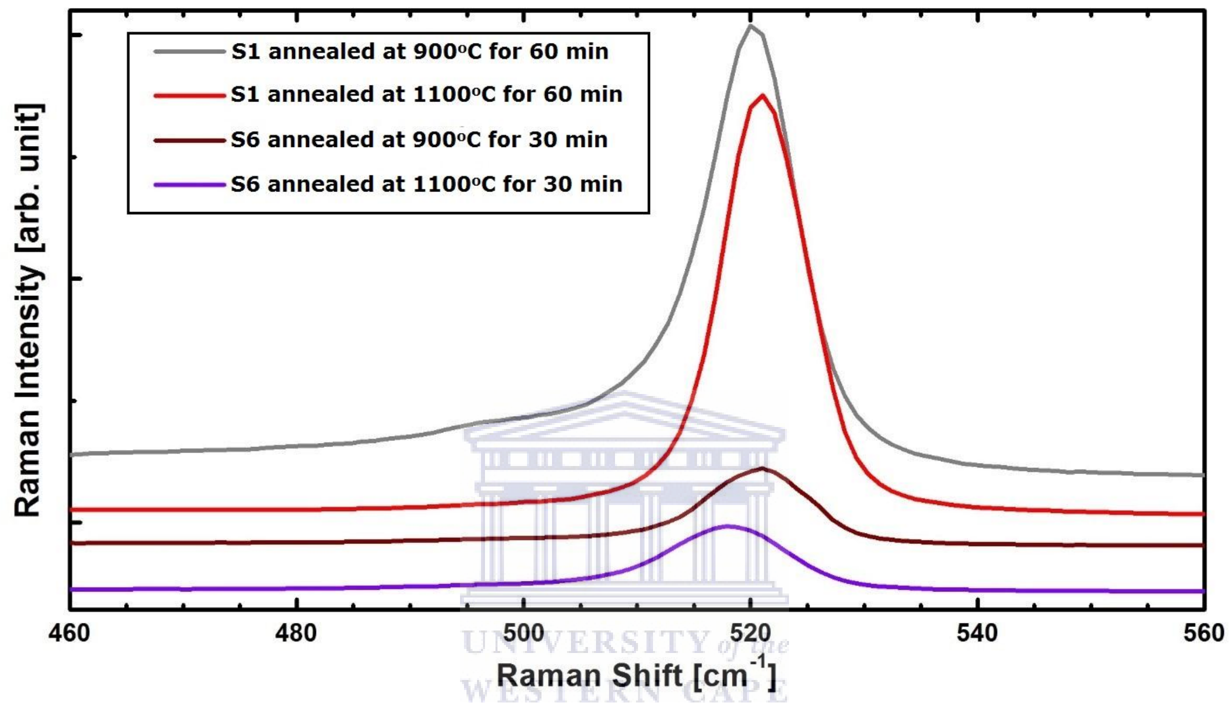

Figure 4.19 *Raman spectra of the films S_1 and S_6 annealed for 60 minutes and 30 minutes, respectively, at temperatures of 900°C and 1100°C.*

Fig. 4.19 presents Raman spectra with focus on the ~520 cm^{-1} peak of samples S_1 and S_6, annealed at temperatures of 900°C and 1100°C for a time period of 60 min and 30 min respectively. A deconvolution of a band between 450 – 550 cm^{-1} usually gives three contributions at 480 cm^{-1}, 505 cm^{-1} and 520 cm^{-1} for a-Si (TO), nanocrystallites/grain boundaries and c-Si (TO) respectively [4.46]. However, the 480 cm^{-1} component was absent in all samples even those annealed at lower temperature of 900°C. Only one peak around 520 cm^{-1} was

observed for all annealed samples with exception to S_1 annealed at 900°C showing also (on top of the 520 cm^{-1}) a remaining component at 500 cm^{-1}due to small crystallites and / or grain boundaries.

The formation of crystallites in the films annealed at 900°C was observed from Raman spectra with a shift towards the 520 cm^{-1} wavenumber where the c-Si peak is found. However, in S_6 the peak center is observed below the 520 cm^{-1} mark compared to S_1 where its peak was found centered just above 520 cm^{-1}. This result suggests that the size of the crystals increased with the longer time of anneal in S_1.

Fig. 4.20 presents Raman spectra of samples S_1 and S_6, with focus on the ~900 cm^{-1} – 1000 cm^{-1} band, annealed at temperatures of 900°C and 1100°C for a varied time period.

UNIVERSITY of the
WESTERN CAPE

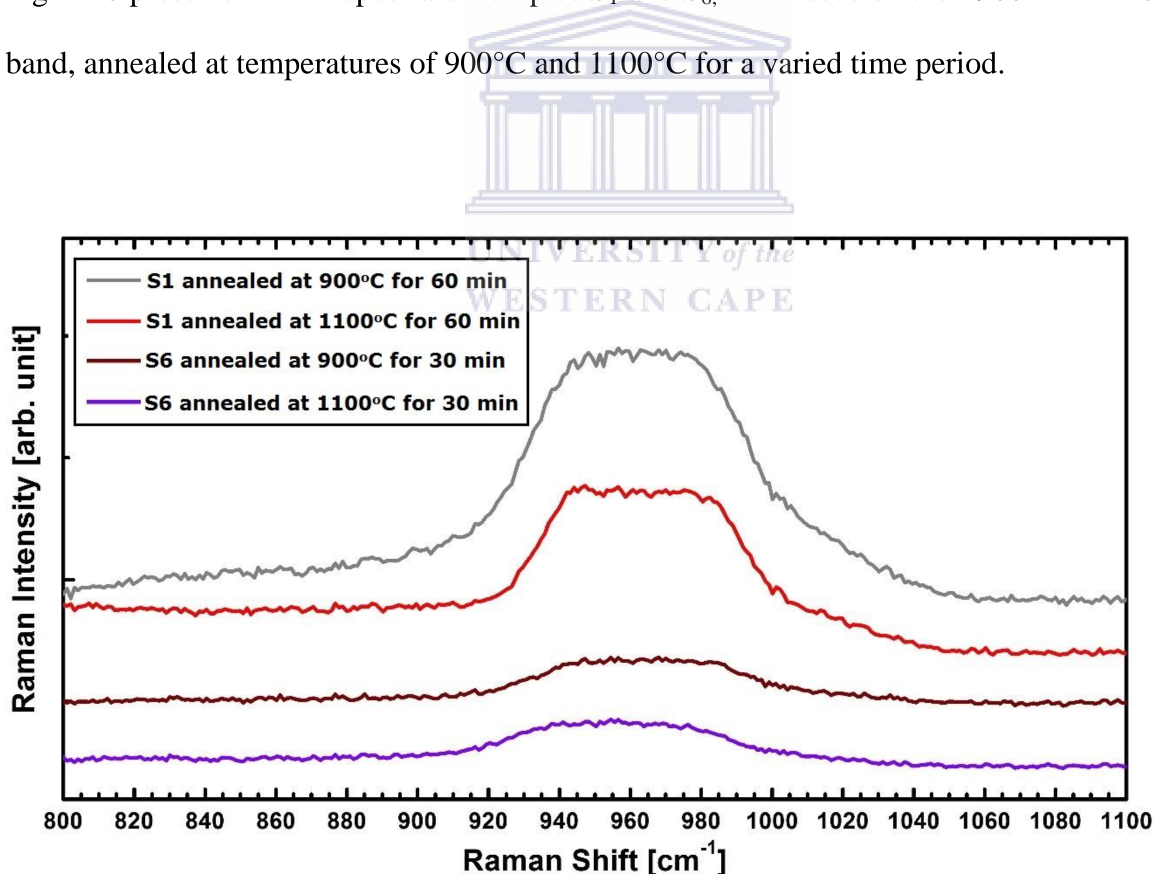

Figure 4.20 *Raman spectra of the films S_1 and S_6 annealed for 60 minutes and 30 minutes, respectively, at temperatures of 900°C and 1100°C.*

From our earlier discussion, the FTIR spectra of the annealed films had indicated the presence of Si-C bonds, therefore it is expected a nc-SiC feature in Raman spectroscopy as well. In Fig 4.20, a broad band centered around 960 cm^{-1} is observed in spectra originating from both annealed samples at 900 and 1100°C for different time duration. The peak at 960 cm^{-1} has been reported to be due to 3C-SiC LO mode [4.60], which is usually accompanied by a peak at 795 cm^{-1} due to TO mode [4.61]. The assignment of this band is however complicated as the first overtone of the 520 cm^{-1} c-Si TO is also observed as a broad band centered at 960 cm^{-1} wavenumber. The difference in the shape of the spectra from annealed samples at different time duration provides good clues about the local order in Raman: the quasi-Gaussian shape in spectra of films annealed for a shorter time is similar to the known shape of the first overtone of c-Si TO peak [4.62]. This is in agreement with the XRD results that showed that those films were Si dominated. The spectra of the annealed samples for longer time are characterized by an asymmetric nature with a noticeable shoulder developing at smaller wavenumbers of the band. A noticeable improvement of the peak intensity is also evident. This suggests that a longer annealing time increases the number of SiC crystallites. A broad band in these wavenumbers is said to be due to a variety of silicon carbide polytypes [4.63, 4.64]. Thus it is implied that after annealing for longer time, a rearrangement of the structure occurs where carbon atoms bonds with Si atoms to form nc-SiC particles within a structurally ordered silicon matrix.

UNIVERSITY of the
WESTERN CAPE

4.5.5 Effect of annealing on the microstructure as studied by XRD

XRD measurements of the annealed samples were performed from films deposited on silicon substrates because samples on Corning glass substrates could not sustain such high temperature of anneal; the shown diffraction patterns of as-deposited films are taken from films deposited on Corning glass. From Fig. 4.21 presents the XRD diffraction patterns of as deposited and annealed samples. The patterns taken from as -deposited samples reproduce the features known to microcrystalline Si materials at 28°, 47° and 56°. In annealed samples, a narrowing of the peaks at 47° and 56° was observed. The narrowing of peaks implies that the crystallites in the films increased in size. However the introduction of additional peaks observed just above 32.5° and just above 42.5° in the patterns of annealed samples signifies inclusion of different other types of crystallites formed in the film during the temperature ramp and annealing processes. The (111) peak even disappeared from the pattern of the sample annealed at 1100°C.

UNIVERSITY of the
WESTERN CAPE

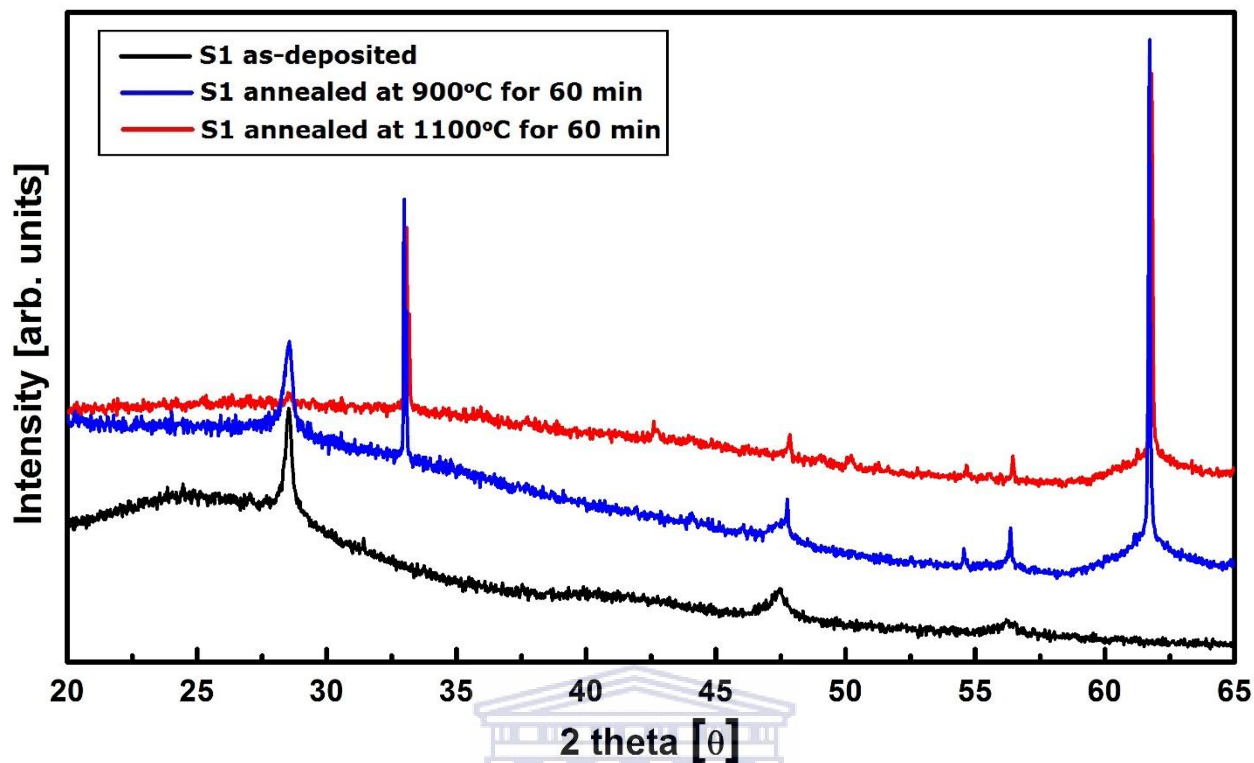

Figure 4.21 *XRD spectra of the film S_1 as-deposited, with its annealed films for 60 minutes at 900°C and 1100°C.*

UNIVERSITY of the
WESTERN CAPE

The additional peaks observed near 32.5° and 42.5° with annealing temperature, can be assigned to inclusion of SiC polytypes identified previously as 6H-SiC by Keffous *et al.* [4.59]. This result agrees with the FTIR results presented earlier where Si-C bonds were appearing with the temperature ramp and annealing. Another additional peak observed at 61.8° does not originate from this polytype however, instead it has been assigned previously to 3C-SiC structure [4.65]. Nethertheless this last assignment should be taken with care as the used c-Si(100) substrate shows a diffraction peak at the same angle. This suggests that the films consist of multiple polytypes formed during the annealing process at 900°C and 1100°C. A change in the structure is observed from the XRD pattern of S_1 annealed at 1100°C as the silicon peaks are greatly

reduced in intensity, with the peak at 32.5° becoming dominant in the structure, the (111) disappearing and other small peaks being seen at 42.5°, 50.0°, 54.5° and 61.8°.

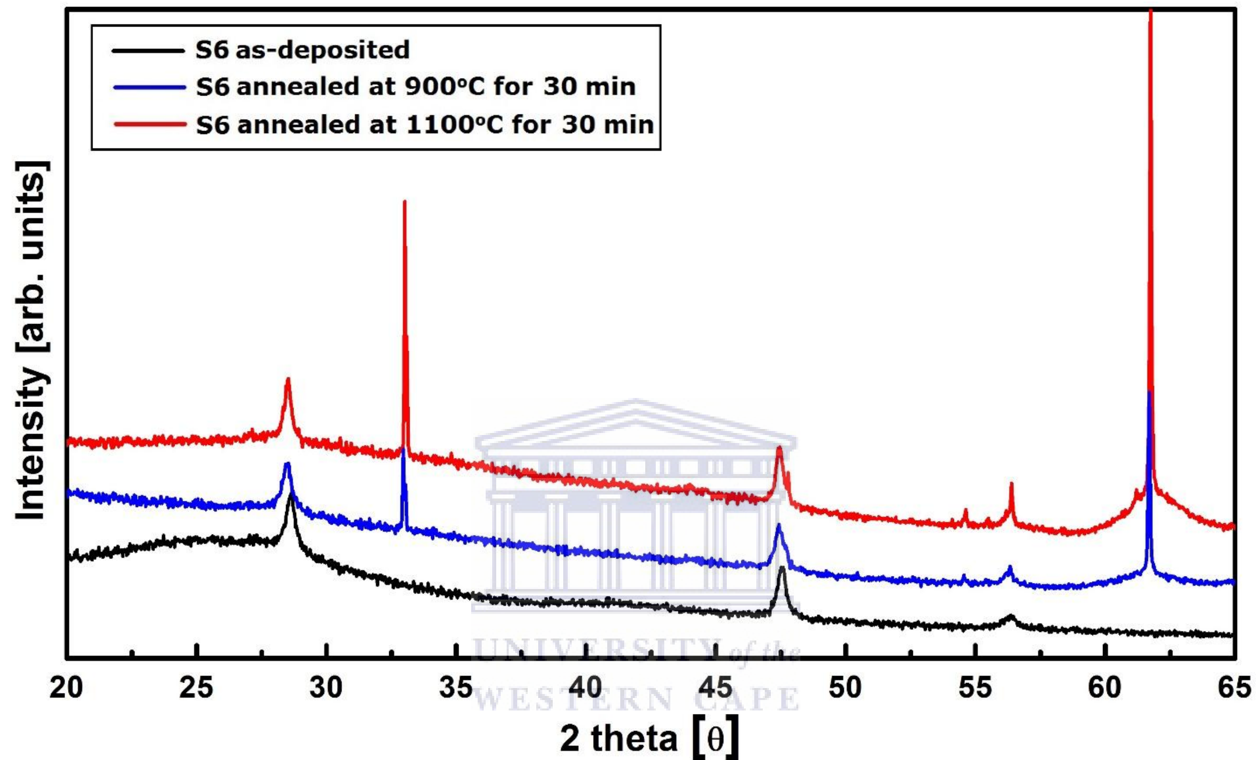

UNIVERSITY of the
WESTERN CAPE

Figure 4.22 *XRD spectra of the film S_6 as-deposited, with its annealed films for 30 minutes at 900°C and 1100°C.*

Fig. 4.22 presents the diffraction patterns of S_6 as deposited and annealed samples: similar diffraction peaks previously observed above in S_1' patterns are recorded.

Table 4.7 lists the crystal sizes of the as-deposited and the annealed samples calculated by the Scherrer formula.

The crystal size in S_1 annealed at 900°C was found to be about 4.5 times larger than that in S_6 while in the as-deposited samples, S_1 related size was 1.4 times smaller than its S_6 counterpart.

The relative bigger crystal size of S_6 compared to S_1 in as deposited films (both deposited with the same H_2 dilution) is to be attributed solely to the higher temperature of the filament that promotes crystallinity. Comparing the same samples annealed at 900°C, S_1 for 60 min and S_6 for 30 min., the crystal size in S_1 was far bigger than that calculated in S_6; the duration time of anneal thus promotes a bigger crystal size.

This behavior was reported in films annealed thermally and by high-energy heavy ion beam irradiation [4.13, 4.37]. This is attributed to the release of H atoms, followed by a recrystallization process.

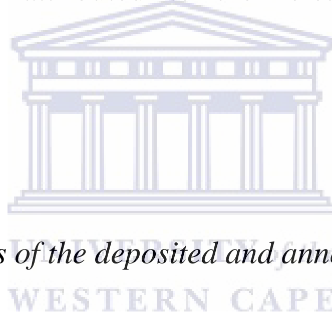
UNIVERSITY of the
WESTERN CAPE

Table 3.7 *XRD crystallite sizes of the deposited and annealed samples by the Scherrer formula.*

Sample name	FWHM [°]	Crystallite size [nm]
S_1 as-deposited	0.5741	15.11
S_6 as-deposited	0.4121	21.06
S_1 annealed at 900°C for 60 min.	0.06310	137.7
S_1 annealed at 1100°C for 60 min.	0.06770	139.2
S_6 annealed at 900°C for 30 min.	0.2943	29.48
S_6 annealed at 1100°C for 30 min.	0.2920	29.72

Another notable observation from Table 4.7 is that the crystal sizes in S_1 annealed at 900°C and 1100°C for a long duration of time are comparable while the size in S_6 also annealed at 900°C

and 1100°C but for a shorter time duration were also comparable; one can conclude then that the annealing time influences strongly the crystal size during the heating process.

4.5.6 Conclusions

It was found from the results obtained at filament temperature of 2000°C that crystallization of a-SiC:H was promoted even when deposited at a relatively low temperature of the substrate of 280°C. Deposition rate of the film is seen to increase with filament temperature as more film forming radicals are more efficiently produced from the CH_4, SiH_4 and H_2 gases. Swain [4.29] had found that the increase in the substrate temperature favoured low hydrogen content in the films; we believe that the decreased hydrogen content in the film deposited at a high temperature of the filament of 2000°C was due to an improved temperature on the surface of the substrate following the radiation of the higher temperature heated filament; the same effect was also found by Arendse [4.30]. Raman scattering, XRD and TEM results showed that the inclusion of C atoms in the films introduced a distortion in the microstructure leading to films consisting of nc-Si:H and a-SiC:H.

UNIVERSITY of the
WESTERN CAPE

ERDA was used in order to determine hydrogen concentration and profile in the deposited films. The ERDA technique has the advantage of determining both the bonded and non-bonded hydrogen concentration in a-SiC:H; this makes it a good complementary technique to FTIR that gives information on the bonded hydrogen only. An attempt has been done to determine the absorption strength constant of the CH_n band detected in the range 960 – 1050 on the infrared spectrum of non-stoichiometric SiC material. .

The FTIR analysis on the samples annealed at 900°C revealed that Si-C stretching modes' features shifted to higher wavenumber around 800 cm^{-1}, which suggested a crystallization in SiC with annealing. This was accompanied by a disappearance of Si-H stretching features in FTIR spectrum due to the H effusion known to occur at ~600°C as it has been previously reported in several papers [4.38, 4.39, 4.49]. At the same time, the C-H wagging/rocking modes at a wavenumber between 960 – 1100 cm^{-1} increased in intensity with new vibrational peaks appearing at ~2850 cm^{-1} and ~2930 cm^{-1} identified as the stretching modes of C-H_n and C-H respectively during reconstruction of the films. Thus FTIR is a good tool to study hydrogen evolution during temperature anneal, a fact established previously by the gas evolution method [4.50]; the activation energy is expected to vary between SiH_n and CH_n due to their different bonding energies.

UNIVERSITY of the
WESTERN CAPE

References

4.1. G. Foti, Applied Surface Science 184 (2001) 20–26.

4.2. M. Mori, A. Tabata, and T. Mizutani, “Properties of hydrogenated amorphous silicon carbide films prepared at various hydrogen gas flow rates by hot-wire chemical vapor deposition,” Thin Solid Films, vol. 501, no. 1-2, pp. 177–180, 2006.

4.3. M. Park, C. W. Teng, V. Sakhrani, M. B. McLaurin, R. M. Kolbas, R. C. Sanwald, R. J. Nemanich, J. J. Hren and J. J. Cuomo, Optical characterization of wide band gap amorphous semiconductors a-SiC:H: Effect of hydrogen dilution. J. Appl. Phys. 89, 1130 (2001).

4.4. S. Nishino, Y. Hazuki, H. Matsunami, T. Tanaka, J. Electrochem. Soc. 127, 2674 (1980)

4.5. S. Nishino, J. A. Powell, H. A. Will, Appl. Phys. Lett. 42, 460 (1983).

4.6. S. Miyajima, K. Haga, A. Yamada, M. Konagai, Low-temperature deposition of highly conductive n-type hydrogenated nanocrystalline cubic SiC films for solar cell applications, Japanese Journal of Applied Physics 45 (2006) L432–L434.

4.7. S. Klein, R. Carius, F. Finger, L. Houben, Low substrate temperature deposition of crystalline SiC using HWCVD, Thin Solid Films 501 (2006) 169–172.

4.8. T.M. Razykov, C.S. Ferekides, D. Morel, E. Stefanakos, H.S. Ullal, H.M. Upadhyaya, Solar Energy 85 (2011) 1580–1608

4.9. M. Tabbal, A. Said, E. Hannoun, T. Christidis, Applied Surface Science 253 (2007) 7050–7059

4.10. J. Kräußlich, A. Fissel, U. Kaiser, K. Goetz, L. Dressler, J. Phys. D: Appl. Phys. 28 (1995) 759-763.

UNIVERSITY of the
WESTERN CAPE

4.11. Y. Tawada, K. Tsuge, M. Kondo, H. Okamoto, Y. Hamakawa, J. Appl. Phys. 53 (1982) 5273.

4.12. S. Zhang, L. Pereira, Z. Hu, L. Ranieiro, E. Fortonato, I. Ferreira, R. Martins, Journal of Non-Crystalline Solids 352 (2006) 1410–1415.

4.13. M. Kuenle, S. Janz, O. Eibl, C. Berthold, V. Presser, K.Nickel, Materials Science and Engineering B 159–160 (2009) 355–360.

4.14. G. Ambrosone, V. Ballarini, U. Coscia, S. Ferrerob, F. Giorgisb, P. Maddalenaa, A. Patellid, P. Ravac, V. Rigatod, Thin Solid Films 427 (2003) 279–283.

4.15. G. Ambrosone, P. Capezzuto, S. Catalanotti, U. Coscia, and S. Mormone, “Optical, electrical and structural properties of hydrogenated amorphous Si-C alloys deposited by different hydrocarbon gas mixtures,” Philosophical Magazine B, Vol. 80, no. 4, (2000) 497–506.

4.16. Y. Huang, A. Dasgupta, A. Gordijn, F. Finger, and R. Carius, Appl. Phys. Lett., 90 (2007) 203502.

4.17. T. Chen, D.R. Yang, R. Carius, F. Finger, Jpn. J. Appl. Phys. 49 (2010) 041303.

4.18. F. Finger, O. Astakhov, T. Bronger, R. Carius, T. Chen, A. Dasgupta, A. Gordijn, L. Houben, Y. Huang, S. Klein, M. Luysberg, H. Wang, L. Xiao, Thin Solid Films 517 (12) (2009) 3507 – 3512.

4.19. P. Musumeci, R. Reitano, L. Calcagno, F. Roccaforte, A. Makhtari, M.G. Grimaldi, Philos. Mag. B Phys. Condens. Matter Stat. Mech. Electron. Opt. Magn. Prop. 76/3 (1997) 323.

4.20. S. Kerdiles, R. Rizk, Philos. Mag. A Phys. Condens. Matter Struct. Defects Mech. Prop. 82/3 (2002) 601.

UNIVERSITY of the
WESTERN CAPE

4.21. G.Y. Xu, T.M. Wang, G.H. Li, Z.X. Ma, G.Z. Zheng, “Raman Spectra Of Nanocrystalline Silicon Films,” Chinese Journal of Semiconductors, Vol. 21, (2000) 1170–176.

4.22. B.P. Swain, R.O. Dusane, “Multiphase structure of hydrogen diluted a-SiC:H deposited by HWCVD,” Materials Chemistry and Physics, vol. 99, no. 2-3, pp. 240–246, 2006.

4.23. M.M. Kamble, V.S. Waman, A.H. Mayabadi, S.S. Ghosh, B.B. Gabhale, S.R. Rondiya, A.V. Rokade, S.S. Khadtare, V.G. Sathe, T. Shripathi, H.M. Pathan, S.W. Gosavi, S.R. Jadkar, “Hydrogenated Silicon Carbide Thin Films Prepared with High Deposition Rate by Hot Wire Chemical Vapor Deposition Method,” Journal of Coatings, Vol. 2014, 2014, Article ID 905903.

4.24. C. Horbach, W. Beyer, and H. Wagner, J. Non-Cryst. Solids 137&138, 661 (1991).

4.25. M.C. Morris, H.F. McMurdie, E.H. Evans, B. Paretzkin, J. H. Degrbot, National Bureau of Standards, Washington, DC. Inst. for Materials Research 02/1975. http://digicoll.manoa.hawaii.edu/techreports/PDF/NBS25-13.pdf.

4.26. T. Chen, Y. Huang, A. Dasgupta, M. Luysberg, L. Houben, D. Yang, R. Carius, F. Finger, Solar Energy Materials & Solar Cells 98 (2012) 370–378.

4.27. S. Halindintwali, D. Knoesen, R. Swanepoel, B.A. Julies, C. Arendse, T. Muller, C.C. Theron, A. Gordijn, P.C.P. Bronsveld, J.K. Rath and R.E.I. Schropp, South African Journal of Science 105, (2009) 7-8.

4.28. Z. Li, J. Bian, H. He, X. Zhang, G. Han, Journal of Physics: Conference Series 276 (2011) 012173.

UNIVERSITY of the
WESTERN CAPE

4.29. B.P. Swain, R.O. Dusane, Materials Letters, Volume 61, Issue 25, October 2007, Pages 4731–4734.

4.30. C.J. Arendse, Hydrogenated amorphous silicon: Optical properties and hydrogen concentration, M.Sc. thesis, University of the Western Cape (1998).

4.31. L. Magafas, C. Mertzanidisa, D. Bandekas, N. Athanasiades, Journal of Optoelectronics and Advanced Materials Vol. 9, No. 7, July 2007, 2030 – 2035.

4.32. W. Yu, W. Lu, L. Han, G. Fu, J. Phys. D: Appl. Phys. 37 (2004) 3304.

4.33. I. Montero, L. Galan, O. Najmi, J.M. Albella, Phys. Rev. B 50, (1994) 4881.

4.34. G. Lucovsky, J. Yang, S.S. Chao, J.E. Tyler, W. Czubatyi, Phys. Rev. B 28, (1983) 3225.

4.35. M. Kamble, V. Waman, S. Ghosh, A. Mayabadi, V. Sathe, T. Shripathi, H. Pathan, S. Jadkar, Bull. Mater. Sci., Vol. 36, No. 7, (2013) 1177–1185.

4.36. T. Kaneko, D. Nemoto, A. Horiguchi, N. Miyakawa, Journal of Crystal Growth 275 (2005) e1097–e1101.

4.37. J. Khamsuwan, S. Intarasiri, K. Kirkby, C. Jeynes, P.K. Chu, T. Kamwanna, L.D. Yu, Surface and Coatings Technology, Volume 206, Issue 5, (2011) 770–774.

4.38. M. Kuenle, S. Janza, O. Eibl, C. Berthold, V. Presser, K. Nickel, Materials Science and Engineering B 159–160 (2009) 355–360.

4.39. N.I. Cho, Y.M. Kim, J.S. Lim, C. Hong, Y. Sul, C.K. Kim, Thin Solid Films 409 (2002) 1–7.

4.40. S. Janz, Amorphous Silicon Carbide for Photovoltaic Applications (Ph.D. Thesis), Fraunhofer Institute for Solar Energy Systems, Freiburg, Germany, (2006).

UNIVERSITY of the
WESTERN CAPE

4.41. L. Calcagno, P. Musumeci, F. Roccaforte, C. Bongiorno, G. Foti, Crystallisation Mechanism Of Amorphous Silicon Carbide, Applied Surface Science 184 (2001) 123–127.

4.42. W.L. Lin, H.K. Tsai, S.C. Lee, W.J. Sah, W.J. Tzeng. Appl. Phys. Lett., 51 (1987) 2112.

4.43. Shu-Ya Lin and S.T. Chang, "Variations of Vibrational Local Modes and Electronic States of Hydrogenated Amorphous Silicon Carbide under Thermal Annealing", J. Phys. Chem. Solids 59, (1998) 1399-1405.

4.44. B.P. Swain, B.S. Swain, Y. Chung, N.M. Hwang, Solid State Sciences 11 (2009) 1408–1411.

4.45. M.M. Kamble, V.S. Waman, A.H. Mayabadi, S.S. Ghosh, B.B. Gabhale, S.R. Rondiya, A.V. Rokade, S.S. Khadtare, V.G. Sathe, T. Shripathi, H.M. Pathan, S.W. Gosavi, S.R. Jadkar, Journal of Coatings, Volume 2014, Article ID 905903, 11.

4.46. F.S. Tehrani, S.A. Rahman, J Mater Sci: Mater Electron (2014) 25:2366–2373

4.47. Y. He, C. Yin, G. Cheng, L. Wang, X. Liu, J. Appl. Phys. 75 (2), 15 January 1994

4.48. R.J. Iwanowski, K. Fronc, W. Paszkowicz, M. Heinonen, J. Alloys Compd. 286 (1999) 143.

4.49. Y. Wang, J. Lin, C.H.A. Huan, Z.C. Feng, S.J. Chua, Thin Solid Films 384 (2001). 173 -176.

4.50. Jang-Ho Park, Jae-Beom Choi, Hae Yeol Kim, Ki-Young Lee, Jai-Young Lee, Thin Solid Films 266 (1995) 129-132.

4.51. T. Chen, D. Yang, R. Carius, F. Finger, Thin Solid Films 519 (2011) 4516–4518.

4.52. S. Nonomura, N. Yoshida, T. Itoh, Thin Solid Films 501 (2006) 164 – 168.

UNIVERSITY of the
WESTERN CAPE

4.53. T. Chen, F. Köhler, A. Heidt, Y. Huang, F. Finger, R. Carius, Thin Solid Films 519 (2011) 4511–4515.

4.54. I. Montero, L. Galan, O. Najmi, J.M. Albella, Phys. Rev. B 50 (1994) 4881.

4.55. G. Lucovsky, J. Yang, S.S. Chao, J.E. Tyler, W. Czubatyj, Phys. Rev. B 28 (1983) 3225.

4.56. Arvind Shah, Thin-film silicon solar cells, London, Taylor & Francis, 2010.

4.57. T. Chen, Y.Huang, A.Dasgupta, M.Luysberg, L.Houben, D.Yang, R.Carius, F.Finger, Solar Energy Materials & Solar Cells 98 (2012) 370–378.

4.58. Goodhew, P. H. (2001). Electron Microscopy and Analysis. London: Taylor & Francis.

4.59. A. Keffous, K. Bourenane, M. Kechouane, N. Gabouze, T. Kerdja Vacuum 81 (2007) 632–635.

4.60. H. Shen, T. Wu, Y. Pan, L. Zhang, B. Cheng, Z. Yue, Thin Solid Films 522 (2012) 36–39.

4.61. S. Klein, L. Houben, R. Carius, F. Finger, W. Fischer, Journal of Non-Crystalline Solids 352 (2006) 1376–1379.

4.62. D.W. Feldman, J.H. Parker, W.J. Choyke, L. Patrick, Phys. Rev. 173 (3) (1968) 787.

4.63. S. Nakashima, H. Harima, Phys. Stat. Sol. (a) 162 (1997) 39.

4.64. J. Khamsuwan, S. Intarasiri, K. Kirkby, C. Jeynes, P.K. Chu, T. Kamwanna, L.D. Yu, Volume 206, Issue 5, (2011) 770–774.

4.65. R.J. Iwanowskia, K. Fronca, W. Paszkowicza, M. Heinonenb, Journal of Alloys and Compounds 286 (1999) 143–147.

UNIVERSITY of the
WESTERN CAPE

Chapter 5. Hydrogen Kinetics Studies

5.1 Hydrogen kinetics in a-Si:H and a-SiC: H thin films investigated by Real-time ERD

Hydrogen is known to effuse in a-Si:H thin films when subjected to a temperature anneal over 160°C [5.1], in situ real-time elastic recoil detection analysis was used for the study of hydrogen effusion from amorphous silicon carbide a-$Si_{1-x}C_x$:H films. In effusion measurements, hydrogen depth profiling over intervals of temperature ramping of thin films can reveal information about hydrogen kinetics. A diffusion limited evolution model, based on the solution of the diffusion equation, was applied to extract the kinetic parameters from the integrated retained H content. It is assumed that no H resides in the used c-Si substrate. As the values of the H kinetic properties in hydrogenated amorphous silicon (a-Si:H) are very well established, the proposed method in this study has been applied first to an a-Si:H film in order to validate it.

UNIVERSITY of the
WESTERN CAPE

5.2 Sample description and methods

The a-$Si_{1-x}C_x$:H film's deposition conditions are listed in Table 4.1; however for completeness the deposition conditions of both samples used in this study are presented in Table 5.1. The a-Si:H film was deposited onto Si(100) substrate by HWCVD using feed gas mixtures of SiH_4/H_2 and a temperature of the substrate equal to 375°C.

The studied a-$Si_{1-x}C_x$:H film is not stoichiometric but it instead incorporates a C content x of ~ 7 at. % as it has been determined by EDX studies mention in section 4.1. Details of the real-time

ERDA system are described in Section 3.2.3. During the real-time ERDA measurements, the a-Si:H sample was rapidly ramped from room temperature to 300°C and then subsequently ramped at slower rate of 3°C.min^{-1} from 300°C to 600°C; whereas for the a-SiC:H film, the constant ramping rate of 3°C.min^{-1} was applied between 250°C and 600°C.

Table 5.1 *A summary of the deposition conditions of the films studied for H kinetics properties..*

Sample	Filament T (°C)	Pressure (µbar)	Feed gas (sccm)	Thickness (nm)
a-Si:H	1600	40	SiH_4/H_2: 12 / 48	900
a-SiC:H	2000	150	$SiH_4/CH_4/H_2$: 2 / 4 / 100	1000

UNIVERSITY of the
WESTERN CAPE

During the constant temperature's ramping rate anneal, ERD spectra were collected every 30 seconds and combined in four (for a-Si:H) and eight (for a-SiC:H) in order to form a slice of ERD spectra with improved statistics. The formed slices were thus representative of a temperature range of 6 °C and 12 °C respectively. The spectra collected were then simulated using SIMNRA [5.2] in order to determine hydrogen depth profiles. The channel –energy calibration experiment was done using spectra taken from a 125 µm thick Kapton ($C_{22}H_{10}N_2O_5$) foil at beam energies of 3, 2.5 and 2 MeV. The calibrated data of the experimental set-up, obtained from the simulation of a Kapton foil spectrum (i.e. a simulation that reproduced the

actual thickness and the hydrogen content in the foil) at a beam energy of 3 MeV, have been kept fixed during the simulation process of the studied samples' spectra.

5.3 Results and discussion

Fig. 5.1 compares the profile of few selected ERDA raw spectra of temperature ramped a-Si:H and a-$Si_{1-x}C_x$:H films; the appended red solid curve on Fig. 5.1(b) is a typical example of the simulations done. The spectrum of the as-deposited a-Si:H sample in (a) shows that H was uniformly distributed throughout the thickness (the reader should note that in ERD spectra, the combined effect of the cross section and of the projectile's energy loss is such that the yield decreases rapidly with depth for the same number N_s of target atoms (i.e. same H content)) in contrast to a-$Si_{1-x}C_x$:H film in (b) where an inhomogeneous H profile was observed towards the interface. The stacked spectra in fig. 1(b) indicate also that the H effusion starts at lower temperature in the a-$Si_{1-x}C_x$:H material.

UNIVERSITY of the
WESTERN CAPE

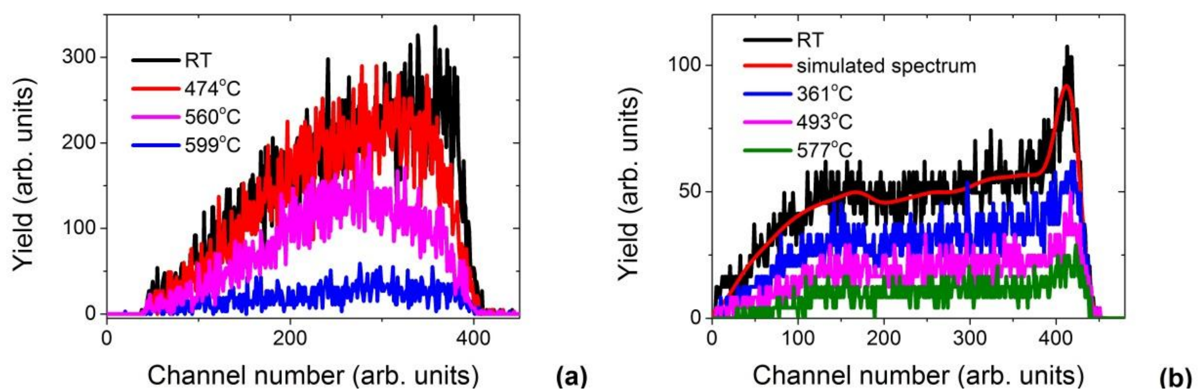

Figure 5.1 *Selected as-taken spectra (a) the a-Si:H (b) the a-$Si_{1-x}C_x$:H ramped from RT to 600 °C.*

Fig. 5.2 presents the total simulated hydrogen content as function of the ramped annealing temperature. In Fig 5.2 (a), H concentration was observed to be constant during the annealing temperature up to about 475°C, and then decreasing rapidly with further increase in temperature. In Fig 5.2 (b), a continuous decrease in H was observed throughout the annealing process. Overall the figure indicates that we have only a high temperature H effusion in a-Si:H film while the a-$Si_{1-x}C_x$:H profile suggests different thermal activated processes through the temperature ramp range.

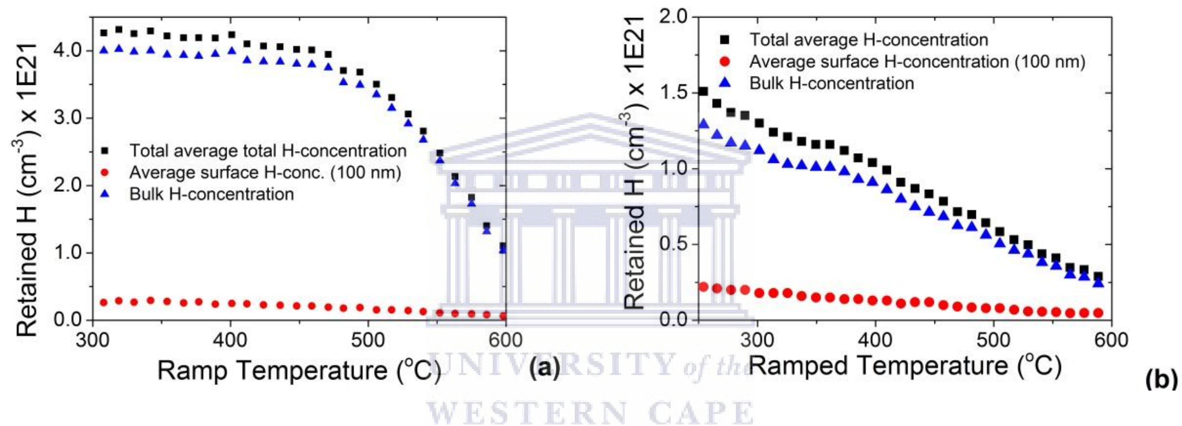

UNIVERSITY of the
WESTERN CAPE

Figure 5.2 *Measured H concentration obtained by simulation, as function of the ramp temperature (a) a-Si:H ; (b) a-$Si_{1-x}C_x$:H.*

In Fig. 5.3 we have plotted the simulated H content as point by point contour maps as a function of depth and ramped temperature. In Fig. 5.3(a) where the results from the a-Si:H were plotted, the bulk hydrogen was fairly stable up to a temperature of ~475°C; the H effusion is seen to be drastic at a high temperature between 500°C – 600 °C which suggests a compact dense material [5.3].

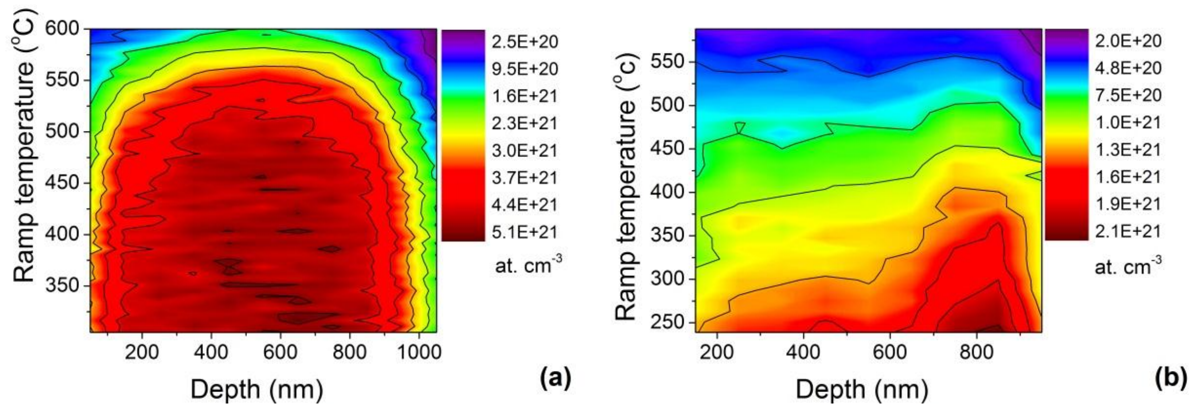

Figure 5.3 *Contour plot maps indicating the depth profile of hydrogen at different ramp temperatures: (a) a-Si:H, (b) a-$Si_{1-x}C_x$:H. The appended contour lines are there as a guide to the eye.*

UNIVERSITY of the
WESTERN CAPE

This is consistent with earlier published results [5.4] that stipulate that hydrogen incorporation in high quality a-Si:H materials is predominantly in the form of isolated Si-H.

Fig. 5.3(b) displays the contour plot of the a-$Si_{1-x}C_x$:H film T ramped at a slow constant rate from around 250 °C to 600 °C A continuous loss of H is observed throughout the range of the temperature studied. Low concentration of C in a-Si films (mainly in a-$Si_{1-x}C_x$:H form) has thus the effect of straining the a-Si network. This is in agreement with the work of Williamson [5.5] that concluded that a-SiC alloy's growth often results in a void-rich structure.

In order to extract the kinetics properties i.e. the activation energy E_a and the pre-factor diffusion coefficient D_0 , we have used the solution of the diffusion equation as discussed earlier in section 3.2.3.1.

Fig. 5.4(a) displays the Arhenius plot obtained from the analysis of the a-Si:H film. Values of (1.62 ± 0.05) eV and 0.51 x 10^{-3} cm^2/s for the activation energy E_a and the diffusion pre-factor respectively were calculated; they are close to those previously reported for compact a-Si:H with a hydrogen content of ~10 at.% [5.3, 5.4, 5.6].

Applied to the a-$Si_{1-x}C_x$:H sample in the high temperature regime (above 481°C) where the H effusion is known to be diffusion limited for a-Si:H films, this model has yielded activation energy E_a and D_0 values (0.31 eV ± 0.01) eV and 1.39×10^{-11} cm^2 / s respectively as seen in fig.4(b) in the upper part of the temperature ramp. The lower half of the temperature ramp (fig. 4(b)) leads to slightly smaller values of activation energy and diffusion pre-factor, which suggests a more complex H effusion process in C-alloyed silicon films. The obtained values of E_a and D_0 for the a-$Si_{1-x}C_x$:H film are particularly low; this points to a void rich microstructure that leads to the instability of hydrogen at the void surfaces and thus its easy desorption.

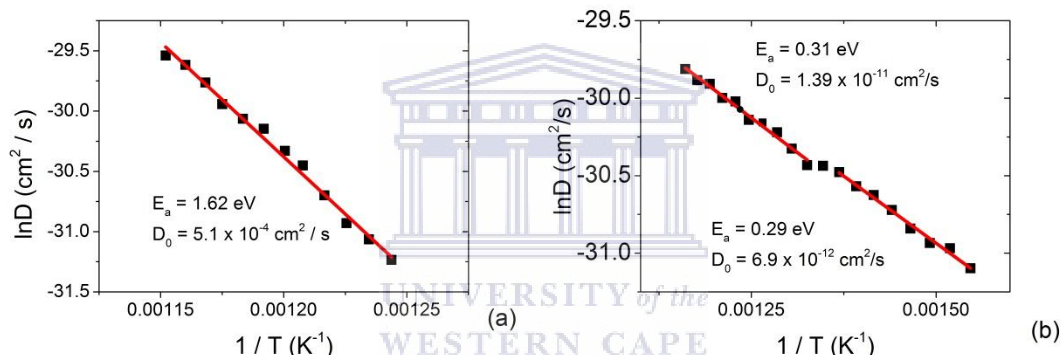

Fig. 5.4 *Arhenius plots of the diffusion coefficient against inverse temperature and the best fits obtained (red solid lines) (a) the a-Si:H sample and (b) the a-$Si_{1-x}C_x$:H film. The obtained values of the kinetic parameters are inserted.*

They are however in very good agreement with the expected values from the previously reported linear dependence curve between the prefactor D_0 and the hydrogen diffusion energy E_D for amorphous, microcrystalline and single-crystal silicon materials [5.4]. Williamson [5.5] attributes the presence of voids in a-SiC:H to the difference in binding energy to H between the alloy C and the host Si atoms. We conclude thus that the random incorporation of C in a-Si:H

has an adverse effect of straining the Si network. The rate of the rupture of Si-H and H desorption from internal surfaces of voids seems to be the main limiting factor in the low C-concentration a-$Si_{1-x}C_x$:H alloys. This is also consistent with the observed continuous loss of H starting at low temperature as observed in fig. 5.2(b) and 5.3(b). Beyer [5.7] had established that H diffusion and H surface desorption in Si were considerably affected by *p*-doping with boron where the low temperature effusion peak shifted towards lower values; it appears that alloying the Si network with smaller atoms like C in small amounts results also in the same effect. It had also been found earlier that the properties of the impurity (e.g. its size) not only influence the rate limiting step of the diffusion process [5.8] but also the effective entropy of diffusion [5.9].

UNIVERSITY of the
WESTERN CAPE

Conclusion

We have studied H effusion from a-Si: H and a-SiC:H films by real-time ERD using a single temperature ramp. In the a-Si:H, the hydrogen exited the sample significantly above 500°C while for a-$Si_{1-x}C_x$:H, the out-diffusion was observed to start below 300°C. A diffusion limited model, using the solution of the diffusion equation, was applied to extract the kinetic parameters with the assumption that no H was diffusing in the substrate but exited only through the surface without any hindrance. The results obtained from the a-Si:H sample are in the range of the reported values for intrinsic a-Si:H with similar hydrogen content indicating that the method of analysis is appropriate. Applying the same analytical method to a HWCVD grown a-SiC:H with a low C content of ~7 at. %, two different thermally activated processes were observed and a lower activation energy value and consequently low H diffusion coefficient were observed; this result points to a defective microstructure resulting from the non-stoichiometric alloying of C in a-Si:H.

References

5.1. J.K. Rath, R.E.I. Schropp, Solar Energy Materials and Solar Cells 53 (1998) 189Ð203.

5.2. M. Mayer, SIMNRA user's guide, Technical report IPP 9/113, Max-Planck Institut für Plamaphysik, Garching, Germany, (1997).

5.3. Arvind Shah, Thin –film silicon solar cells, EPFL Press (2010) 68.

5.4. W. Beyer and H. Wagner, J. Appl. Phys. **53** (1982) 12 8745.J. Crank, *The mathematics of diffusion*, Clarendon press, Oxford, second edition (1975).

5.5. D.L. Williamson, "Structural information on a-Si:H and its alloys from small-angle scattering of X-rays and neutrons", in "*Amorphous Silicon and its Alloys*", ed. Searle, T., Vol. **19** of EMIS Data review series, INSPEC, London (1998).

5.6. D. E. Carlson and C.W. Magee, Appl. Phys. Lett. **33** (1978) 81.

5.7. W. Beyer, Physica B **170** (1991) 105.

5.8. S.K. Sharma, M. P. Macht and V. Naudorf, Phys. Rev. B **49** (1994) 6655.

5.9. W. Frank, A. Hörmer, P. Scharwächter and H. Kronmüller, Mater. Sci. Eng. A **179&180** (1994) 36.

UNIVERSITY of the
WESTERN CAPE

Chapter 6. Conclusions and Recommendations

6.1 Conclusions

In this work, structural properties of a-SiC:H thin films .were studied from material deposited by the HWCVD process. These films were deposited on silicon and glass substrates in order to allow characterization different analytical techniques. The effects caused by filament temperature, methane (CH_4) gas flow rate and ramp / annealing temperature on the films' microstructure were studied.

UNIVERSITY of the
WESTERN CAPE

The low temperature of the filament maintained at 1700 °C was found to produce films with lower deposition rates compared to a filament temperature of 2000 °C. A small RMS roughness of 13 nm was measured for the film deposited with a low temperature of the filament (1700 °C), revealing a smooth surface, while a greater RMS roughness value of 31 nm was calculated for the film deposited at 2000 °C (other process parameters kept unchanged) indicating a rougher surface from the more crystalline microcrystalline material deposited at a high temperature of the filament. Average hydrogen concentration of 2.31 at.% was estimated in films deposited at low temperature of the filament as opposed to ~1.74 at.% in films produced at higher filament temperature; thus higher filament temperature series yielded a better ordering in the film's microstructure.

Keeping the filament to the optimized temperature of 2000 °C, the deposition rate increased with the increase in CH_4 gas flow rate from 1 to 4 sccm where a saturation point was reached; thereafter it decreased for the 6 sccm CH_4 processed sample.

The high hydrogen dilution proved useful in that there was no inclusion of sp^2 C-C bond species which have been shown to be detrimental in solar cells. The deposited films were not stoichiometric however and contained only little C content estimated at ~7at.%. FTIR showed that such class of films contain a pronounced component of C-H_n implying a disordered C inclusion in as –deposited Si based films.

ERDA technique was used to determine the H depth profile and estimate the total hydrogen content in the films. It was found that H distribution was not uniform throughout the films, instead higher H concentrations were observed deeper in the films.

Since the films were rich in C-H_n bonds observed in FTIR at wavenumber between 960 – 1050 cm^{-1} whose absorption strength had not been reported before, an attempt was done to estimate it from both FTIR and ERDA results: an average absorption strength was estimated to 6.69×10^{19} cm^{-2}. This value was used to determine hydrogen concentration from the C-H_n bonds, and the results were found to be in agreement with ERDA measurements with an error extending between 5% and 19% in all studied samples.

UNIVERSITY of the
WESTERN CAPE

Annealing of the films revealed that the heat treatment influenced the effusion of H and promotes the rearrangement of Si, C through the crystallization process as Si-Si and Si-C. TEM, XRD and FTIR supported convincingly this claim.

Real-time elastic recoil detection analysis was performed on a-Si: H and a-SiC:H films by in situ ERD using a single temperature ramp to study the hydrogen kinetics in the films. A high temperature H effusion was observed in a–Si:H suggesting a compact material where hydrogen is bound in isolated Si-H while a continuous effusion of H was noted in a-$Si_{1-x}C_x$:H from temperatures as low as 200°C, suggesting a defective microstructure where H is incorporated in

clusters form. While a single energy H thermally activated process was observed in the a-Si:H film, two thermally activated processes were found in the a-SiC:H films. This complexity of H kinetics in a-SiC material arises due to C alloying.

6.2 Recommendations and Future Research

This is the first full thesis completed on a-SiC:H in our department; we are aware that the deposition conditions of the material have not been optimized yet; future work should focus on achieving full control of the processing parameters so that a stoichiometric SiC material can be produced.

An attempt has been done, for the first time as far as we know, to estimate the absorption strength of the CH_n band at a wavenumber 960 -1050 cm^{-1} in FTIR. Future studies should use samples with varied stoichiometry whose thickness should be known more accurately. We have relied in this work on thickness determined by indirect method as the Dektak profilometer available at our institute was ill-functioning for most part of this thesis investigation.

UNIVERSITY of the
WESTERN CAPE

Maybe the highlight of this study has been the work done on the H kinetics using in situ real-time ERDA and we have proposed a model for data processing; future work would be to apply it on samples containing a varied range of C content from low values as in the present study to near stoichiometric Si-C.